Final Report

Site-Specific Seismic Hazard Analyses and Development of Time Histories for the Port of Alaska

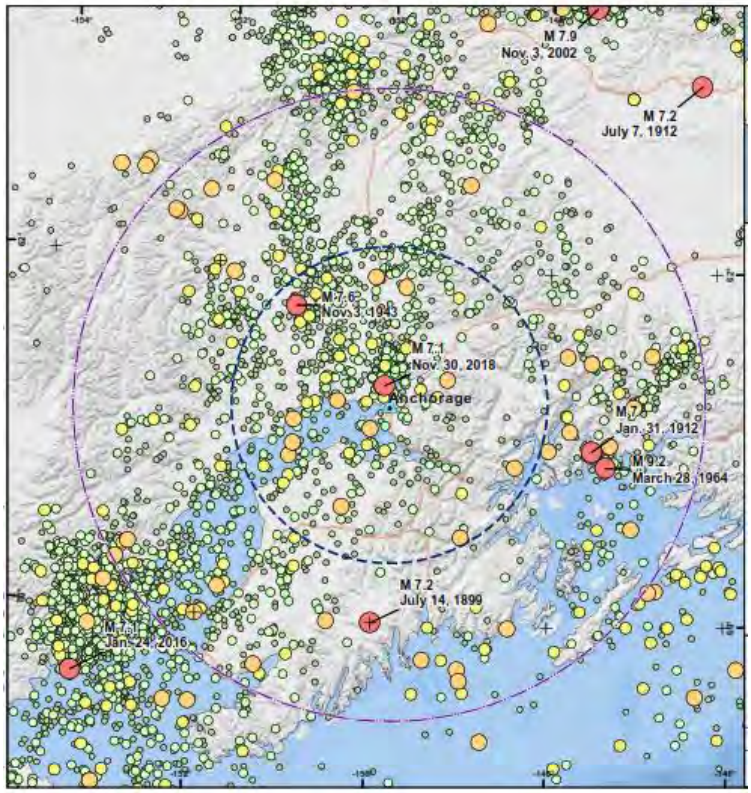

Prepared for:

Jacobs

Prepared by:

Ivan Wong, Nora Lewandowski, Brian Gray, Nesrin Yenihayat, Qimin Wu, and Arash Zandieh
Lettis Consultants International, Inc.
1000 Burnett Avenue, Suite 350
Concord, CA 94520

14 December 2022

Table of Contents

Executive Summary vi

1.0 Introduction 1

1.1 Purpose 1

1.2 Scope of Work 2

1.3 Acknowledgments 3

2.0 PSHA Methodology 4

2.1 Seismic Source Characterization 5

2.1.1 Source Geometry 5

2.1.2 Recurrence 6

2.2 Ground Motion Characterization 7

3.0 Seismotectonic Setting and Historical Seismicity 9

3.1 Seismotectonic Setting 9

3.2 Historical Seismicity 10

3.2.1 Significant Earthquakes 11

3.2.2 Local Seismicity 13

4.0 Inputs to Analyses 14

4.1 Seismic Sources 14

4.1.1 Crustal Fault Sources 14

4.1.2 Crustal Background Earthquakes 19

4.1.3 Alaska Subduction Zone 22

4.1.4 Time-Dependent Model 26

4.2 Ground Motion Models 27

5.0 Seismic Hazard Results 31

5.1 PSHA Results 31

5.2 Comparison with National Seismic Hazard Maps 32

5.3 DSHA Results 33

6.0 Design Earthquake Ground Motions 34

6.1 Conditional Mean Spectra 34

7.0 Development of Time Histories 36

8.0 References Cited 38

List of Tables

Table 1. Seismic Source Parameters for Quaternary Faults Used in the Analysis 48
Table 2. Completeness Estimates and Number of Earthquakes in Each Magnitude Interval for the Modeled Seismic Source Zones 55
Table 3. Recurrence Parameters for the Crustal Source and Intraslab Zones 56
Table 4. Estimated Recurrence Intervals for the Seismic Source Zones 57
Table 5. Seismic Source Parameters for Alaskan Subduction Zone 58
Table 6. Time-Dependent Equivalent Poisson Recurrence Intervals 59
Table 7. Probabilistic Ground Motions at Selected Return Periods.....60
Table 8. Controlling Earthquakes 61
Table 9. Horizontal UHS for Vs30 760 m/sec 62
Table 10. Comparison with the 2007 USGS National Seismic Hazard Map 63
Table 11. Inputs for DSHA 64
Table 12. Median and 84th Percentile Deterministic Horizontal Response Spectra.....65
Table 13. CMS Conditioned at 0.2 and 2.0 Sec for the 975-Year Return Period 66
Table 14. Vertical Spectra for Vs30 760 m/sec.....67

List of Figures

Figure 1. Historical Seismicity in the Site Region, 1882 – 2020
Figure 2. Historical Seismicity Within 100 km of the Site, 1882 – 2020
Figure 3. Quaternary Faulting in Southcentral Alaska
Figure 4. Alaska-Aleutian Subduction Zone and Selected Crustal Faults
Figure 5. Historical Seismicity and the Alaska-Aleutian Wadati-Benioff Zone
Figure 6. Generalized Seismic Hazard Model Logic Tree
Figure 7. Tectonic Setting from Haeussler *et al*., 2017
Figure 8. Isoseismal Map of the 28 March 1964 **M** 9.2 Great Alaska Earthquake
Figure 9. 2018 **M** 7.1 Anchorage Earthquake ShakeMap
Figure 10. Crustal Fault Sources Included in the PSHA
Figure 11. Layered Model for the Castle Mountain Fault
Figure 12. Seismic Source Zones and Declustered Crustal Catalog, 1882 - 2020
Figure 13. Cumulative Magnitude-Recurrence Curves for the Southern Alaska Block and Cook Inlet Source Zone for Mmax 7.0

Figure 14. Cumulative Magnitude-Recurrence Curves for the Yakutat Block Source Zone for Mmax 7.0
Figure 15. Gridded Seismicity for the Southern Alaska Block and Cook Inlet Source Zone
Figure 16. Gridded Seismicity for the Yakutat Block Source Zone
Figure 17. Segmentation of the Alaska-Aleutian Subduction Zone
Figure 18. Cross Section of the Historical Seismicity in the Alaska-Aleutian Wadati-Benioff Zone
Figure 19. Contour Map of Top of Megathrust and Wadati-Benioff Zone
Figure 20. Cumulative Magnitude-Recurrence Curves for the Intraslab Source Zone for Mmax 7.5
Figure 21. Gridded Seismicity for the Intraslab Zone
Figure 22. Seismic Hazard Curves for Peak Horizontal Acceleration for V_S30 760 m/sec
Figure 23. Seismic Hazard Curves for 1.0 Sec Horizontal Spectral Acceleration for V_S30 760 m/sec
Figure 24. Seismic Source Contributions to Mean Peak Horizontal Acceleration Hazard for V_S30 760 m/sec
Figure 25. Seismic Source Fractional Contributions to Mean Peak Horizontal Acceleration Hazard for V_S30 760 m/sec
Figure 26. Seismic Source Contributions to Mean 1.0 Sec Horizontal Acceleration Hazard for V_S30 760 m/sec
Figure 27. Seismic Source Fractional Contributions to Mean 1.0 Sec Horizontal Acceleration Hazard for V_S30 760 m/sec
Figure 28. Magnitude, Distance, and Epsilon Contributions to the Mean Peak Horizontal Acceleration Hazard at (a) 72-, (b) 475-, (c) 975-, and (d) 2,475-Year Return Period for V_S30 760 m/sec
Figure 29. Magnitude, Distance, and Epsilon Contributions to the Mean 1.0 Sec Horizontal Acceleration Hazard at the (a) 72-, (b) 475-, (c) 975-, and (d) 2,475-Year Return Period for V_S30 760 m/sec
Figure 30. Sensitivity of Mean Peak Horizontal Acceleration Hazard to Crustal GMMs for V_S30 760 m/sec
Figure 31. Sensitivity of Mean 1.0 Sec Horizontal Spectral Acceleration to Crustal GMMs for V_S30 760 m/sec

Figure 32. Sensitivity of Mean Peak Horizontal Acceleration Hazard to Megathrust GMMs for V_S30 760 m/sec
Figure 33. Sensitivity of Mean 1.0 Sec Horizontal Spectral Acceleration to Megathrust GMMs for V_S30 760 m/sec
Figure 34. Sensitivity of Mean Peak Horizontal Acceleration Hazard to Intraslab GMMs for V_S30 760 m/sec
Figure 35. Sensitivity of Mean 1.0 Sec Horizontal Spectral Acceleration to Intraslab GMMs for V_S30 760 m/sec
Figure 36. 5%-Damped Uniform Hazard Spectra at the 72-, 475-, 975-, and 2,475-Year Return Periods
Figure 37. 84th Percentile Deterministic Horizontal Acceleration Response Spectra for the **M** 7.6 Intraslab Scenario
Figure 38. 84th Percentile Deterministic Horizontal Acceleration Response Spectra for the **M** 9.2 Megathrust Scenario
Figure 39. Comparison of 84th Percentile Deterministic Horizontal Acceleration Response Spectra
Figure 40. Comparison of 5%-Damped Uniform Hazard Spectra at the 72-, 475-, 975-, and 2,475-Year Return Periods with the Controlling Deterministic Spectra
Figure 41. Uniform Hazard Spectra at 975-Year Return Period and CMS Conditioned at 0.2 and 2.0 sec Using Scenarios for the Interface and Intraslab
Figure 42. 5%-Damped Vertical Spectra at the 72-, 475-, 975-, and 2,475-Year Return Periods

APPENDICES

A 72-Year Return Period Time Histories

B 475-Year Return Period Time Histories

C 975-Year Return Period Time Histories

D 2,475-Year Return Period Time Histories

EXECUTIVE SUMMARY

At the request of Jacobs Engineering Group, this report presents the results of a site-specific probabilistic seismic hazard analysis (PSHA) and deterministic seismic hazard analysis (DSHA) of the Port of Alaska (Port) near Anchorage, Alaska. The purpose of the hazard analyses is to develop Maximum Considered Earthquake (MCE), Design Earthquake (DE), Contingency Level Earthquake (CLE), and Operating Level Earthquake (OLE) ground motions to be used in the Terminal 1 and Terminal 2 concept and preliminary designs. The associated return periods are 2,475, 975, 475, and 72 years, respectively. This study is in response to requirements of design standards applicable to the design of the new terminal structures. This study updates previous analyses of the Port performed in 2008 and 2014.

The objectives of this study are to estimate the levels of ground motions that could be exceeded at specified annual frequencies (or return periods) at the Port, to compare the PSHA results with the results of a DSHA, and to provide acceleration time histories. In this study, geologic and seismologic data were used to evaluate and characterize potential seismic sources, the likelihood of earthquakes of various magnitudes occurring on those sources, and the likelihood of the earthquakes producing ground motions over a specified level. Traditionally, the PSHA is performed assessing time-independent behavior for seismic sources. In this analysis, as was done in the 2014 study, time-dependent behavior for the portion of the Alaska-Aleutian subduction zone beneath Anchorage was included. Basin amplification not considered in previous studies was also included in these analyses.

Inputs included in the PSHA were a seismic source characterization model, ground motion models (GMMs), and site conditions as parameterized by Vs30 (time-averaged shear wave velocity in the top 30 m). The seismic source model consists of Quaternary faults, crustal background seismicity, and the Alaska subduction zone, both the megathrust, source of the 1964 moment magnitude (M) 9.2 earthquake, and the Wadati-Benioff (intraslab) zone. The NGA-West2 GMMs were used for the crustal seismic sources and the global versions of the NGA-Sub GMMs for the two subduction zone sources. The Vs30 assumed in the analyses was for a firm rock site condition (NEHRP B/C) with a Vs30 of 760 m/sec.

The products of the PSHA included mean, median, and fractile hazard curves, seismic source deaggregation, sensitivity analyses, Uniform Hazard Spectra (UHS) for the four return periods, and Conditional Mean Spectra (CMS) for a return period of 975 years. The peak horizontal ground accelerations for the return periods of 72, 475, 975, and 2,475 years were 0.20, 0.56, 0.79, and 1.19 g, respectively. The hazard is higher than calculated in 2014 due primarily to the relatively new NGA-Sub GMMs. The intraslab zone controls the probabilistic hazard at the Port similar to what was observed in the 2014 study. The megathrust does not contribute to the hazard because it was modeled with time-dependent behavior, and only 58 years have elapsed since the 1964 earthquake. We computed a mean recurrence interval of 594 +/- 162 years for a repeat of the 1964 event based on paleoseismic record. Based on the UHS, 11 sets of horizontal and vertical time histories were developed for the four return periods.

The characterization of seismic sources and ground motions in Alaska has been rapidly evolving, particularly since the last USGS Alaska National Seismic Hazard Maps were released in 2007. New paleoseismic data and information and the development of the NGA-Sub GMMs have resulted in changes in our understanding of seismic hazards in Alaska, and it is expected that the future changes are eminent. In particular, the vetting and implementation of the NGA-Sub GMMs has not been thoroughly performed and so changes are expected. We recommend that the hazard and the seismic design ground motions calculated in this study be reviewed and possibly updated as significant advances in seismic hazards in Alaska are achieved. In particular, at this time the USGS hazard results are not available for us to compare with our site-specific hazard results and this comparison should be made to evaluate potential differences. Differences are to be expected since we implemented a time-dependent model for the Alaska subduction hazard which will decrease our hazard results compared to the USGS which uses only a time-independent model for all seismic sources. We also included basin effects which will increase the site-specific hazard at long periods compared to the USGS results. Despite these different approaches, the comparisons will be valuable to better understand other differences in both models and approaches.

1.0 INTRODUCTION

At the request of Jacobs Engineering Group (Jacobs), this report presents the results of a site-specific probabilistic seismic hazard analysis (PSHA) and deterministic seismic hazard analysis (DSHA) of the Port of Alaska (Port) near Anchorage, Alaska. The purpose of the hazard analyses is to develop Maximum Considered Earthquake (MCE), Design Earthquake (DE), Contingency Level Earthquake (CLE), and Operating Level Earthquake (OLE) ground motions to be used in the Terminal 1 and Terminal 2 concept and preliminary designs. The associated return periods are 2,475, 975, 475, and 72 years, respectively. This study is in response to requirements of design standards applicable to the design of the new terminal structures. This study updates previous analyses of the Port performed in 2008 and 2014 by Wong *et al*. (2008; 2014a; 2014b).

Traditionally, the PSHA is performed assessing time-independent behavior for seismic sources. In this analysis, as was done in the 2014 study (Wong *et al.*, 2014a; 2014b), time-dependent behavior for the portion of the Alaska-Aleutian subduction zone beneath Anchorage was included. Basin amplification not considered in previous studies was also included in these analyses.

The Port of Alaska is located in seismically active south-central Alaska with Quaternary-active faults with the potential for generating earthquakes of at least moment magnitude (**M**) 6.5 and larger surrounding the site (Figures 1 to 3). The Alaska subduction zone dominates the seismic tectonic setting and the associated Wadati-Benioff zone lies just south of the site (Figure 4). Large-magnitude deep Wadati-Benioff earthquakes contribute to the hazard at the site (Figure 5).

1.1 PURPOSE

The objectives of this study are to estimate the levels of ground motions that could be exceeded at specified annual frequencies (or return periods) at the Port, to compare the PSHA results with the results of a DSHA, and to provide acceleration time histories. In this study, geologic and seismologic data were used to evaluate and characterize potential seismic sources, the likelihood of earthquakes of various magnitudes occurring on those sources, and the likelihood of the earthquakes producing ground motions over a specified level. This evaluation was limited in scope with respect to input data; we relied solely on available data and information and no field investigations were performed for this analysis.

The PSHA methodology used in this study for assessing ground motion hazard allows for the explicit inclusion of the range of possible interpretations of components in the seismic hazard model, including seismic source characterization and ground motion estimation. Uncertainties in models and parameters are incorporated into the PSHA through logic trees (Figure 6).

The following report presents the seismic source characterization, the ground motion models (GMMs) used in the PSHA and DSHA, ground motion hazard results, and time histories.

1.2 Scope of Work

Jacobs requested the following products. Spectra were calculated by performing a site-specific PSHA. Based on the selected design spectra as described below, time histories were developed.

ASCE 61-23 (Draft) Firm-Rock Acceleration Response Spectra

Provided 22-point acceleration response spectra (5%-damping) for 72, 475, and 975-year (OLE, CLE, and DE) return periods. The spectra were defined for firm-rock conditions (Site Class B/C). (Note draft planned for release for public comment in 2023).

ASCE 7-22 Firm-Rock Acceleration Response Spectra

Provided 22-point acceleration response spectra (5%-damping) for the 2,475-year (MCE) return period. The spectra were defined for firm-rock conditions (Site Class B/C).

475-Year and 975-Year Firm Rock Time Histories

Provided acceleration time histories (or time series) fit to updated 475-year and 975-year firm rock ground acceleration response spectra. Used spectral matching procedures to develop 11 sets of orthogonal horizontal and vertical component time histories where the number of sets is based on the seismic source deaggregation results (i.e., crustal, intraslab, and megathrust) representing the two return periods.

2,475-Year and 72-Year Firm Rock Time Histories

Provided acceleration time histories fit to 2,475-year and 72-year firm rock acceleration response spectra. Used spectral matching procedures to develop at 11 sets of time histories based on the seismic source deaggregation results representing the two return periods.

Condition Mean Spectra

Conditional mean spectra (CMS) were computed at two spectral periods for a return period of 975 years to evaluate their use for developing time histories in place of Uniform Hazard Spectra (UHS).

Report Documentation

Provided a report that documents the seismic hazard model update and the development of the acceleration time histories.

Meetings

Attended three (3) 1-hour virtual meetings through MS Teams. Meetings included a kickoff meeting, a progress meeting, and a closeout meeting to discuss results.

1.3 ACKNOWLEDGMENTS

Our thanks to George Newman, Don Anderson, Sean Shin, and Hong Guan for their project support and assistance. Thanks to Peter Haeussler and Rob Witter of the USGS for providing us data and information that was vital to this study. Our appreciation to Claire Unruh and Javier Chalini for their assistance in the report preparation.

2.0 PSHA METHODOLOGY

The PSHA approach used in this study is based on the model developed principally by Cornell (1968). The occurrence of earthquakes on a fault is assumed to be a Poisson process. The Poisson model is widely used and is a reasonable assumption in regions where data are sufficient to provide only an estimate of average recurrence rate (Cornell, 1968). When there are sufficient data to permit a real-time estimate of the occurrence of earthquakes, the probability of exceeding a given value can be modeled as an equivalent Poisson process in which a variable average recurrence rate is assumed. The occurrence of ground motions at the site in excess of a specified level is also a Poisson process, if (1) the occurrence of earthquakes is a Poisson process, and (2) the probability that any one event will result in ground motions at the site in excess of a specified level is independent of the occurrence of other events.

The probability that a ground motion parameter "*Z*" exceeds a specified value "*z*" in a time period "t" is given by:

$$p(Z > z) = 1\text{-}e^{-\nu(z)\cdot t} \tag{1}$$

where $\nu(z)$ is the annual mean number (or rate) of events in which *Z* exceeds *z*. It should be noted that the assumption of a Poisson process for the number of events is not critical. This is because the mean number of events in time t, $\nu(z)\cdot t$, can be shown to be a close upper bound on the probability $p(Z > z)$ for small probabilities (less than 0.10) that generally are of interest for engineering applications. The annual mean number of events is obtained by summing the contributions from all sources, that is:

$$\nu_k(Z > z) = \sum_n \nu_{kn}(Z > z) \tag{2}$$

where ν_{kn} (*Z*>*z*) is the annual mean number (or rate) of events on source n for which *Z* exceeds *z* at site k. The parameter ν_{kn} (*Z*>*z*) is given by the expression:

$$\nu(Z > z) = \sum_n \alpha_n \left(M^0\right) \int_{M^0}^{M_n^u} f_n(M)\left[\int_0^\infty f_{kn}(r|M) \cdot P_{kn}(Z > z|M,r) \cdot dr\right] \cdot dM \tag{3}$$

where $\alpha_n(M^0)$ is the rate of all earthquakes on source *n* above a minimum magnitude, M^0; $f_n(M)$ is the probability density function of earthquake magnitude between M^0 and a maximum earthquake that source *n* can produce, M_n^u (i.e., recurrence model); $f_{kn}(r|M)$ is the conditional probability density function for distance from site *k* to an earthquake of magnitude *M* occurring on source *n*; and $P_{kn}(Z>z|M,r)$ is the conditional probability that, given an earthquake of magnitude *M* at distance *r* from site *k*, the ground motion (Z) will exceed the specified level *z*. Distance *r* is calculated as the closest distance from the rupture to the site.

Calculations were made using LCI's computer program APEX. The program has been validated using the test cases in the Pacific Earthquake Engineering Research (PEER) Center-sponsored PSHA Computer Program Validation Project (Hale *et al*., 2018).

2.1 SEISMIC SOURCE CHARACTERIZATION

Four types of earthquake sources are characterized in this PSHA: (1) fault sources; (2) areal (background) source zones; (3) intraslab sources; and (4) megathrust sources (Section 4.1). Fault and megathrust sources are modeled as three-dimensional surfaces and details of their behavior are incorporated into the source characterization. Areal source zones are regions where earthquakes are assumed to occur randomly, and intraslab sources are zones where locations of past earthquakes are assumed to be likely locations of future earthquakes. Seismic sources are modeled in the hazard analysis in terms of geometry and earthquake recurrence.

The geometric source parameters for faults and the megathrust include location, segmentation model, dip, and thickness of the seismogenic crust. The recurrence parameters include recurrence model, recurrence rate (slip rate or average recurrence interval for the maximum event), slope of the recurrence curve (*b*-value), and maximum magnitude. Clearly, the geometry and recurrence are not totally independent. For example, if a fault is modeled with several small segments instead of large segments, the maximum magnitude is lower, and a given slip rate requires many more small earthquakes to accommodate a cumulative seismic moment. For areal source zones and intraslab sources, only the areas, thickness, maximum magnitude, and recurrence parameters (based on the historical earthquake record) need to be defined.

As described below, uncertainties in the seismic source parameters, which are sometimes large, were incorporated into the PSHA using a logic tree approach (Figure 6). In this procedure, values of the source parameters are represented by the branches of logic trees with weights that define the distribution of values. A sample logic tree for a fault is shown on Figure 6. In general, three values for each parameter were weighted and used in the analysis. Statistical analyses by Keefer and Bodily (1983) indicate that a three-point distribution of 5th, 50th, and 95th percentiles weighted 0.185, 0.63, and 0.185 (rounded to 0.2, 0.6, and 0.2), respectively, is the best discrete approximation of a continuous distribution. Alternatively, they found that the 10th, 50th, and 90th percentiles weighted 0.3, 0.4, and 0.3, respectively, can be used when limited available data make it difficult to determine the extreme tails (i.e., the 5th and 95th percentiles) of a distribution. Note that the weights associated with the percentiles are not equivalent to probabilities for these values, but rather are weights assigned to define the distribution. We generally applied these guidelines in developing distributions for seismic source parameters with continuous distributions (e.g., Mmax, fault dip, slip rate or recurrence) unless the available data suggested otherwise. Estimating the 5th, 95th, or even 50th percentiles is typically challenging and involves subjective judgment given limited available data.

2.1.1 Source Geometry

In the PSHA, it is assumed that earthquakes of a certain magnitude may occur randomly along the length of a given fault or segment. The distance from an earthquake to the site is dependent on the source geometry, the size and shape of the rupture on the fault plane, and the likelihood of the earthquake occurring at different points along the fault length. The distance to the fault is defined to be consistent with the specific ground motion model used to calculate the ground

motions. The distance, therefore, is dependent on both the dip and depth of the fault plane, and a separate distance function is calculated for each geometry and each ground motion model. The size and shape of the rupture on the fault plane are dependent on the magnitude of the earthquake; larger events rupture longer and wider portions of the fault plane. We modeled the rupture dimensions following the magnitude-rupture area and rupture-width relationships of Wells and Coppersmith (1994).

2.1.2 Recurrence

The recurrence relationships for the seismic sources are modeled using the truncated-exponential Gutenberg-Richter, characteristic earthquake, and the maximum magnitude recurrence models (Section 4.1). These models are weighted (Figure 6) to represent our judgment on their applicability to the sources. For the areal source zones and intraslab, only a truncated exponential recurrence relationship is assumed to be appropriate.

We have used the general approach of Molnar (1979) and Anderson (1979) to arrive at the recurrence for the truncated exponential model. The number of events exceeding a given magnitude, N(m), for the truncated exponential relationship is

$$N(m) = \alpha(m^o)\frac{10^{-b(m-m^o)}-10^{-b(m^u-m^o)}}{1-10^{-b(m^u-m^0)}} \quad (4)$$

where $\alpha\ (m^o)$ is the annual frequency of occurrence of earthquakes greater than the minimum magnitude, m^o; b is the Gutenberg-Richter parameter defining the slope of the recurrence curve; and m^u is the upper-bound magnitude event that can occur on the source. A m^o of **M** 5.0 was used for the hazard calculations because smaller events are not considered likely to produce ground motions with sufficient energy to damage well-designed structures.

We have included the model where faults rupture with a "characteristic" magnitude on specific segments; this model is described by Aki (1983) and Schwartz and Coppersmith (1984). For the characteristic model, we have used the numerical model of Youngs and Coppersmith (1985). In the characteristic model, the number of events exceeding a given magnitude is the sum of the characteristic events and the non-characteristic events. The characteristic events are distributed uniformly over a ± 0.25 magnitude unit around the characteristic magnitude, and the remainder of the moment rate is distributed exponentially using the equation (4) with a maximum magnitude 0.25 unit lower than the characteristic magnitude (Youngs and Coppersmith, 1985).

The maximum magnitude model can be regarded as an extreme version of the characteristic model. We adopted the model proposed by Wesnousky (1986). In the maximum magnitude model, there is no exponential portion of the recurrence curve (i.e., no events can occur between the minimum **M** 5.0 and the distribution about the maximum magnitude). The model is a normal distribution centered on the characteristic magnitude and truncated at the upper end of the range at two standard deviations. The standard deviation used is 0.12 magnitude units.

The recurrence rates for the fault sources and megathrust are defined by either the slip rate or the average return time for the maximum or characteristic event and the recurrence *b*-value. Slip rate can be used to compute the activity rate by balancing the long-term accumulation of seismic moment with the long-term release of seismic moment in earthquakes. The slip rate is used to calculate the moment rate on the fault using the following equation defining the seismic moment:

$$M_o = \mu A D \tag{5}$$

where M_o is the seismic moment, μ is the shear modulus, A is the area of the rupture plane, and D is the slip on the plane. Differentiating with respect to time results in the moment rate as a function of slip rate:

$$\dot{M}_o = \mu A S \tag{6}$$

where $\dot{M}_o$ is the moment rate and S is the slip rate. Equation 6 defines the annual rate of buildup of seismic moment. The long-term rate of seismic moment release is a function of the seismic moment released during an earthquake of a given magnitude and the distribution of magnitudes of earthquakes that occur. M_o has been related to moment magnitude, M, by Hanks and Kanamori (1979):

$$\mathbf{M} = 2/3 \log M_o - 10.7 \tag{7}$$

Using this relationship and the relative frequency of different magnitude events from the recurrence model, the slip rate can be used to estimate the absolute frequency of different magnitude events.

The average return time for the characteristic or maximum magnitude event defines the high magnitude (low likelihood) end of the recurrence curve. When combined with the relative frequency of different magnitude events from the recurrence model, the recurrence curve is established.

2.2 Ground Motion Characterization

To characterize the ground motions at a specified site as a result of the seismic sources considered in the PSHA and DSHA, we used empirical GMMs for spectral accelerations. The models used in this study were selected based on the appropriateness of the site conditions and tectonic environment for which they were developed (Figure 6; Section 4.2).

Ground motions are generally assumed to be lognormally distributed. However, studies (e.g., GeoPentech, 2015) have demonstrated that ground motions deviate from the generally assumed lognormal distribution at epsilon (ε) values greater than about 2.5, where ε is the number of standard deviations above or below the median ground motion intensity. As part of the Southwestern United States Ground Motion Characterization SSHAC Level 3 study (GeoPentech, 2015), residuals for the Next Generation of Attenuation (NGA)-West2 models were examined at

various epsilon values, and it was determined that the within-event residuals had “fat tails” in that there was a higher probability of extremes (at both high and low epsilon) than predicted by a lognormal distribution. To adequately model these fat tails, a mixture model was developed, which consists of two equally weighted lognormal distributions: one model having a mean of zero and log standard deviation of 0.8 times sigma (from the individual GMMs) and the second model having a mean of zero and log standard deviation of 1.2 times sigma. The mixture model was implemented in this study for both the NGA-West2 and NGA-Sub GMMs. Five standard deviations about the median value were included in the analysis.

3.0 SEISMOTECTONIC SETTING AND HISTORICAL SEISMICITY

The seismotectonic setting and the historical seismicity of the site region are described below.

3.1 SEISMOTECTONIC SETTING

Alaska is one of the most seismically active parts of the U.S. (Figures 1, 2, and 5). Earthquakes in southern Alaska result primarily from interactions between the Pacific and North American plates (Figure 7). Northwestward motion of the Pacific plate relative to the North American plate is accommodated by subduction of the Pacific plate at the Alaska-Aleutian megathrust and by dextral transform faulting in southeastern Alaska on the Queen Charlotte and Fairweather fault zones (Figure 4). Most damaging earthquakes in Alaska have occurred on the main megathrust plate boundary interface. Zoback and Zoback (1991) state that the direction of principal maximum stress in the Aleutian subduction zone area is north-northwest, consistent with direction of relative motion between the Pacific and North American plates. Convergence across the Alaska-Aleutian trench in the eastern part of the subduction zone, where Anchorage lies, occurs at a rate of about 5.4 cm/yr, and transform motion occurs at a slightly slower rate across the transform boundary to the southeast (Demets and Dixon, 1999). The eastern end of the subduction zone is complex because of the change from subduction, where the plates converge nearly perpendicularly, to the transform boundary defined by the Queen Charlotte and Fairweather fault zones (Figure 4).

Earthquakes occur in several settings within the subduction zone: (1) bending-moment normal fault events in the Pacific plate near and seaward of the trench, (2) megathrust earthquakes that have a maximum depth of seismic coupling of about 35 to 40 km (Tichelaar and Ruff, 1993), (3) events within the down-going slab (Wadati-Benioff zone) to depths of about 150 km in the Gulf of Alaska region (Davies and House, 1979), and (4) within the upper North American plate, north of the plate interface. Davies and House (1979) and Tichelaar and Ruff (1993) argue that low levels of seismicity in the megathrust zone to about 40 km depth suggests that these shallow zones are dominated by great earthquakes and their aftershocks, with little inter-event seismicity. Conversely, the Wadati-Benioff zone below about 40 km shows relatively continual seismicity. Earthquakes within the Pacific plate, south of the Aleutian trench, are relatively rare.

The area of collision where the subduction and transform systems merge includes what Perez and Jacob (1980) call the Yakutat block (microplate). In this region, the Aleutian trench shallows and the plate boundary turns southeast along the Transition fault, the southwestern boundary of the Yakutat block (Figures 4, 5, and 7). The Yakutat block is tightly coupled to the Pacific plate; it moves northeastward at about 5 cm/yr in a direction about 10 to 20 degrees to west (counterclockwise) of the Pacific plate's direction. Northeast of the Transition fault, at the Yakutat block's eastern margin, the block is separated from the North American plate by the right-lateral Fairweather-Queen Charlotte fault system (Figure 4). The northwestern part of the Yakutat block is subducted beneath the North American plate, and it, along with the Pacific plate, dip more shallowly than the Pacific plate dips farther to the west (Brocher *et al*., 1994).

The Denali fault defines the northeast boundary of the Saint Elias block, and farther to the north it separates the Wrangell block from the North American plate (Plafker *et al*., 1994). The Denali fault is predominantly a right-lateral strike slip fault. It lies within and is parallel to the active transpressional Alaska Range orogen for much of its length across south-central Alaska (Bemis *et al.,* 2015). The Totschunda fault system is a younger right-lateral splay of the Denali fault system that separates the Saint Elias and Wrangell blocks (Plafker *et al*., 1994; Bemis *et al.,* 2015). It has a slip rate of between 10 and 20 mm/yr (Plafker *et al*., 1994). To the north and west, the Denali fault curves to a more westerly and then southwesterly strike (Figures 3 and 4). At the longitude of Anchorage, the Denali fault strikes to the southwest and the Castle Mountain and Lake Clark faults, south of the Denali fault, roughly parallel it (Figure 3). The epicenter of the 2002 **M** 7.9 Denali earthquake was north-northwest of Anchorage, near where the Denali fault changes from a northwest to a northeast strike (Figure 1).

The site is located near the northeastern corner of the Cook Inlet, a forearc basin bounded by the Kenai Mountains to the southeast, the Aleutian Range to the west, and the Caste Mountain fault along its northeastern margin. The basin is characterized by numerous northeast and north-trending folds that have accommodated Tertiary and Quaternary shortening related to subduction of the Pacific Plate. Haeussler *et al*. (2000) indicate that much of the shortening is Pliocene and younger. Several of the Cook Inlet folds are included in the crustal source model and represent some of the closest sources to the Port of Alaska (POA). Because many of the sources are offshore and/or do not clearly fault postglacial surficial deposits, slip rates for the associated faults carry broad uncertainties.

3.2 Historical Seismicity

The Alaska subduction zone experienced four great earthquakes in the 20th century, including three of the largest earthquakes of the century. From east to west, these included the 1964 Great Alaska earthquake (**M** 9.2), the 1938 earthquake off the Alaska Peninsula (**M** 8.2), the 1957 Andreanof earthquake (**M** 9.1), and the 1965 Rat Island earthquake (**M** 8.7).

The project seismicity catalog was obtained from the USGS and is a subset of a preliminary catalog for use in the National Seismic Hazard Map Project update of the Alaska seismic hazard maps (USGS, 2021). The catalog, which spans the period of 1882 through December 2020, was compiled from the USGS ComCat and GSCanada catalogs and encompasses a region extending over 500 km around the project site (Figure 1).

Events in the 2021 USGS compilation were provided with magnitudes of type “expected **M**” (E[**M**]), which is derived from either (1) “observed” **M** from inversion of long-period waveforms or surface-wave spectra, (2) magnitude types Richter local magnitude (M_L) and duration magnitude (M_D) assumed equivalent to **M**, or (3) magnitude types converted to **M** following EPRI/DOE/NRC (2012) (Petersen *et al*., 2014). *N** values were provided for earthquakes in the 2021 USGS compilation. Instead of using the observed number of earthquakes for recurrence calculations, *N** values are used to estimate unbiased recurrence parameters (EPRI/DOE/NRC, 2012).

The final project seismicity catalog represents a catalog of E[**M**] ≥ 3 earthquakes in the greater project region. In the figures and text of this report, we commonly refer to these magnitudes as **M** rather than E[**M**] for simplicity.

3.2.1 Significant Earthquakes

The following describes the significant earthquakes within 200 km of the site (Figure 1) and the 2002 Denali earthquake (Figure 5).

Pre-Instrumental Seismicity

Instrumentation in Alaska was sparse prior to the 1964 Great Alaska earthquake. At the time there were only two instruments: at Sitka installed in 1904 and the University of Alaska at Anchorage installed in 1935. After the 1964 earthquake, four more instruments were installed by 1996 creating the regional network in central and southern Alaska (Page *et al*., 1991). In 1967 the Alaska Tsunami Warning Center was established with six instruments to respond to the pressing need for detecting potentially tsunamigenic earthquakes (Page *et al*., 1991).

Instrumental Seismicity

The 1964 earthquake introduced the need for more instrumentation in the Alaska region, including the Aleutian Islands. By the early 1970's, continental Alaska had over 40 instruments. With the onset of oil exploration in the late 1970's, there were at least four 17-station regional networks in operation at one time (Page *et al*., 1991). The USArray Temporary Array project installed 197 temporary seismic stations throughout Alaska between 2014 to 2017, 107 of which were acquired as permanent stations by the Alaska Earthquake Center between 2019 to 2020, and are operated by the Alaska Earthquake Center, the Arctic Observing Network Program, and the Alaska Volcano Observatory (AEC, 2022). There are currently about 250 stations in the Alaska Regional Seismic Network (Ruppert *et al*., 2022).

There are 2,135 earthquakes of **M** ≥ 3.5 within 200 km of the site with 159 of **M** ≥ 5.0 (Figure 1). There have been five events of **M** ≥ 7.0 within 200 km of the site (Figure 1). The closest significant earthquake, approximately 13 km northwest of the site, occurred on 30 November 2018 (Figure 2). An earthquake of **M** 7.6 in 1943 occurred 86 km northwest of the site.

3 November 1943 M 7.6 Earthquake

The 3 November 1943 **M** 7.6 earthquake was felt in Anchorage, McGrath, and Bethel. In Anchorage, doors swung and windows rattled (Bodle, 1945). In Bethel, the community closest to the epicenter, the ground shaking lasted 20 seconds and buildings swayed. Ice from nearby frozen lakes and streams cracked for an hour after the shock (Bodle, 1945).

25 June 1951 M 6.3 Earthquake

The closest significant earthquake aside from the 2018 **M** 7.1 earthquake occurred on 25 June 1951 approximately 20 km southwest of the site (Figure 2). The **M** 6.3 earthquake caused light fixtures to sway, parked cars to jump, and containers to fall from top shelves (Murphy and Cloud, 1953). The local radio station reported the phonographs rolled out of their files. The event was also felt in Cordova, Palmer, and Spenard, where the strongest shaking was felt (Murphy and Cloud, 1953).

1964 Great Alaska Earthquake

The Great Alaskan **M** 9.2 earthquake of 28 March 1964 was one of the most violent earthquakes on record and possibly the second largest earthquake ever recorded (Kanamori, 1977). The earthquake was felt over 1.8 million km^2 in Alaska, and the Yukon Territory and British Columbia, Canada (Figure 8; Hake and Cloud, 1966). Rupture initiated about 100 km east of Anchorage along the Prince William Sound asperity (e.g., Christensen and Beck, 1994; Johnson *et al*., 1996). The source mechanism for the 1964 earthquake is sinistral-reverse slip with a displacement of about 20 m. The maximum resulting surface displacements were on the order of 10 m in Prince William Sound with smaller amounts of subsidence on the Kenai Peninsula towards Anchorage (Plaflker, 1969). Surface deformation was noted over a zone about 140 km wide.

The greatest amount of damage from the earthquake occurred in Anchorage, which recorded a Modified Mercalli (MM) intensity VIII (Figure 8; Stover and Coffman, 1993). Numerous landslides, rockslides, and avalanches were triggered from the strong ground shaking felt in the area. In addition, fractures and cracking developed in unconsolidated deposits, while mud spouts, slumping, and boils were observed in areas of compaction (Hake and Cloud, 1966). Observers in Anchorage documented shaking lasting between 4 to 5 minutes. There were 15 deaths attributed to the earthquake and another 113 following the related tsunami (USGS, 2008). The most destruction was attributed to four major landslides, two of which were near the Port; one at L Street, and the second at Turnagain Heights. The L Street slide was over 244 m wide and 0.8 km long with shearing at the base, causing buildings to slide off foundations and buildings at the head of the slide to topple over (Hake and Cloud, 1966). The Turnagain Heights slide was larger, 300 m by 2.4 km, leaving a 15 m vertical scarp. Over 70 homes were destroyed by the slide at Turnagain Heights (Hake and Cloud, 1966).

30 November 2018 M 7.1 Anchorage Earthquake

The 2018 **M** 7.1 Anchorage earthquake occurred approximately 13 km northwest of the site at a depth of 47 km within the subducting slab and was consistent with Pacific plate extension (West *et al.*, 2019) (Figure 2). Within the first six months following the mainshock, approximately 300 felt aftershocks (including 24 events of **M** > 4.5) were recorded. West *et al.* (2019) stated that strong to severe shaking was felt by over half of Alaska's population, though the most violent shaking was not felt due to the earthquake's depth. Moderate to strong shaking spanned a broad region,

with the highest reported peak horizontal ground acceleration (PGA) value of 0.5 g and PGA values of 0.25 g were reported across an area of > 8,000 km^2 (West *et al.*, 2019). The estimated ground shaking at the Port was MM VII (Figure 9).

Grant *et al.* (2020) documented observations of ground failure caused by the event by creating an initial inventory of liquefaction, landslides, crack traces, and incipient landslides. They found that landslides triggered by the 1964 Alaska earthquake did not reactivate with significant downslope movement (extensional cracks 1 to 2 cm wide) as a result of the 2018 event, and that most landslides and liquefaction observed had permanent deformation less than approximately 20 cm (Grant *et al.,* 2020). However, flow slides within highway fill, widespread lateral spreading and/or riverbank slumping, and extensional cracking and possible incipient landslides were noted in other locations (Grant *et al.,* 2020). In general, based on the magnitude of the 2018 event alone, less ground failure over a smaller spatial area occurred than would have been expected; this is likely due to the focal depth and mechanism of the event (Grant *et al.,* 2020).

3.2.2 Local Seismicity

Within 50 km of the Port, there are 363 events of **M** ≥ 3.5, 145 events of **M** ≥ 4.0, 69 events of **M** ≥ 4.5, 31 events of **M** ≥ 5.0, 11 events of **M** ≥ 5.5, and four events of **M** ≥ 6.0 (Figure 1). The closest event to the Project area was an **M** 3.7 earthquake that occurred on 12 February 2019 approximately 4 km northwest of the Port (Figure 1). The largest event within 50 km of the Port was the 2018 **M** 7.1 earthquake approximately 13 km northwest of the Port (Figure 1).

4.0 INPUTS TO ANALYSES

The following section discusses the characterization of the seismic sources and the GMMs implemented in the PSHA and DSHA.

4.1 SEISMIC SOURCES

Seismic source characterization is concerned with three fundamental elements: (1) the identification, location, and geometry of significant sources of earthquakes; (2) the maximum size of the earthquakes associated with these sources; and (3) the rate at which the earthquakes occur. The seismic source model includes crustal faults capable of generating large surface-faulting earthquakes within about 100 km of the Port as well as faults with particularly high slip rates between 100 to 200 km of the Port site (Section 4.1.1), background crustal seismicity that cannot be attributed to identified faults explicitly included in the seismic source model (Section 4.1.3), and potential earthquakes associated with the megathrust and intraslab zones of the Alaska subduction zone (Section 4.1.4).

4.1.1 Crustal Fault Sources

Fault parameters required in the PSHA include: (1) rupture model (including independent single plane and potentially linked models); (2) probability of activity; (3) fault geometry including rupture length, rupture width, fault orientation, and sense of slip; (4) maximum or characteristic magnitude [Mmax]; and (5) earthquake recurrence including both recurrence model and rates. These parameters are discussed generally below. Selected seismic sources that contribute the most to the hazard are specifically discussed in subsequent sections. We have explicitly incorporated the uncertainties in each parameter through logic trees, as shown in Figure 6.

The seismic source characterization of faults used in this study is based principally on Alaska fault data compiled in the 2013 USGS Quaternary Faults and Folds database (Koehler *et al*., 2012, 2013), and the 2023 Alaska National Seismic Hazard Model (NSHM; Bender *et al*., 2021a, 2021b). In addition, LCI reviewed previous PSHA studies relevant to the study area (Wong *et al*., 2008; 2014), as well as fault-specific publications, such as Haeussler and Saltus (2011), Willis *et al*. (2007), Haeussler *et al.* (2017), and Liberty *et al*. (2013). The seismic source model also incorporated information from email correspondence with Peter Haeussler, a leading expert familiar with the geologic and seismotectonic setting in the study. Each seismic source is characterized using the latest geologic, seismological, and paleoseismic data and the currently accepted models of fault behavior. All known active or potentially active faults within 200 km of the Port were included in the analyses (Figure 10). We included faults that we judge to be at least potentially active and that would potentially contribute to the probabilistic hazard because of their maximum earthquakes and/or proximity to the site. Table 1 shows the parameters for the crustal faults included in the source model.

Faults are generally modeled as single, independent, planar sources (Figure 10). We calculate preferred maximum earthquake magnitudes using the empirical relationships from Wells and

Coppersmith (1994) for magnitude-rupture length (all faults), and Leonard (2010) for area, weighted equally. Rupture area is calculated from rupture length and width; rupture length estimates are straight line end-to-end distances taken from mapped fault lengths and widths are the down-dip extent of the planar fault.

Based on the observed focal depths in the modern portion of the historical record, assumed seismogenic depth ranges are somewhat variable. In general, maximum seismogenic thickness falls in the range of 10 to 25 km, with minimum depth assumed to be zero unless otherwise noted. Specific depth ranges are noted in Table 1.

In these analyses, we model all faults as planar sources that extend the full extent of the seismogenic crust. Thus, fault dips are averages estimated over the seismogenic crust. Near-surface and crustal fault dip data were available for many of the faults included in the source characterization. Sources with oblique or lateral slip components typically have steep dip values of 75 to 90° (weighted 0.6) ± 15-20° (weighted 0.2). Faults with primarily dip slip components are assigned fault dips based on their interpreted style of faulting and any available data to constrain dip (Table 1).

In assigning probabilities of activity (P[a]) for each fault source, we considered both the likelihood that the structure exists and is capable of independently generating earthquakes (i.e., is seismogenic), and the likelihood that it is still active within the modern stress field. We incorporated many factors in assessing these likelihoods, such as: orientation relative to the modern stress field, fault geometry (length, continuity, depth extent, and dip), relation to other faults, age of youngest movement, geomorphic expression, amount of cumulative offset, rates of activity, similarity to known active faults, and any evidence for a non-tectonic origin. Faults with definitive evidence for repeated Quaternary activity were generally assigned probabilities of being active and seismogenic of 1.0. Exceptions include faults that may be secondary and dependent on other faults, and faults that do not show definitive evidence for repeated Quaternary activity. Resulting probabilities range from 0.2 to 1.0 (Table 1). The Patton Bay and Montague Strait faults, while clearly active, are both assigned P(a) values of 0.2 to represent their potential rupturing independently of the subduction zone as capable seismic sources.

As recurrence interval data are generally lacking for local faults, we used slip rates to characterize rates of fault activity (Table 1). Based on available GPS velocity data and deformed Quaternary landforms, there are reasonable constraints on slip rate for sources in the region. Preferred slip rate values typically range from 0.05 mm/yr to 11.0 mm/yr (Table 1).

The uncertainty in the slip rates and the other input parameters is accommodated in the PSHA through logic trees (Figure 6). Uncertainties in determining recurrence models can significantly impact the hazard analysis. We considered the maximum magnitude and characteristic recurrence models for the fault sources. Observations of historical seismicity and paleoseismic investigations along faults in the western U.S. (e.g., San Andreas fault) suggest that characteristic behavior is more likely for individual faults (Schwartz and Coppersmith, 1984). Therefore, for most

fault sources, we favored the characteristic model (weight of 0.7), while the maximum-magnitude model was weighted 0.3.

A total of 19 seismic sources were characterized in this study; each is described in detail in Table 1 and shown on Figure 10. The majority of these sources form three types of tectonic structures that accommodate regional transpression and block rotations, and contribute to seismicity in the study area:

1. *Steeply dipping, right-lateral strike-slip faults* (the Denali, Castle Mountain, Lake Clark), accommodating dextral deformation of southern and interior Alaska associated with the Yakutat plate convergence. We consider several rupture models for these and other sources that include, floating, full, and segmented ruptures. Additionally, we utilized a layered approach for the Castle Mountain fault to better accommodate along-strike slip rate variation. (The Lake Clark fault has been recently declassified as a Quaternary fault - Peter Haeussler, USGS, verbal communication, Nov 2022).

2. *Variably oriented faults located between the Denali and Castle Mountain faults* (e.g., Broad Pass, Kahiltna, Leech Lake, Pass Creek), that collectively accommodate shortening and rotation between the two dextral fault zones.

3. *Low angle, northeast-striking thrust faults associated with fold growth/shortening in the Cook Inlet* (e.g., Kenai lowlands, Middle Ground Shoal, Lewis River). These sources represent causative faults for the numerous faults in the Cook Inlet region.

Significant Fault Sources

The following summarizes the significant crustal fault sources included in the seismic source model. Summaries for other fault sources not discussed below are included in Table 1.

Castle Mountain – Caribou Fault System

At a distance of 38 km from the Port, the Holocene-active Castle Mountain – Caribou Fault System is the closest fault source to the site with a preferred slip rate greater than 1mm/yr. Based on mapping by Detterman *et al*. (1976) and seismicity analysis following the 1984 m_b 5.7 earthquake and aftershock sequence (Lahr *et al*., 1986), the fault likely dips approximately 70° to 90° north. Willis *et al.* (2007) documented post-last glacial maximum (LGM) displacements along the western section of the fault zone and calculated dextral slip rates that ranged from 2.1 to 3.6 mm/yr with no more than a few meters of vertical displacement. More recent work in preparation for the Alaska hazard map update presented by Tape and Haeussler (2019) documents mostly vertical deformation along the fault from detailed topography review. However, based on the focal mechanisms (e.g., Lahr *et al.,* 1986), near-vertical fault, evidence for limited shortening related to the last three or four events (Haeussler *et al*., 2002), and evidence for primarily lateral displacement (Willis *et al*., 2007, this study), we model the fault as primarily strike-slip. Along the Holocene active section, our review of the LiDAR-based 10-m digital elevation model (DEM) found

an obvious and remarkably linear to curvilinear series of scarps that each extend largely unbroken for many kilometers. These scarps are typically several meters high and almost exclusively display down-to-the-southeast displacement. The section with unequivocal post-LGM morphology extends for at least 62 km (modeled as 80 km given limitations of fault visibility at east and west ends) and has a midpoint that is nearly the closest approach of the fault to the POA.

En-echelon left-steps along the fault are locally abundant. Additionally, the few locations of clear left (restraining) and right (releasing) steps are associated with localized graben and/or bulges interpreted to represent localized extension and shortening, respectively. These features are consistent with a dextral fault accommodating some oblique shortening on a north-dipping structure.

Based on evidence for repeated Holocene activity along the Western section (recurrence interval of ~700 years), with only Pleistocene activity identified on the Eastern section (Haeussler *et al*., 2002), we consider a layered model for the Castle Mountain fault. This is the only fault in the Anchorage area (< 50 km) with both a constrained slip rate and a constrained Late Holocene earthquake chronology. The fault has ruptured four times during the past 2,700 years (Haeussler *et al*., 2002). To adequately model hazard along the highest rate section of the Castle Mountain, we utilize two segments in a layered format for the western section; the geomorphically youthful 62-km section carries 75% of the total western section target rate while the full western section carries the remaining 25% (distributed over two layers), resulting in overlap section carrying the full rate of 0.5, 3.0, and 4.0 mm/yr, respectively (Figure 11). Because of the apparent along-strike continuity of the fault in map view between the Western and Eastern sections, we also include a floating rupture model that is allowed to rupture anywhere along the fault system. However, this is given a relatively low weight (Table 1) because of the paleoseismic record that clearly shows the Western Castle Mountain fault has repeatedly ruptured during the Holocene, while the Eastern Castle Mountain (Caribou) fault has not. This is consistent with the clear morphology along the western section and apparent lack thereof on the eastern section. Due to this apparent lack of recent activity, and the suggestion that the slip rate should decrease to the east due to being on the edge of the Yakutat – North America collision that may drive the Castle Mountain fault, we assign the Eastern Castle Mountain – Caribou Fault System a lower, preferred, and maximum slip rate compared to the Western Castle Mountain fault (Table 1).

Cook Inlet Faults

Because the Cook Inlet faults are largely offshore and/or are blind, comparatively little is known about the activity and strain rates of the faults responsible for the Cook Inlet folds. The proximity of these structures to the Port of Alaska makes them, next to the Castle Mountain fault, the closest shallow crustal seismic sources (Figure 10). Haeussler *et al*. (2000) suggest that these faults may present a greater short-term hazard than 1964-type subduction zone earthquakes. Our source characterization includes eight structures capable of **M** ≥ 6.5 earthquakes and identified by Haeussler *et al*. (2000) and Haeussler and Saltus (2011) as Quaternary-active or potentially Quaternary-active (Table 1). P(a) ranged from 0.3 to 1.0. We also include the Turnagain Arm

structure because it is the closest potentially Quaternary-active structure to the site (Figure 10). Because very little additional information about these structures exists with which to characterize them, we mostly adopt the source parameters of Haeussler *et al*. (2000), who measured the structure lengths in their dataset and used the magnitude versus rupture length relationships of Wells and Coppersmith (1994) to calculate preferred earthquake moment magnitudes. In some instances, where the on-trend continuity of two or more structures suggests they have a potential to rupture together, we have combined the structures and calculated a preferred maximum magnitude. Haeussler *et al*. (2000) note that, although the base of the seismogenic crust may be as deep as 35 km, they do not believe that these faults extend to this depth.

Denali Fault

The Denali fault system is a zone of right-lateral faulting that extends in a broad arc across south-central Alaska (Figures 3 and 4) and accommodates relative motion between North America and the Yakutat Block to the south. This fault system has at least 38 km of total offset during the past 38 my (Reed and Lanphere, 1974) and geomorphic evidence of Holocene activity is clear along much of the fault (Plafker *et al*., 1977). Historically, the most notable large earthquake along the fault is the 2002 **M** 7.9 Denali fault earthquake, that ruptured about 320 km of the central Denali fault and part of the Totschunda fault (Eberhart-Phillips *et al*., 2003; Figure 3). A **M** 7.2 to 7.4 earthquake in 1912 is also thought to have ruptured the central Denali fault (Carver *et al*., 2004; Figure 1).

Following the 2002 earthquake, new research has provided slip rates along the central Denali fault and shows that the late Pleistocene – Holocene slip rate is as much as 12.1 ± 1.7 mm/yr and decreases westward to 9.4 ± 1.6 at longitude ~148.6° W. This slip rate gradient is due to the partitioning of slip from the Denali fault to thrust faults north and west of the Denali fault (Matmon *et al*., 2006). Additional evidence of a decreasing slip rate is also documented by Mériaux *et al*. (2009), who report a Holocene slip rate of about 6.7 ± 1.2 mm/yr at Bull Creek, located on the McKinley strand of the Denali fault in Denali National Park at longitude ~149°26’ W. The site is about 50 km west of the westernmost Matmon *et al*. (2006) study site. Although the Denali fault system has been mapped extending through western Alaska to the Bering Sea, the end of the active fault is regarded to be at about 154.7° W (Wesson *et al*., 2007).

The model considers the central segment of the Denali fault closest to 2002 Denali fault earthquake. The approving 400 km-long Denali Center segment is based on the segmentation scheme in the 2023 NSHM fault database (Bender *et al*., 2021a), which divides the strand into a “Denali (center)”, “Denali (center, east)” and “Denali (center, west). The segment bisects the Alaska Range, and many of the highest peaks, including Mt McKinley, are located south of the fault.

Preliminary results of paleoseismic studies along the section of the fault west of the 2002 rupture suggest that the most recent earthquake (MRE) was relatively recent based on geomorphically fresh fault scarps and radiocarbon dating that constrains the MRE to have occurred in the past

250 years (Schwartz *et al*., 2005). Paleoseismic trenching and radiocarbon dating also show prior events occurred in 1912 (Carver *et al*., 2004) and 570 to 680 yrs B.P., suggesting that the fault has a recurrence interval on the order of several hundred years between large earthquakes (Schwartz *et al*., 2005).

We consider two rupture scenarios in our seismic source model based on information from the 2002 and penultimate events on the central section. The first scenario represents a 340-km floating rupture and based on the 2002 Denali earthquake, which ruptured about 340 km of the central Denali fault (Eberhart-Phillips *et al*., 2003). In the case of the 2002 rupture, it has been implied that the endpoints of the rupture were largely controlled by the timing of the most recent event along the unruptured parts of the fault adjacent to the 2002 rupture (Schwartz *et al*., 2005). The second rupture model is also a floating source that is based on tree-ring evidence for surface rupture along the central segment in 1912 (Carver et al., 2004). The year is coincident with the 1912 low **M** 7 Delta River earthquake that damaged trees along a portion of the same section that ruptured in 2002. Identification of this smaller event demonstrates considerable magnitude variability along the Central section of the Denali fault.

4.1.2 Crustal Background Earthquakes

In state-of-the-practice seismic hazard evaluations, the hazard from background earthquakes is addressed. Background earthquakes are those events that do not appear to be associated with known geologic structures. They occur on crustal faults that exhibit no surficial expression (buried faults) or are unmapped due to inadequate studies. In this source characterization, we address the hazard from crustal background earthquakes through two crustal seismic source zones adopted and modified from the 2023 Alaska National Seismic Hazard Model (NSHM; Bender *et al*., 2021a): (1) the Southern Alaska Block and Cook Inlet source zone (SABCI); and (2) the Yakutat Block source zone (YB) (Figure 12). These seismic source zones were defined based on the tectonic and geologic characteristics, focal mechanisms, styles of faulting, and observed alignments in historical seismicity of each zone. To address the hazard from these crustal source zones, we considered two models: (1) a gridded seismicity model, where locations of past seismicity appear to be likely locations of future seismicity (stationarity); and (2) the use of regional seismic source zones, where earthquakes are assumed to occur randomly ("uniform" model). For both approaches, the background earthquakes are assumed to occur uniformly from 2 km to the bottom of the seismogenic crust. Each source zone has three branch values for the maximum depth of the seismogenic crust: 10, 15, and 20 km with weights of [0.2], [0.6], [0.2], respectively, for the SABCI source zone, and 18, 23, and 28 km with weights of [0.2], [0.6], [0.2], respectively, for the YB source zone. These values were estimated based on hypocentral depths of earthquakes in the project earthquake catalog, as well as judgement. To mirror the style of faulting of crustal fault sources within each source zone, the SABCI source zone was modeled with a combination of reverse and strike-slip styles of faulting weighted at [0.7] and [0.3], and the YB source zone was modeled with full weight to reverse style of faulting.

Earthquake recurrence estimates in the site region are required to assess the hazard from background earthquakes. The recurrence parameters for the source zones were developed using the project earthquake catalog for the period of 1841 through June 2021 (Section 3.2). Crustal and intraslab earthquakes in the historical record were separated using the Slab2 model of Hayes *et al*. (2018). We considered the completeness intervals from the 2007 USGS Seismic Hazard Maps for Alaska (Wesson *et al*., 2007) and subsequently revised them using Tinti-Mulargia plots (Tinti and Mulargia,1985). Completeness estimates and number of earthquakes by magnitude bin are listed in Table 2.

The catalog was declustered by the USGS using the Gardner and Knopoff (1974) algorithm to remove dependent earthquakes (i.e., foreshocks and aftershocks). Additional aftershocks were removed by the USGS from several very large earthquakes using published aftershock areas. All seismicity (regardless of depth) within 5 km of the surface trace of the Denali, Castle Mountain, and Lake Clark faults was considered fault-related and removed from the declustered catalog used in this study. Removal of fault-related crustal earthquakes for other faults in the crustal source model was not performed due to the difficulty of identifying such events because of location uncertainty and defining the down-dip geometries of the faults. Hence, there is potentially some double-counting and the hazard from background earthquakes may be conservative. As testing of the source model indicated that the intraslab and megathrust are the sources controlling hazard, we expect the effect of this double counting to have a minimal impact on the overall hazard results.

Both seismic source zones have five branch values for Mmax of **M** 6.75, **M** 6.875, **M** 7.0, **M** 7.125, and **M** 7.25 with weights of [0.101], [0.244]. [0.310], [0.244], and [0.101], respectively, that are based on a five-point approximation of a continuous uncertainty distribution (Miller and Rice, 1983). The five values are intended to capture almost two standard deviations and the median value of a normal probability distribution. The Mmax values for each source zone are highly uncertain based on incomplete knowledge of fault connectivity, rupture potential, and the relatively short duration of the historical earthquake record. This uncertainty is reflected in the selection of the five-point uncertainty distribution that spans 0.5 magnitude units. The Mmax values represent estimates of the largest expected earthquake within each source zone that will not occur on a recognized and separately modeled fault source. Generally, Mmax values are selected that exceed the largest known “background” earthquake within the source zone and, to some extent, the largest known “background” earthquake in similar seismotectonic environments globally.

Recurrence parameters (*b*-values and rates) were calculated using the background earthquake catalog and the program ABSMOOTH (LCI proprietary software; EPRI/DOE/NRC, 2012). The ABSMOOTH program computes a *b*-value for the source zone then divides the source zone into cells of a selected size (0.2-degree cells in this report) and calculates the rate in each cell using the likelihood function of the data in that cell along with penalty functions that smooth the cell-to-cell variation in the rate. The program outputs both mean values and eight alternative sets (“realizations”) of the recurrence parameters to characterize epistemic uncertainty in the rates and *b*-values (EPRI/DOE/NRC, 2012). This approach is based on the Markov Chain Monte Carlo

techniques to generate multiple realizations from a multi-dimensional probability distribution – in this case, rate, *b*-value, and uncertainty in those parameters. The equally weighted eight alternative maps of rates and *b*-value represent the central tendency and statistical uncertainty in the recurrence parameters and are selected using the Latin Hypercube sampling technique. Eight realizations are used to provide a good representation of the underlying distributions (EPRI/DOE/NRC, 2012).

Table 3 provides the rates of events for **M** 5 and above and the corresponding *b*-values for use in the PSHA. For the SABCI zone, *b*-values range from 0.52 to 0.65, with corresponding total rates of 0.22679 and 0.11685. For the YB zone, *b*-values range from 0.66 to 0.93, with corresponding total rates of 0.09891 and 0.03369. Figures 13 and 14 show example the recurrence curves for the range of *b*-values for **M** ≥ 5 for the weighted mean Mmax (**M** 7.0) for the SABCI and YB source zones, respectively, compared to the independent historical seismicity (also accounting for completeness). For the SABCI, recurrence calculations were performed using historical data for **M** 3.0 and greater. For the YB, recurrence calculations were performed using historical earthquake data for **M** 3.5 and greater. In the latter case, recurrence curves that incorporate the 3 ≤ **M** < 3.5 historical data tend to result in higher *b*-values and curves that appear to underestimate the rate of **M** 5.0 and greater (curves not shown). To avoid this possible underestimation, recurrence calculations for the YB zone were performed using only data for **M** 3.5 and greater, with the resulting curves shown on Figure 14.

Figures 15 and 16 show the gridded seismicity results generated from ABSMOOTH for the SABCI and YB source zones, respectively. Recurrence parameters for the uniform seismic source zones were adopted from the eight realizations generated for the gridded seismicity, such that the total rates generated for each realization were assumed to apply uniformly across each source zone. On Figures 15 and 16, the total rate averaged over the area of the SABCI and YB zone, respectively, is labeled on the rate scale bar for each realization shown. For the SABCI zone (the "host" zone for the Port site), the average rate is generally higher than or similar to the gridded rate for the cells closest to the Port (Figure 16). This result is consistent with the distribution of independent earthquakes within the zone, where the majority of events are located north of the Port site.

An inspection of the resulting recurrence intervals for **M** 5 and 6 events was performed to check the reasonableness of the eight *b*-values and rates for each of the source zones. To do this, using the weighted mean Mmax value (**M** 7.0) and the eight realizations of the recurrence parameters, the resulting recurrence intervals were evaluated for each zone. Table 4 lists the recurrence intervals for **M** 5 or greater and **M** 6 or greater events for each seismic source zone. For the SABCI zone, the estimated recurrence interval for events of magnitude **M** 5 or greater ranges from approximately 4 to 9 years; for events of **M** 6 or greater, the recurrence interval ranges from approximately 19 to 47 years. For the YB zone, the estimated recurrence interval for events of **M** 5 or greater ranges from approximately 10 to 30 years; for events of **M** 6 or greater, the recurrence interval ranges from approximately 56 to 284 years. These ranges result from the epistemic uncertainty in the recurrence parameters, primarily due to the limited number of historic

earthquakes in the catalog within each zone. This is particularly true for the YB zone, which has 74 independent events compared to the 130 independent events in the SABCI zone.

4.1.3 Alaska Subduction Zone

The Alaska subduction zone, both the megathrust and Wadati-Benioff zone, are described below (Figures 17 through 19).

Megathrust

The Alaska megathrust is defined by a northward-dipping Wadati-Benioff zone at the plate boundary interface. If this zone of seismicity intersected the surface, it would daylight near the Aleutian trench (Figure 7). Large historical earthquakes have ruptured much of the length of this megathrust. The four segments of the subduction zone considered in the PSHA were the Semidi, Kodiak, Prince William Sound, and Yakataga (western Yakataga microplate) (Figure 17). Table 5 lists the seismic source parameters for the megathrust. This segmentation model was generally adopted from the 2007 USGS characterization (Wesson *et al*., 2007). However, we updated the recurrence intervals based on the recent studies by Witter *et al*. (2022) and the geometry of the megathrust interface was adopted from the Slab2 model of Hayes *et al*. (2018).

Near Anchorage, relative motion is compressional and thrust faults predominate, whereas the eastern part of the subduction zone, where plate motion is oblique, is largely a transform boundary. Large historical earthquakes have ruptured much of the length of this megathrust.

The “Eastern section” of the subduction zone includes the Kodiak segment, centered on Kodiak Island, and the Prince William Sound segment (Figure 17). The Prince William Sound and Kodiak segments ruptured in the 1964 Alaska earthquake. Shennan *et al.* (2009), however, suggests that the prior two megathrust events on those segments, at ca. 900 BP and ca. 1500 BP, also ruptured the western part of the Yakutat block, adding about 15% to the seismic moment release compared to 1964.

The Yakutat microplate has been variously described as an oceanic plateau (e.g., Worthington *et al.*, 2012; Christensen *et al*., 2010), an allochthonous fragment of continental terrane (Plafker *et al.*, 1994), and oceanic crust (Brums, 1983). The western part of the block is subducting under the North American plate, whereas the eastern portion meets the North American plate in a collisional regime characterized by accretion and underplating along a series of crustal thrust faults soling into a décollement under the Saint Elias block (Elliott, 2011; Worthington *et al*., 2012). The microplate is buoyant compared to the oceanic crust of the Pacific plate and the subduction is low angle. Veilleux and Doser (2007) use relocated earthquakes to conclude that the subducted Yakutat block is nearly flat in the easternmost part of the subduction zone. Brocher *et al*. (1994) analyzed wide-angle seismic reflection and refraction profiles and determined it is dipping 3 to 4 degrees. The 2007 National Seismic Hazard Map model for Alaska, acknowledging the complexity of the Yakutat region, simplified it to include the Yakutat microplate as a subduction zone source, the Yakataga segment. It was characterized in that model as a flat surface at 15 km

depth. More recently, Elliott (2011) analyzed GPS data and modeled the western Yakutat microplate, from the Bering Glacier west, subducting with a 5-degree dip and extending at least 200 km to the northwest under Prince William Sound.

The subduction of the Yakutat microplate and its interaction with the subducting Pacific plate are complex and poorly understood. Based on the Elliott (2011) model, however, the subducting Yakutat plate underlies much the same region as the northeastern part of the subducting Pacific slab. Freymueller *et al*. (2008) argue that the Yakutat plate subducts under the north American plate at a very shallow dip while the Pacific plate subducts at a slightly steeper dip under the subducting Yakutat slab, yielding two separate but overlapping subduction interfaces. Brocher *et al*. (1994) argue that there are not two Wadati-Benioff zones and rather the Yakutat and Pacific plates subduct together as a composite plate. Given the complexity, different interpretations, and distance from the site, and in light of the paleoseismic data suggesting the western Yakutat microplate has ruptured with the Prince William Sound and Kodiak segments of the Pacific plate in single event, in this model of the subduction zone, we simplify the region and combine the western Yakutat microplate megathrust with the Prince William Sound megathrust into a single segment (PWS/WY), capable of rupturing together. In this model, the 1964 rupture would represent a partial rupture of the segment, or an event somewhat smaller than the maximum event, while the 900 BP and 1500 BP events would represent full rupture events.

In the model of the subduction zone, we include two rupture models for the Eastern section (Table 5). In the “unsegmented” model, the PWS/WY and Kodiak segments rupture together in 1964-like earthquakes. In the segmented model, PWS/WY and Kodiak rupture independently. Paleoseismic data through nine events in the Prince William Sound area and through five or six events in Kodiak indicate that earthquakes in both segments occurred at the same time within the uncertainties of radiocarbon ages (Carver and Plafker, 2008; Hutchinson and Crowell, 2007). This leads us to favor the unsegmented model, but we give moderate weight to the segmented model because the paleoseimic events could represent independent ruptures in relatively rapid succession (Table 5).

Geodetic modeling of the megathrust indicates a very shallow dip (Figure 19). In a joint inversion of tsunami waveforms and geodetic data, Johnson *et al*. (1996) model the Prince William Sound segment as dipping 3 to 4 degrees and the Kodiak segment as 8 to 10 degrees. Similarly, Savage *et al*. (1999) model a megathrust as dipping 5 degrees based on geodetic data. Brocher *et al.* (1994) estimate the dip of the megathrust as 9 to 10 degrees based on wide-angle seismic reflection data. Ichinose *et al*. (2007) model the Prince William Sound and Kodiak segments as dipping 12 degrees based on modeling of the 1964 rupture using teleseismic data. At the bottom of the megathrust, the downgoing slab steepens in dip based on relocated seismicity. In the PSHA, we model the megathrust with a dip of 6˚ ± 3˚ for the Kodiak and PWS/WY segments and a slightly steeper dip of 7˚ ± 2˚ for the Kodiak segment. The rupture distance from the Port to the megathrust is 31 km (Figure 18).

The colored area shown on Figure 19 is treated as locked and capable of producing great megathrust earthquakes. The un-shaded part of the slab is greater than 45 km in depth, and is the part that is considered not capable of producing great earthquakes like the subduction zone. Zweck *et al*. (2002) use GPS data to model the locked and slipping parts of the plate interface. They conclude that the present extent of the locked plate boundary closely resembles the area of the interface that broke in the 1964 earthquake. The area to the northwest of this locked patch is experiencing post-seismic creep parallel to the direction of plate motion. The boundary between these locked and creeping patches trends to the northwest and is very near Anchorage. This is also the location where the subducting slab begins to bend and dip more steeply (Figure 19).

The USGS (Wesson *et al*., 2007) cites paleoseismology studies in the eastern part of the megathrust by Plafker and Rubin (1994), Combellick (1994), Bartsch-Winkler and Schmool (1992), Hamilton and Shennan (2005), Hamilton *et al*. (2005), and Shennan and Hamilton (2006) to assign an average recurrence time of 650 years for the Prince William Sound (1964 rupture zone) segment (Table 5). A more recent compilation of paleoseismic data by Carver and Plafker (2008) and Shennan *et al*. (2014), however, suggests a slightly shorter average recurrence interval. Based on the studies of Shennan *et al*. (2014) who identified and dated six “1964”-like earthquakes, we computed an average recurrence interval of 594 years with a standard deviation of 162 years. A mean coefficient of variation (COV) of 0.27 was also estimated from the six recurrence mean intervals, which is a relatively low value compared to the global average of 0.5 indicating relatively periodic behavior (Section 4.1.4).

The USGS also cites evidence in Nishenko and Jacob (1990) and Carver *et al*. (2003) to conclude that the southwestern part of the 1964 rupture zone (the Kodiak Island segment) ruptures separately as well, more frequently than the segment to the east. We allow for the possibility that the Kodiak segment ruptures somewhat more frequently by assigning it a slightly shorter recurrence interval than PWS/WY in the segmented model and, in the “unsegmented” model, by allowing additional ruptures of only the Kodiak segment along with the unsegmented full rupture events (Table 5). Based on the work of Shennan, Witter *et al*. (2022) state that the Kodiak Island segment ruptured at least four times in the past 2,000 years. Hence, we adopt an average recurrence interval of 500 years ± 100 years (Table 5). Rupture of the Prince William Sound and Kodiak segments can also be modeled as time-dependent using the Brownian Passage Time (BPT) model and equivalent Poisson recurrence intervals can be calculated (Section 4.1.4).

The Semidi segment is located between the Kodiak segment and the Shumagin gap (Figure 17). The Semidi segment, according to geodetic analyses, is nearly fully coupled (70 to 90%) whereas in the adjacent Shumagin gap, the plates are largely decoupled (Fletcher *et al*., 2001; Fournier and Freymueller, 2007; Freymueller and Beavan, 1999). An **M** 8.2 earthquake occurred on the Semidi segment in 1928. Johnson and Satake (1994) used modeling of waveforms from the earthquake to infer that the rupture plane dipped about 10 degrees and extended to a depth of about 30 km. More recently, modeling of GPS velocities suggests an effective slip rate for the Semidi segment of about 45 mm/yr, dip of about 6 to 10 degrees and a locking depth of about 23 to 30 km (Fletcher, 2002; Fournier and Freymueller, 2007). We include a characteristic event on

this segment with a weight of 0.6 for **M** 8.2, based on the 1938 earthquake magnitude, and weights of 0.2 for earthquakes of **M** 7.9 and 8.5 (Table 5). We adopt the 180- to 270-year recurrence interval from Witter *et al*. (2022) (Table 5).

For the megathrust, we weighted the characteristic and maximum magnitude recurrence models 0.6 and 0.4, respectively. For megathrust earthquakes larger than **M** 8.0, the USGS (Wesson *et al.*, 2007) weighted equally the characteristic model and the maximum magnitude model for the Prince William Sound and Kodiak segments.

Wadati-Benioff Zone

In the PSHA, we model the Wadati-Benioff zones as a series of 12 staircasing blocks extending to a depth of 120 km that mimic the curvature of the slab using the Slab2 model of Hayes *et al*. (2018). Figure 18 is a cross-section oriented northwest to southeast showing slab seismicity in the vicinity of the Port. The rupture distance from the Port to the slab is 25 km. Focal mechanisms and inversion of first motion data in this area indicate that the subducted Pacific plate is experiencing east-west compression resulting from its collision with the southwestern edge of the subducted Yakutat block (Veilleux and Doser, 2007). The inset map on Figure 19 shows contours of the depth to the top of the slab that were used in the intraslab and megathrust models in the hazard analysis. Zweck *et al*. (2002) use GPS data to model the locked and slipping parts of the plate interface. They conclude that the present extent of the locked plate boundary closely resembles the area of the interface that broke in the 1964 earthquake. The area to the northwest of this locked patch is experiencing post-seismic creep parallel to the direction of plate motion. The boundary between these locked and creeping patches trends to the northwest and is very near Anchorage. This is also the location where the subducting slab begins to bend and dip more steeply (Figure 19).

Similar to our evaluation of crustal background seismicity, recurrence was calculated for the intraslab zone using ABSMOOTH, which resulted in eight realizations of recurrence parameters. A maximum magnitude distribution of **M** 7.5 ± 0.25 was adopted based on the historical record of earthquakes greater than 30 km in depth in the Alaskan subduction zone. Table 3 provides the total rates of events for **M** 5 and above. Note the rates provided in Table 3 are for the entire intraslab zone, and the 12 staircasing blocks modeled in the PSHA each have total rates that are a fraction of the entire zone (such that the summation of the total rates for the 12 blocks equals the rates provided in Table 3). Therefore, each of the 12 blocks has the same range of *b*-values but has a different range of rates of events for **M** 5 and above. The range of *b*-values for the intraslab zone is 0.80 to 0.87, with corresponding total rates of 3.09326 to 2.60756. Figure 20 shows example recurrence curves for the range of *b*-values for **M** ≥ 5 for the weighted mean Mmax (**M** 7.5) for the zone compared to the independent historical seismicity (also accounting for completeness). Recurrence calculations were performed using historical earthquake data for **M** 4.0 and greater. Recurrence curves that incorporate the 3.5 ≤ **M** < 4.0 historical data tend to result in higher *b*-values and curves that appear to underestimate the rate of **M** 5.0 and greater (curves not shown; note that the slab portion of the catalog is complete down to **M** 3.5). To avoid this

possible underestimation, recurrence calculations for the slab YB zone were performed using only data for **M** 4.0 and greater, with the resulting curves shown on Figure 20.

Figure 21 shows the gridded seismicity results generated from ABSMOOTH for the intraslab zone overlain by the outlines of the 12 blocks used in the PSHA. Unlike the crustal background source zones, only a gridded seismicity model was adopted for the intraslab. In general, gridded rates are high throughout the intraslab zone, but for all realizations shown on Figure 21, the cells closest to the Port site have gridded rates higher than the average rate for the zone.

Table 4 lists the recurrence intervals for **M** 5 or greater and **M** 6 or greater events for the intraslab zone. The estimated recurrence interval for events of **M** 5 or greater ranges from approximately 0.3 to 0.4 years (i.e., multiple events of **M** 5 or greater are expected to occur within the intraslab zone each year); for events of **M** 6 or greater, the recurrence interval ranges from approximately 2 to 3 years. In contrast to the crustal source zones, there are many historic earthquakes in the catalog in the intraslab zone (over 1,000 events of **M** 4.0 or greater) which results in smaller epistemic uncertainty in the recurrence parameters and hence the relatively small ranges in the recurrence intervals estimated across the eight realizations for the zone.

4.1.4 Time-Dependent Model

We have modeled the Kodiak + PWS/WY, PWS/WY, and Kodiak segments in a time-dependent manner. Time-dependent hazard for the megathrust was also calculated in Wong *et al*. (2014a) and included a range of COVs of 0.3, 0.5 and 0.7. This range of COV is a typical range and has been used in other time-dependent forecasts (Ellsworth *et al*., 1999). Boyd *et al*. (2008) who performed a partially time-dependent PSHA for Alaska used a single value of 0.5. Given the short time since the 1964 event, the BPT model predicts very low rupture probabilities for all values of COV. Hence, equivalent Poisson rates, based on a time interval of 50 years, are very long. The time-dependent model was weighted 0.9 and the time-independent model was weighted 0.1 in the PSHA based on the analyses of recurrence intervals from Shennan *et al*. (2014) (Section 4.1.3). For the National Seismic Hazard Maps, the USGS has always assumed a time-independent model which is the standard of practice although time-dependent PSHAs are becoming more common (Wong and Thomas, 2020). The USGS has implemented time-dependent models in the Pacific Northwest and Alaska but not part of the NSHMs (Petersen *et al*., 2002; Boyd *et al*., 2008). They are currently evaluating time-dependent models as part of their research model (Mark Petersen, USGS, personal communication, 2022).

In contrast to the Poisson model, a time-dependent renewal process model embodies the expectation that after one earthquake on a fault segment, another earthquake on that segment is unlikely until sufficient time has elapsed for stress to gradually re-accumulate. Such models require a minimum of two parameters and typically include knowledge of the time of the most recent rupture. One parameter is the mean recurrence interval, $\mu = \lambda$, and the other parameter describes the variability of recurrence intervals and can be related to the variance, σ^2, of the

distribution. For the Poisson distribution, σ = μ. We define this variability of recurrence times as the aperiodicity or COV, α=σ/μ.

The BPT model (Matthews *et al*., 2002) is a renewal model that describes the statistical distribution of rupture times. The BPT distribution is also known as the inverse Gaussian distribution. The probability density is defined by

$$f_{BPT}(t) = \sqrt{\frac{\mu}{2\pi a^2 t^3}} exp\left\{-\frac{(t-\mu)^2}{2\mu t a^2}\right\} \quad (8)$$

The hazard function (instantaneous failure rate), $h_{BPT}(t)$, is always zero at t = 0. It increases to achieve a maximum value at a time greater than the mode of $f_{BPT}(t)$, and from there decreases toward an asymptotic value of $h_{BPT}(t) = 1/(2\mu\alpha^2)$. Thus, a BPT process always attains a finite quasi-stationary state in which the failure rate is independent of elapsed time. For an aperiodicity of 0.5, this quasi-stationary state is reached by 1.5 times the mean recurrence rate. After that point, conditional probabilities will not continue to increase. When the aperiodicity $\alpha = 1/\sqrt{2}$, the asymptotic failure rate is 1/μ, which equals the asymptotic failure rate for a Poisson process with the same μ. In practice, the behavior of a BPT model is similar to that of a delayed Poisson process, for which the failure rate is zero up to a finite time following an event and then steps up to an approximately constant failure rate at all succeeding times.

The behavior of a BPT model depends strongly on the value of α. For smaller values of α, $f_{BPT}(t)$ is more strongly peaked and remains close to zero longer. For larger values, the "delay" of "dead time" becomes shorter, $f_{BPT}(t)$ becomes increasingly Poisson-like, and its mode decreases. The hazard function in the quasi-stationary state increases with decreasing values of α and becomes Poisson-like with increasing values.

Equivalent Poisson rupture rates can be back-calculated from the BPT rupture probabilities by solving for an equivalent Poisson rupture rate which produces the same rupture probability using the Poisson model. Equivalent Poisson rates are used in the standard PSHA methodology to compute time-dependent hazard.

Table 6 lists the equivalent Poisson rates calculated in this study. A COV range of 0.3, 0.5, and 0.7 was adopted as described in Section 4.1.3 with weights of 0.5, 0.4, and 0.1, respectively. The heavier weights on the COVs of 0.3 and 0.5 were influenced by the calculated value from the Shennan *et al*. (2014) data of 0.27 (Section 4.1.3). As can be seen in Table 6, the equivalent Poisson recurrence intervals are very long. An exposure period of 50 years was assumed.

4.2 Ground Motion Models

To estimate the horizontal ground motions in the PSHA and DSHA, we have used GMMs appropriate for tectonically active crustal regions such as the western U.S. and for subduction zones. For vertical ground motions, we have used the vertical to horizontal ratios of Abrahamson and Gulerce (2011) to convert from horizontal to vertical spectra. The crustal GMMs, developed

as part of the NGA-West2 Project sponsored by PEER Center Lifelines Program, were published in the journal of *Earthquake Spectra*. These models are the standard of practice for site-specific hazard analyses in the western U.S. and are used in the USGS National Seismic Hazard Maps (NSHMs) (e.g., Petersen *et al*., 2014). The four NGA-West2 models used in this study are Abrahamson *et al*. (2014), Boore *et al*. (2014), Campbell and Bozorgnia (2014), and Chiou and Youngs (2014) (Figure 6).

The Port is located within the Anchorage Basin which contains up to a few kilometers of sedimentary deposits (Dutta *et al.*, 2009). Moschetti *et al*. (2021) computed ground motion residuals from 44 intermediate depth earthquakes including the 2018 Anchorage event to evaluate regional amplification. They identified spatially coherent regional site amplification at all periods including significant basin amplification that scales with basin depth and exhibits maximum amplification of about a factor of two at 1 sec.

A V_S30 of 760 m/sec was used in the GMMs to obtain site-specific ground motions. Other input parameters in the GMMs include $Z_{1.0}$ (the depth of a V_S of 1.0 km/sec) and $Z_{2.5}$ (the depth to a V_S of 2.5 km/sec). $Z_{1.0}$ is used by Chiou and Youngs (2014), Boore *et al*. (2014), and Abrahamson *et al*. (2014) and $Z_{2.5}$ is only used in one model, Campbell and Bozorgnia (2014). Based on Shellenbaum *et al*. (2010), the depth to basement rock beneath the Port is about 1.0 km. Hence that value was adopted for $Z_{2.5}$. A $Z_{1.0}$ of 0.5 km was assumed. Other parameters such as depth to the top of rupture (zero for all faults that intersect the surface unless specified otherwise), dip angle, rupture width, and aspect ratio were specified for each fault or calculated within the PSHA code.

For the Alaska subduction zone, we used the NGA-Sub GMMs. NGA-Sub was a large multidisciplinary and multi-researcher initiative to develop a comprehensive ground-motion database and multiple GMMs for subduction earthquakes. This project was also organized by the PEER and encompasses subduction zones around the world. In the NGA-Sub Project, a database of ground-motions recorded in worldwide subduction events (Bozorgnia and Stewart, 2020) was developed. This database includes the processed recordings and supporting source, path, and site metadata from Japan, Taiwan, the U.S. Pacific Northwest, Alaska, Mexico and Central America, South America, and New Zealand. The NGA-Sub database includes 1,570 events with magnitudes ranging from **M** 4.0 to 9.1. The subduction events are classified as megathrust or intraslab events. The NGA-Sub ground-motion database has over 210,000 individual ground-motion components. Multiple GMMs have been developed by NGA-Sub developer teams using this empirical ground-motion database and supporting ground-motion simulations. This report uses the currently developed NGA-Sub GMMs from three developer teams:

- Kuehn *et al*. (2020) [KBCG20]
- Parker *et al*. (2020) [PSHAB20]
- Abrahamson and Gülerce (2020) [AG20]

All three models provide global and regionalized models for PGA and 5%-damped pseudo-spectral acceleration at 22 oscillator periods ranging from 0.01 to 10 sec. Developed models accommodate the differences in the magnitude, distance, and depth scaling for megathrust and intraslab earthquakes. In this study, we used the global models in consultation with Dr. Norm Abrahamson (written communication, 21 July 2022), developer of AG20, who noted an apparent error in the Alaska strong motion data and the lack of data from events of **M** > 6 at short to moderate distances. We are aware that for the 2023 Alaska National Seismic Hazard Maps, the USGS is planning to only use the Alaska versions of the NGA-Sub GMMs including the adjusted and unadjusted models of AG20. For KBCG20, PSHAB20, and the two AG20 models, the USGS will also implement 15th and 85th percentile as well as the median models for a total of 12 models with the intent of covering the full range of epistemic uncertainty (see following discussion).

The global models do not contain basin amplification factors; only selected regional models such as for the Cascadia region. For the 2023 Alaska maps, the USGS recognizes that basin effects are significant in the Anchorage area, but they have not developed a basin effects model and hence do not plan to account for such effects in the maps. Discussions with Morgan Moschetti (USGS, October 2022) indicated that the Puget Sound was a suitable analogue and so the NGA-Sub global models were revised to include the basin amplification factors for the Puget Sound region that are in the Cascadia models. All three models parameterize basin amplification using $Z_{2.5}$. The Cascadia basin factors in the three NGA-Sub GMMs are for periods of about 0.2 to 10 sec and vary in amplitude depending on the model and model inputs. The AG20 basin factors can be as large as a factor of two at 10 sec.

Site response terms include both linear and nonlinear site effects. No differences in site effects between the event types were included in the models. KBCG20 and AG20 use the depth to the top of rupture (Z_{tor}) for depth scaling. PSHAB20 uses the hypocentral depth (Z_{hyp}) for depth scaling.

The aleatory uncertainty is based on the between-event and within-event uncertainty. Similar to the development of the median GMM, each modeler team investigated, evaluated, and developed an aleatory uncertainty model based on the between-event and within-event variations. For the KBCG20 model, these variations are independent of prediction parameters such as distance, magnitude, or site conditions. For the PSHAB20 model, the within-event model is defined as a function of distance and V_S30 site conditions; however, the between-event variation is independent of these variables. For the AG20 model, the between-event standard deviation piece of the aleatory variability model is region and distance independent whereas the within-event standard deviations are both region and distance dependent. Note that a single-station model is also developed for the PSHAB20 model but is not currently developed for the other two NGA-Sub models.

As noted by Al Atik and Youngs (2014), the development of the NGA-West2 models was a collaborative effort with many interactions and exchanges of ideas among the developers and the developers indicated that an additional epistemic uncertainty needs to be incorporated into the

median ground motions in order to more fully represent an appropriate level of epistemic uncertainty. Hence, for each of the NGA-West2 GMMs used for the crustal events, an additional epistemic uncertainty on the median ground motion was included. The three-point distribution and model of Al Atik and Youngs (2014) was applied. The model is a function of magnitude, style of faulting, and spectral period.

For the NGA-Sub GMMs, there was no evaluation of the model-to-model variability and associated statistical uncertainty in median predictions. However, the three NGA-Sub models provide the epistemic uncertainty in the median ground motion predictions. For this project, this epistemic uncertainty is used as the additional epistemic uncertainty for the NGA-Sub models for a total of nine models. Following the Al Atik and Youngs (2014) epistemic uncertainty model for the NGA-West2 GMMs, a three-point distribution and model of was applied which weights the median GMMs 0.6 and ± additional epistemic uncertainty of $1.645*\sigma_{ln}$ weighted 0.2 each. The three NGA-Sub models used in this report (i.e., KBCG20, PSHAB20, and AG20) are weighted equally for seismic hazard calculations.

5.0 SEISMIC HAZARD RESULTS

The ground motion hazard results for the Port and a V_S30 of 760 m/sec are described below. Note the hazard is time-dependent for the megathrust beneath Anchorage and has been adjusted for basin effects. The latter is a notable change from previous analyses of the Port (Wong et al., 2008; 2014).

5.1 PSHA RESULTS

The results of the PSHA are presented in terms of ground motion as a function of annual exceedance probability. The annual exceedance probability is the reciprocal of the average return period. Figure 22 shows the mean, median (50th percentile), 5th, 15th, 85th, and 95th percentile hazard curves for PGA. These fractiles indicate the range of epistemic uncertainties about the mean hazard. At the 72- and 2,475-year return periods, the range of uncertainty is about a factor of 3.5 and 4.0, respectively, between the 5th and 95th percentile fractiles (Table 7). The 1.0 sec horizontal spectral acceleration (SA) hazard is shown on Figure 23. The range of uncertainty between the 5th and 95th percentile fractiles is slightly smaller at 1.0 sec SA compared to PGA, with a factor of about 2.5 and 3.0 at the 72- and 2,475-year return periods, respectively. At the return periods of 72, 475, 975, and 2,475 years, the mean PGA and 1.0 sec SA values and their uncertainties are listed in Table 7.

The contributions of the various seismic sources to the mean PGA and 1.0 sec SA hazard are shown on Figures 24 to 27. At all return periods, the intraslab controls both the PGA (Figures 24 and 25) and 1.0 sec SA hazard (Figures 26 and 27).

Figures 28 and 29 illustrate deaggregation of the mean PGA and 1.0 sec SA hazard by magnitude, distance, and epsilon bins for the 72-, 475-, 975-, and 2,475-year return periods. Epsilon is the difference between the logarithm of the ground motion amplitude and the mean logarithm of ground motion (for that magnitude and distance) measured in units of the standard deviation of the logarithm of the ground motion. Thus, positive epsilons indicate larger than average ground motions. By deaggregating the PGA and 1.0 sec SA hazard by magnitude, distance, and epsilon bins, the contributions by events at different periods are illustrated. On each of the deaggregation figures, the plot in the upper left (panel A) shows the contribution from all seismic sources modeled. The other two plots in the figures show the contribution by events from the following source groups: megathrust (interface) (panel B), and instraslab (panel C). The contributions (shown as the vertical axis labeled “Proportion” in panels B and C in the figures) are normalized by total hazard, such that the sum of the contributions shown in the megathrust and intraslab panels (plus the faults and background) at a given return period and spectral period equals one.

At PGA, the hazard is controlled by events in the range of **M** 5.5 to 7.5 at distances between 25 and 150 km, primarily corresponding to the intraslab (Figure 28). Contribution from the intraslab ranges from 93% at the 72-year return period to 96% at the 2,475-year return period. Contribution from the megathrust ranges from 1% at the 72-year return period up to 3% at the 2,475-year return period. At 1.0 sec SA, the results are similar, though the relative contribution of events in

the range of **M** 9.0 to 9.5 at distances between 25 and 100 km is slightly higher than at PGA (Figure 29). Based on the magnitude and distance bins (Figures 28 and 29), the controlling earthquakes as defined by the mean magnitude (M-bar) and modal magnitude (M*) and mean distance (D-bar) and modal distance (D*) can be calculated. Table 8 lists the M-bar, M*, D-bar, and D* for the four return periods (72, 475, 975. and 2,475 years) and for a range of return periods (PGA, 0.2, 1.0, 1.5, and 2.0 sec SA).

We assigned different sets of GMMs to sources based on source type (Figure 6). Hence, the impact of a single GMM on the total mean hazard depends on the relative contribution of the sources that have been assigned to that GMM. As a result, it is useful to examine the relative differences in combined hazard due to sources using the same set of GMMs due to individual GMMs in the set. Figures 30 and 31 show the sensitivity of crustal PGA and 1.0 sec SA hazard, respectively, to the NGA-West2 GMMs with the additional epistemic uncertainty from Al Atik and Youngs (2014). At PGA, there is a factor of about 1.5 between the largest and smallest ground motions predicted by the NGA-West2 GMMs at both the 72- and 2,475-year return periods (Figure 30). At 1.0 sec SA, there is a factor of about 2.0 between the largest and smallest ground motions predicted by the NGA-West2 GMMs at both the 72- and 2,475-year return periods (Figure 31). Figures 32 and 33 show the sensitivity of megathrust PGA and 1.0 sec SA hazard, respectively, to the NGA-Sub GMMs with additional epistemic uncertainty included. The range between the largest and smallest ground motions predicted for the megathrust is much larger than for the crustal sources, with a factor of 4.7 and 4.8 at PGA and 1.0 sec SA, respectively, at the 2,475-year return period (note that the NGA-Sub GMMs are not defined at the 72-year return period). This larger range of predicted ground motions is primarily due to the additional epistemic uncertainty added to the models, rather than difference between the median NGA-Sub GMMs. This relationship is also observed in the sensitivity of intraslab PGA and 1.0 sec SA hazard, where the range between the largest and smallest ground motions is large (4.9 and 3.9, respectively, at the 2,475-year return period), but the range between the predicted ground motions from the median NGA-Sub GMMs is relatively small (Figures 34 and 35).

The 5%-damped mean UHS for return periods of 72, 475, 975, and 2,475 years are shown in Figure 36 and listed in Table 9. These UHS reflect the geometric mean of expected horizontal ground motions, as predicted by the GMMs. The PGA values at these four return periods are 0.20, 0.56, 0.79, and 1.19 g, respectively.

5.2 Comparison with National Seismic Hazard Maps

In the 2007 version of the U.S. Geological Survey's Alaska Seismic Hazard Maps (time-independent), which are the basis for the Alaskan portions of the U.S. building code and the International Building Code, Wesson *et al*. (2007) have estimated probabilistic ground motions for Alaska for a range of annual exceedance frequencies. We computed the 72-, 475-, 975-, and 2,475-year return period PGA and 1.0 sec SA values based on the hazard curves of the 2007 USGS Alaska Seismic Hazard Maps for a V_S30 of 760 m/sec. At PGA, the differences range from the site-specific value 5% lower than the 2007 USGS value at the 72-year return period, to the

site-specific value 72% higher than the 2007 USGS value at the 2,475-year return period (Table 10). At 1.0 sec SA, the differences range from the site-specific value 22% lower than the 2007 USGS value at the 72-year return period, to the site-specific value 9% higher than the 2007 USGS value at the 2,475-year return period (Table 10). Differences between our site-specific hazard and the 2007 USGS hazard are likely due to (1) the use of the NGA-Sub GMMs in this study, which had not yet been developed for use in the USGS 2007 model; (2) the inclusion of time dependency for the megathrust in this study; and (3) the inclusion of basin effects in this study.

5.3 DSHA Results

Deterministic ground motions were computed for scenarios on seismic sources expected to be capable of producing the largest ground motions at the site due to their magnitude and distance. The most significant deterministic seismic sources to the Port are the intraslab and megathrust. For the intraslab, the maximum event modeled was a **M** 7.6 at a rupture distance of 25 km, and for the megathrust, the maximum event modeled was a **M** 9.2 at a rupture distance of 31 km (Tables 5 and 11).

The 5%-damped 50th (median) and 84th percentile horizontal acceleration response spectra are calculated for the intraslab and megathrust using the same GMMs used in the PSHA. Other input parameters are provided in Table 11. Figures 37 and 38 present the sensitivity of the 84th percentile horizontal acceleration response spectra for the deterministic scenarios to the GMMs. These figures show spectra for each of the individual models (lines shown in color) and the weighted average of these spectra (line shown in black). The range in spectra for the individual models shown in these figures represents the epistemic uncertainty in the ground motion modeling.

Figure 39 shows the weighted mean median and 84th percentile spectra for the intraslab and megathrust as well as the enveloping spectra. The enveloped median and 84th percentile spectra are developed by taking the maximum spectral acceleration between the intraslab and megathrust at each spectral period. For spectral periods up to 4 sec, the intraslab controls hazard, and at longer periods, the megathrust controls hazard. Table 12 lists the individual scenario and controlling spectra.

A comparison of the enveloped 5%-damped median and 84th percentile controlling horizontal acceleration response spectra and the 5%-damped UHS for a suite of return periods is provided on Figure 40. The median deterministic response spectrum is between the 475- and 975-year return period UHS up to 1.5 sec; at longer spectral periods up to 10.0 sec, the median spectrum is between the 975- and 2,475-year return period UHS. At 10.0 sec, the median spectrum exceeds the 2,475-year return period UHS. The 84th percentile spectrum is greater than the 2,475-year return period UHS at all spectral periods.

6.0 DESIGN EARTHQUAKE GROUND MOTIONS

Preliminary design UHS have been developed for the 72, 475, 975, and 2,475-year return period. CMS were developed at 975 years conditioned at 0.2 and 2.0 sec SA for comparison with the UHS and to assess whether time histories should be developed using the UHS or CMS. A comparison of the spectra indicated that there was no added benefit to the Terminal 1 and Terminal 2 developments in using the CMS for the time histories.

6.1 CONDITIONAL MEAN SPECTRA

The UHS represents the spectral accelerations at each period based on the rates of occurrence of all nearby sources, the ground motion models, and the uncertainties in these models. It is generally a broader spectrum than is expected for any single event. As in the case of the controlling earthquake spectra approach, this uniform hazard can be represented by a suite of spectra that individually more closely represent the spectral shape of expected events contributing to the UHS. At a given period, a spectrum can be computed based on the deaggregated magnitude, distance and epsilon at that period. Depending on the epsilon required to match the spectrum to the UHS, the expected shape of this spectrum is not necessarily the median predicted spectral shape, i.e., the controlling earthquake spectrum. Given the epsilon at a target period, epsilon at all other periods can be determined using a correlation function. Thus, a CMS represents a more realistic shape of an event likely to cause the target spectral acceleration at the target period (Baker, 2011).

The CMS approach is described in Baker (2011) and is summarized here. The steps in the process are:

Step 1: Determine the Target S_a at a Given Period, and the Associated M, R and ε

For a specified return period, determine the target S_a from the mean hazard curve for S_a for the fundamental period of the structure to be analyzed. This period is denoted T^*. For this ground motion, obtain the mean magnitude (M), distance (R), and ε from the PSHA deaggregation results. For this project, deaggregation results for the megathrust and intraslab were used. Depending upon the response characteristics of the structure or structures to be analyzed, CMS should be developed for several values of T^*.

Step 2: Compute the Mean and Standard Deviation of the Response Spectrum, Given M and R

For the mean M and R determined in Step 1, compute the mean and standard deviation of logarithmic spectral acceleration at all periods for the mean magnitude and distance. These are provided by standard ground motion prediction models. The predicted mean and standard deviation, given magnitude, distance, period, etc., are denoted $\overline{\ln Sa}(M,R,T)$ and $\sigma_{\ln Sa}(T)$, respectively. The mean and standard deviation of the log spectral acceleration can be computed

using the GMMs that were used in the PSHA itself. Since multiple GMMs were used in the PSHA, a weighted estimate of the mean log S_a and the standard deviation can be used. For this project, CMS for each GMM were computed and combined using deaggregation weights. Deaggregation weights are the fractional contribution of each GMM to the total hazard for a given period and hazard level, as described in Lin *et al*. (2013).

Step 3: Compute ε at Other Periods, Given ε(T*)

Compute the "conditional mean" ε at other periods. The conditional mean ε at ε (T^*) was determined in Step 1. The conditional mean at other periods, T_i, is determined by,

$$\mu_{\varepsilon(Ti)|\varepsilon(T*)} = \rho(T_i, T^*)\varepsilon(T^*) \tag{9}$$

where $\rho(T_i,T^*)$ is the correlation coefficient between ε for periods T_i and T^*. The correlation coefficients of Baker and Jayaram (2008), which are developed using the NGA West database and are applicable in the range 0.01 to 10 sec are used to compute the conditional mean ε at other periods.

Step 4: Compute the Conditional Mean Spectrum

The CMS is computed using the estimated log mean and standard deviation from Step 2 and the conditional mean $\varepsilon(T_i)$ values determined in Step 3. The CMS is estimated according to:

$$\mu_{\ln S_a(T_i)|\ln(S_a(T^*)} = \mu_{\ln S_a}(M, R, T_i) + \rho(T_i, T^*)\varepsilon(T^*)\sigma_{\ln S_a}(T_i) \tag{10}$$

The CMS is,

$$S_{a,CMS}(T) = \exp(\mu_{\ln(S_a(T_i)|\ln(S_a(T^*)}) \tag{11}$$

The standard deviation of $\ln S_a$ (T_i) is

$$\sigma_{\ln Sa(T_i)|\ln Sa(T*)} = \sigma_{\ln Sa(T_i)}\sqrt{1-\rho^2(T_i, T^*)} \tag{12}$$

Conditioning periods of 0.2 and 2.0 sec were selected for the CMS. These periods span the possible range of fundamental periods of the Port.

The horizontal CMS and the UHS for 975-year return period are shown in Figure 41 and listed in Table 13.

7.0 DEVELOPMENT OF TIME HISTORIES

Eleven sets of horizontal and vertical-component time histories were developed for the 72-, 475-975-, and 2,475-year return period UHS (Appendices A to D). The horizontal UHS are shown in Figure 36 and provided in Table 9, and the vertical spectra are shown in Figure 42 and provided in Table 14. Because the response spectrum of a time history has peaks and valleys that deviate from the design response spectrum (target spectrum), it is necessary to modify the motion to improve its response spectrum compatibility. The procedure proposed by Lilhanand and Tseng (1988), as modified by Al Atik and Abrahamson (2010) and contained in their computer code RSPMatch09, was used to develop the acceleration time histories through spectral matching to the target (seed) spectrum. This time-domain procedure has been shown to be superior to previous frequency-domain approaches because the adjustments to the time history are only done at the time at which the spectral response occurs, resulting in only localized perturbations on both the time history and the spectra (Lilhanand and Tseng, 1988).

To match the target spectrum, seed time histories should be selected from events of similar magnitude, distance (for duration), to a lesser extent, site condition, and most importantly, spectral shape as the earthquake dominating the spectrum. The site condition is a secondary criterion that may be used to favor some seeds over others if the main criteria are similar. The main goal of matching is to modify the seed to match its response spectrum to the target. For this purpose, seeds with spectral shapes closer to the target undergo less distortion to match the target. The seed time histories selected and their properties are listed in Appendices A to D.

In addition to criteria for selecting seed time histories based on spectral shape, target Arias intensity and duration of strong ground motion were calculated based on the controlling earthquake and used in the selection process. Arias intensity is a ground motion parameter defined by Arias (1970) as the integral of the square of acceleration over the duration of a time series record, as follows:

$$Ia = \frac{\pi}{2g}\int_0^{\infty} a(t)^2 dt \qquad (13)$$

where I_a is Arias intensity, $a(t)$ is acceleration, and g is the acceleration of gravity. Recent studies show that I_a correlates well with the damage potential of earthquakes (*e.g.*, Travasarou *et al.*, 2003). The models of Watson-Lamprey and Abrahamson (2006) and Abrahamson *et al.* (2016) were used for the I_a calculations. For all return periods, deaggregated magnitudes and distances at 1.0 sec SA for the megathrust and intraslab were used to calculate the target I_a values and ranges. The computed values are contained in the appendices. Note that these relationships provide targets for geometric mean I_a.

Duration of a strong ground motion is related to the time required for release of accumulated strain energy by rupture along the fault and generally increases with magnitude of the earthquake. Trifunac and Brady (1975) defined significant duration as the time interval between the points at which 5% and 95% of the total energy (I_a) has been recorded. The target durations for the 72,

475, 975, and 2,475-year time histories were calculated using the models of Silva *et al*. (1997) and Kempton and Stewart (2006) and were calculated based on deaggregation of the megathrust and intraslab at 1.0 sec SA, similar to the Arias intensity calculations. The computed values are listed in the appendices.

The spectral matches (up to 4 sec) and the resulting acceleration, velocity, and displacement time histories are shown in the appendices. Also shown with the spectral matches are the response spectra calculated from the scaled seed time histories. Acceleration, velocity, and displacement time histories were developed. Husid plots at the bottom of each of these figures illustrate the increase in energy (normalized Arias intensity) with time.

The properties of the matched time histories that include peak acceleration, velocity, and displacement, as well as Arias intensities and 5 to 95% durations are listed in the appendices.

8.0 REFERENCES CITED

Abrahamson, N. and Gulerce, Z., 2011, Site-specific design spectra for vertical ground motion: Earthquake Spectra, v. 27, p. 1023-1047.

Abrahamson, N. and Gülerce Z., 2020, Regionalized ground-motion models for subduction earthquakes based on the NGA-SUB Database: PEER Report No. 2020/25, Pacific Earthquake Engineering Research Center, University of California, Berkeley, CA.

Abrahamson, N.A. and Silva, W.J., and Kamai, R., 2014, Summary of the ASK14 ground-motion relation for active crustal regions: Earthquake Spectra, v. 30, p. 1025-1055.

Abrahamson, C., Hao-Jun, M.S. and Yang, B., 2016, Ground-motion prediction equations for Arias intensity consistent with the NGA-West2 ground-motion Models: PEER Report No. 2016/05, Pacific Earthquake Engineering Research Center, University of California, Berkeley, 42 p.

Aki, K., 1983, Seismological evidence in support of the existence of “Characteristic Earthquakes”: Earthquake Notes, v. 54, p. 60 61.

Al Atik, L. and Abrahamson, N., 2010, An improved method for nonstationary spectral matching: Earthquake Spectra: v. 26, p. 601-617.

Al Atik, L. and Youngs, R., 2014, Epistemic uncertainty for NGA-West2 models: Earthquake Spectra, v. 30, p. 1301-1318.

Alaska Earthquake Center (AEC), 2022, https://earthquake.alaska.edu/alaskas-seismic-network-history.

Anderson, J.G., 1979, Estimating the seismicity from geological structure for seismic risk studies: Bulletin of the Seismological Society of America, v. 69, p. 135-158.

Arias, A., 1970, A measure of earthquake intensity: Seismic Design for Nuclear Power Plants, R.J. Hansen, ed., MIT Press, Cambridge, Massachusetts, p.438–483.

Baker, J.W., 2011, The conditional mean spectrum: A tool for ground motion selection,” American Society of Civil Engineers, Journal of Structural Engineering, v. 137, p. 322-331.

Baker, J. W., and Jayaram, N., 2008, Correlation of spectral acceleration values from NGA ground motion models: Earthquake Spectra, v. 24, p. 299-317.

Bartsch-Winkler, S.B. and Schmoll, H.R., 1992, Utility of radiocarbon-dated stratigraphy in determining late Holocene earthquake recurrence intervals, upper Cook Inlet region, Alaska: Geological Society of America Bulletin, v. 104, p. 684-694.

Bemis, S.P., Weldon, R.J., and Carver, G.A., 2015, Slip partitioning along a continuously curved fault: Quaternary geologic controls on Denali fault system slip partitioning, growth of the Alaska Range, and the tectonics of south-central Alaska: Geological Society of America, Lithosphere, v.7, p.235-246

Bender, A. M., Haeussler, P. J. and Powers, P. M., 2021a, Geologic inputs for the 2023 Alaska update to the U.S. National Seismic Hazard Model (NSHM): U.S. Geological Survey data release.

Bender, A. M. and Haeussler, P. J., 2021b, Alaska fault trace mapping, 2021: U.S. Geological Survey data release.

Betka, P.M., Gillis, R.J., and Benowitz, J.A., 2017, Cenozoic sinistral transpression and polyphase slip within the Bruin Bay fault system, Iniskin-Tuxedni region, Cook Inlet, Alaska: Geosphere, v. 13, p. 1806–1833.

Bodle, R. R., 1945, United States Earthquakes 1943, Coast and Geodetic Survey: US Government Printing Office, no. 762, 49 p.

Boore, D.M., Stewart, J.P., Seyhan, E., Atkinson, G.M., 2014, NGA-West2 equations for predicting PGA, PGV, and 5%-damped PSA for shallow crustal earthquakes: Earthquake Spectra, v. 32, p. 979-1004.

Boyd, O.S., Zeng, Y., Bufe, C.G., Wesson, R.L., Pollitz, F., and Hardebeck, J.L., 2008, Toward a time-dependent probabilistic seismic hazard analysis for Alaska: Active Tectonics and Seismic Potential of Alaska Geophysical Monograph Series 179.

Bozorgnia, Y., and Stewart, J., 2020, Data resources for NGA-Subduction Project: Pacific Earthquake Engineering Research Center, University of California, Berkeley, PEER Report 2020/02, 179 p.

Brocher, T.M., Fuis, G.F., Fisher, M.A., Plafker, G., Moses, M.J., Taber, J.J., and Christensen, N.I., 1994, Mapping of the megathrust beneath the northern Gulf of Alaska using wide-angle seismic data: Journal of Geophysical Research, v. 99, p. 11,663-11,685.

Brums, T.R., 1983, Model for the origin of the Yakutat black, an accreting terrane in the northern Gulf of Alaska: Geology, v. 11, p. 718-721.

Campbell, K.W. and Bozorgnia, Y., 2014, NGA-West2 ground motion model for the average horizontal components of PGA, PGV, and 5%-damped linear acceleration response spectra: Earthquake Spectra, v. 30, p. 1087-1115.

Carver, G., and Plafker, G., 2008, Paleoseismicity and neotectonics of the Aleutian subduction zone – an overview. In: Freymueller, J.T., Haeussler, P.J., Wesson, R., Ekstrom, G., (Eds.), Active Tectonics and Seismic Potential of Alaska. In: Geophysical Monograph Series, v. 179. American Geophysical Union, Washington, 350 p.

Carver, G.A., Lettis, W.R., and Witter, R.C., 2003, Seismic hazard evaluation, Kodiak LORAN Station, Phase I, II and III: unpublished consulting reports prepared for the U.S. Coast Guard, Civil Engineering Unit, Juneau, Alaska.

Carver, G.A., Plafker, G., Metz, M., Cluff, L., Slemmons, B., Johnson, E., Roddick, J., and Sorenson, S., 2004, Surface rupture on the Denali fault interpreted from tree damage during the 1912 Delta River Mw 7.2-7.4 earthquake: Implications for the 2002 Denali Fault Earthquake Slip Distribution: Bulletin of the Seismological Society of America, v. 94; p. S58-S71.

Chiou, B-S.J. and Youngs, R.R., 2014, Update of the Chiou and Youngs NGA ground motion model for average horizontal component of peak ground motion and response spectra: Earthquake Spectra, v. 30, p. 1117-1153.

Christensen, G.L., Gulick, S.P.S., van Avendonk, H.J.A., Worthington, L.L., Reece, R.S., Pavlis, T.L., 2010, The Yakutat terrane: dramatic change in crustal thickness across the Transition fault, Alaska: Geology, v. 38, p. 895-898.

Christensen, D.H. and Beck, S.L., 1994, The rupture process and tectonic implications of the great 1964 Prince William Sound earthquake: Pure and Applied Geophysics, v. 142, p. 29-53.

Combellick, R.A., 1994, Investigation of peat stratigraphy in tidal marshes along Cook Inlet, Alaska, to determine the frequency of 1964-style great earthquakes in the Anchorage region: Alaska Division of Geological and Geophysical Surveys Report of Investigation 94-7, 24 p.

Cornell, C.A., 1968, Engineering seismic risk analysis: Bulletin of the Seismological Society of America, v. 58, p. 1583-1606.

Davies, J.N., and House, L., 1979, Aleutian subduction zone seismicity, volcano-trench separation, and their relation to great thrust earthquakes: Journal of Geophysical Research, v. 84, p. 4583-4591.

Demets, C., and Dixon, T.H., 1999, New kinematic models for Pacific-North America motions from 3 Ma to present, 1: Evidence for steady motion and biases in the NUVEL-1A model: Geophysical Research Letters, v. 26, p. 1921-1924.

Detterman, R. L., Plafker, G., Russell, G.T., and Hudson, T., 1976, Features along part of the Talkeetna segment of the Castle Mountain-Caribou fault system, Alaska: U.S. Geologic Survey MF Map 738, 1 sheet.

Dutta, U., Sen, M.K., Biswas, N., and Yang, Z., 2009, Investigation of shallow sedimentary structure of the Anchorage Basin, Alaska, using simulated annealing inversion of site response: Bulletin of the Seismological Society of America, v. 99, p. 326-339.

Eberhart-Phillips, D., Haeussler, P.J., Freymueller, J.T., Frankel, A.D., Rubin, C.M., Craw, P., Ratchkovski, N.A., Anderson, G., Carver, G.A., Crone, A.J., Dawson, T.E., Fletcher, H., Hansen, R., Harp, E.L., Harris, R.A., Hill, D.P., Hreinsdottir, S., Jibson, R.W., Jones, L.M., Kayen, R.E., Keefer, D.K., Larsen, C.F., Moran, S.C., Personius, S.F., Plafker, G., Sherrod, B.L., Sieh, K., Sitar, N., and Wallace, W.K., 2003, The 2002 Denali fault earthquake, Alaska – A large magnitude, slip-partitioned event: Science, v. 300, p. 1113-1118.

Elliott, J., 2011, Active tectonics in southern Alaska and the role of the Yakutat Block constrained by GPS measurements: Ph.D. dissertation, 187 p., University of Alaska Fairbanks, Fairbanks.

Ellsworth, W.L., Matthews, M.V., Nadeau, R.M., Nishenko, S.P., Reasenberg, P.A., and Simpson, R.W., 1999, A physically-based earthquake recurrence model for estimation of long-term earthquake probabilities: Workshop on Earthquake Recurrence: State of the Art and Directions for the Future, Instituto Nazionale de Geofisica, Rome, Italy, 22-25 February.

EPRI/DOE/NRC, 2012, Electric Power Research Institute (EPRI), 2013, Seismic evaluation guidance: Screening, Prioritization, and Implementation Details (SPID) for the resolution of Fukishima near-term task for recommendation 2.1: Seismic.

Fletcher, H.J., 2002, Crustal deformation in Alaska measured using the Global Positioning System, University of Alaska, Thesis, 135p.

Fletcher, H.J., Beavan, J., Freymueller, J., and Gilbert, L., 2001, High interseismic coupling of the Alaska subduction zone SW of Kodiak Island inferred from GPS data: Geophysical Research Letters, v. 28, p. 443-446.

Flores, C. and Doser, D.I., 2005, Shallow seismicity of the Anchorage, Alaska region (1964– 1999): Bulletin of the Seismological Society of America, v. 95, p. 1865–1879.

Fournier, T.J., and Freymueller, J.T., 2007, Transition from locked to creeping subduction in the Shumagin region, Alaska: Geophysical Research Letters, v. 34, p. L06303.

Freymueller, J.T., and Beavan, J., 1999, Absence of strain accumulation in the western Shumagin segment of the Alaska subduction zone: Geophysical Research Letters, v. 26, p. 3233-3236.

Freymueller, J.T., Woodard, H., Cohen, S.C., Cross, R., Elliot, J., Larsen, C.F., Hreinsdóttir, S., and Zweck, C., 2008, Active deformation processes in Alaska, based on 15 Years of GPS measurements, in Active Tectonics and Seismic Potential of Alaska, p.1-42

Gardner, J.K., and Knopoff, L., 1974, Is the sequence of earthquakes in southern California, with aftershocks removed, Poissonian?: Bulletin of the Seismological Society of America, v. 64, p.1363-1367.

GeoPentech, 2015, Southwestern United States Ground Motion Characterization SSHAC Level 3 – Technical Report Rev. 2, March 2015.

Grant, A.R.R., Jibson, R.W., Witter, R.C., Allstadt, K.E., Thompson, E.M., and Bender, A.M., 2020, Ground failure triggered by shaking during the November 30, 2018, magnitude 7.1 Anchorage, Alaska, earthquake: U.S. Geological Survey Open-File Report 2020–1043, 21 p.

Haeussler, P.J., Armstrong, P.A., Liberty, L.M., Ferguson, K.M., Finn, S.P., Arkle, J.C. and Pratt, T.L., 2015, Focused exhumation along megathrust splay faults in Prince William Sound, Alaska: Quaternary Science.

Haeussler, P.J., Matmon, A., Schwartz, D.P., and Seitz, G.G., 2017a, Neotectonics of interior Alaska and the late Quaternary slip rate along the Denali fault system: Geosphere, v. 13, p. 1445–1463.

Haeussler, P.J., Saltus, R.W., Stanley, R.G., Ruppert, N., Lewis, K., Karl, S.M., and Bender, A., 2017b, The Peters Hills basin, a Neogene wedge-top basin on the Broad Pass thrust fault, south-central Alaska: Geosphere, v. 13.

Haeussler, P.J., Wells, R.E., Blakely, R.J., Murphy, J. and Wooden, J.L., 2000, Structure and timing of movement on the Seattle fault at Green and Gold Mountains, Kitsap Peninsula, Washington: Geological Society of America Abstracts with Programs, v. 32, p. A-16.

Haeussler, P.J., Best, T.C., and Waythomas, C.F., 2002, Paleoseismology at high latitudes: Seismic disturbance of late Quaternary deposits along the Castle Mountain fault near Houston, Alaska: Geological Society of America Bulletin, v. 114, p. 1296-1310, 1 pl.

Haeussler, P. J., and Saltus, R.W., 2004, 26 km of offset on the Lake Clark fault since Late Eocene time: U.S. Geological Survey Professional Paper 1709-A, 4 p.

Haeussler, P. J., and Saltus, R.W., 2011, Location and extent of Tertiary structures in Cook Inlet Basin, Alaska, and mantle dynamics that focus deformation and subsidence: U.S. Geological Survey Professional Paper 1776-D, 34 p.

Hake, C.A., and Cloud, W.K., 1966, United States Earthquakes 1964, Coast and Geodetic Survey: U.S. Government Printing Office, 91 p.

Hale, C., Abrahamson, N. and Bozorgnia, Y., 2018, Probabilistic seismic hazard analysis code verification: Pacific Earthquake Engineering Research Center, College of Engineering, University of California, Berkeley, PEER Report 2018/03, 105 p.

Hamilton, S., and Shennan, I., 2005, Late Holocene relative sea-level changes and the earthquake deformation cycle around upper Cook Inlet, Alaska: Quaternary Science Reviews, v. 24, p. 1479.

Hamilton, S., Shennan, I., Combellick, R., Mulholland, J., and Noble, C., 2005, Evidence for two great earthquakes at Anchorage, Alaska and implications for multiple great earthquakes through the Holocene: Quaternary Science Reviews, v. 24, p. 2050.

Hanks, T.C. and Kanamori, H. 1979, A moment magnitude scale: Journal of Geophysical Research, v. 84, p. 2348-2350.

Hayes, G., 2018, Slab2 - A Comprehensive Subduction Zone Geometry Model: U.S. Geological Survey data release.

Hutchinson, I., and Crowell, A.L., 2007, Recurrence and extent of great earthquakes in southern Alaska during the late Holocene from an analysis of the radiocarbon record of land-level change and village abandonment: Radiocarbon, v. 49, p. 1-63.

Ichinose, G., Somerville, P., Thio, H.K., Graves, R., and O'Connell, D., 2007, Rupture process of the 1964 Prince William Sound, Alaska, earthquake from the combined inversion of seismic, tsunami, and geodetic data: Journal of Geophysical Research, v. 112, p. B07306.

Johnson, J.M., and Satake, K., 1994, Rupture extent of the 1938 Alaska earthquake as inferred from tsunami waveforms: Geophysical Research Letters, v. 21, p. 733-736.

Johnson, J.M., Satake, K., Holdahl, S.R., and Sauber, J., 1996, the 1964 Prince William Sound earthquake: Joint inversion of tsunami and geodetic data: Journal of Geophysical Research, v. 101, p. 523-532.

Kanamori, H., 1977, The energy release in great earthquakes: Journal of Geophysical Research, v. 82, p. 2981-2988.

Keefer, D.I. and Bodily, S.E., 1983, Three-point approximations for continuous random variables: Management Science, v. 26, p. 595-609.

Kempton, J.J. and Stewart, J.P., 2006, Prediction equations for significant duration of earthquake ground motions considering site and near-source effects: Earthquake Spectra, v. 22, p. 985–1013.

Koehler, R.D. and Reger, R.D, 2011, Reconnaissance evaluation of the Lake Clark fault, Tyonek area, Alaska, State of Alaska Dept. of Natural Resources, Division of Geological and Geophysical Surveys, Preliminary Interpretative Report 2011-1, 12 p.

Koehler, R.D., Farrell, Rebecca-Ellen, Burns, P.A.C., and Combellick, R.A., 2012, Quaternary faults and folds in Alaska: A digital database, in Koehler, R.D., Quaternary Faults and Folds (QFF): Alaska Division of Geological & Geophysical Surveys Miscellaneous Publication 141, 31 p., 1 sheet, scale 1:3,700,000.

Koehler, R.D., Burns, P.A.C., and Weakland, J.R., 2013, Digitized faults of the Neotectonic map of Alaska (Plafker and others, 1994), in Koehler, R.D., Quaternary Faults and Folds (QFF): Alaska Division of Geological & Geophysical Surveys Miscellaneous Publication 150, 1 p.

Kuehn N., Bozorgnia Y., Campbell K.W., Gregor N., 2020, Partially nonergodic ground-motion model for subduction regions using NGA-Subduction database, PEER Report No. 2020/04: Pacific Earthquake Engineering Research Center, University of California, Berkeley, CA.

Lahr, J., Page, RA., Stephens, C.D., and Fogelman, K.A., 1986, Sutton, Alaska, earthquake of 1984-Evidence for activity on the Talkeetna segment of the Castle Mountain fault system: Bulletin of the Seismological Society of America, v. 76, p. 967-984.

Leonard, M., 2010, Earthquake fault scaling: Self-consistent relating of rupture length, width, average displacement, and moment release: Bulletin of the Seismological Society of America, v. 100, p. 1971–1988.

Lewis, K.A., Potter, C.J., Shah, A.K., Stanley, R.G., Haeussler, P.J., and Saltus, R.W., 2015, Preliminary Interpretation of Industry Two-Dimensional Seismic Data from Susitna Basin, South-Central Alaska: U.S. Geological Survey Open-File Report 2015-1138, 51 p.

Liberty, L.M., Finn, S.P., Haeussler, P.J., Pratt, T.L., Peterson, A., 2013, Megathrust splay faults at the focus of the Prince William Sound asperity: Alaska. Journal of Geophysical Research, v. 118, 1e14.

Lilhanand, K. and Tseng, W.S., 1988, Development and application of realistic earthquake time histories compatible with multiple-damping design spectra: Proceeding of the 9th World Conference on Earthquake Engineering, Tokyo-Kyoto, Japan.

Lin, T., Harmsen, S.C., Baker, J.W. and Luco, N., 2013, Conditional spectrum computation incorporating multiple causal earthquakes and ground-motion prediction models: Bulletin of the Seismological Society of America, v. 103(2A), p.1103-1116.

MacKay, P.A., Varsek, J.L., Kubli, T.E., Dechesne, R.G., Newson, A.C., and Reid, J.P., 1996, Triangle zones and tectonic wedges: An introduction: Bulletin of Canadian Petroleum Geology, v. 44, p. I-1–I-5.

Matmon, A., Schwartz, D.P., Haeussler, P.J., Finkel, R., Lienkaemper, J.J., Stenner, H.D., and others, 2006, Denali fault slip rates and Holocene-late Pleistocene kinematics of central Alaska: Geology, v. 34, p. 645-648.

Mériaux, A.-S., Sieh, K., Finkel, R. C., Rubin, C. M., Taylor, M. H., Meltzner, A. J., Ryerson, F.J., 2009, Kinematic behavior of southern Alaska constrained by westward decreasing postglacial slip rates on the Denali Fault, Alaska: Journal of Geophysical Research, v. 114, B03404.

Miller, A.C., and Rice, T.R., 1983, Discrete approximations of probability distributions: Management Science, v. 29, p. 352-362.

Molnar, P., 1979, Earthquake recurrence intervals and plate tectonics: Bulletin of the Seismological Society of America, v. 69, p. 115-133.

Moschetti, P.M., Thompson, E.M., Rekoske, J., Hearne, M.G., Powers, P.M., McNamara, D.E., and Tape, C., 2021, Ground-motion amplification in Cook Inlet region, Alaska, from intermediate-depth earthquakes, including the 2018 Mw 7.1 Anchorage Earthquake: Seismological Research Letters, v. 91, p. 142-152.

Murphy, L. M. and Cloud, W. K., 1953, United States Earthquakes 1951, Coast and Geodetic Survey: US Government Printing Office, no. 762, 50 p.

Nishenko, S.P., and Jacob, K.H., 1990, Seismic potential of the Queen Charlotte-Alaska-Aleutian-seismic zone: Journal of Geophysical Research, v. 95, p. 2511-2532.

Page, R.A., Biswas, N.N., Lahr, J.C., and Pulpan, H., 1991, Seismicity of Continental Alaska, The Geology of North America Decade Map, Neotectonics of North America: Geological Society of America, v. 1, p. 47-68.

Parker G.A., Stewart J.P., Boore D.M., Atkinson G.M., Hassani B., 2020, NGA-subduction global ground motion model with regional adjustment factors: PEER Report No. 2020/03, Pacific Earthquake Engineering Research Center, University of California, Berkeley, CA.

Perez, O.J., and Jacob, K.H., 1980, Tectonic model and seismic potential of the East Gulf of Alaska and Yakataga seismic gap: Journal of Geophysical Research, v. 88, p. 7132-7150.

Petersen, M.D., Cramer, C.H., and Frankel, A.D., 2002, Simulations of Seismic Hazard for the Pacific Northwest of the United States from Earthquakes Associated with the Cascadia Subduction Zone: Pure and Applied Geophysics, v. 159, p. 2147-2168.

Petersen, M.D., Frankel, A.D., Harmsen, S.C., Mueller, C.S., Haller, K.M., Wheeler, R.L., Wesson, R.L., Zeng, Y., Boyd, O.S., Perkins, D.M., Luco, N., Field, E.H., Wills, C.J., and Rukstales, K.S., 2014, Documentation for the 2014 update of the United States National Seismic Hazard Maps: U.S. Geological Survey Open-File Report 2014-1091, 243 p.

Plafker, G., Hudson, T., and Richter, D.H., 1977, Preliminary observations on late Cenozoic displacements along the Totschunda and Denali fault system, in Blean, K.M., ed., The U.S. Geological Survey in Alaska: Accomplishments during 1976: U.S. Geological Survey Circular 751B, p. B67-B69.

Plafker, G., Moore, J.C., and Winkler, G.R., 1994, Neotectonic map of Alaska, in Plafker, G., and Berg, H.C., eds., The Geology of Alaska: Geology of North America, Geological Society of America, G-1, scale 1:2,500,000.

Plafker, G.F., and Rubin, M., 1994, Paleoseismic evidence for “yo-yo” tectonics above the eastern Aleutian subduction zone – Coseismic uplift alternating with even larger interseismic submergence, in Proceedings of the Workshop on Paleoseismology, Prentice, C.S., Schwartz, D.P., and Yeats, R.S., Conveners: U.S. Geological Survey Open-File Report 94-568, p. 155-157.

Plaflker, G., 1969, Tectonics of the March 27, 1964, Alaska earthquake: U.S. Geological Survey Professional Paper 543-I 74 p.

Reed, B.L., and Lanphere, M.A., 1974, Offset plutons and history of movement along the McKinley segment of the Denali fault system, Alaska: Geological Society of America Bulletin, v. 85, p. 1883-1892.

Ruppert, N.A., Holtkamp, S.G., and Murphy, N., 2022, Performance review of AK regional seismic network for 2019-2021 with focus on field site telemetry and power: Alaska Earthquake Center.

Savage, J.C., Svarc, J.L., and Prescott, W.H., 1999, Deformation across the Alaska-Aleutian subduction zone near Kodiak: Geophysical Research Letters, v. 26, p. 2117-2120.

Schmoll, H.R., and Yehle, L.A., 1987, Surficial geologic map of the northwestern quarter of the Tyonek A-4 Quadrangle, south-central Alaska: U.S. Geological Survey Miscellaneous Field Studies Map MF-1934, 1 sheet, scale 1:31,680.

Schwartz, D.P. and Coppersmith, K.J., 1984, Fault behavior and characteristic earthquakes--examples from the Wasatch and San Andreas fault zones: Journal of Geophysical Research, v. 89, p. 5681-5698.

Schwartz, D.P., Haeussler, P.J., Seitz, G.G., Dawson, T.E., Stenner, H.D., 2005, Unraveling the earthquake history of the Denali fault system, Alaska – Filling a blank canvas with paleoearthquakes: EOS Transactions, American Geophysical Union, v. 86, Fall Meeting Supplement, Abstract U42A-06.

Shellenbaum, D.P., Gregersen, L.S., and Delaney, P.R., 2010, Top Mesozoic unconformity depth map of the Cook Inlet Basin, Alaska: Alaska Division of Geological and Geophysical Surveys, report of investigations 2010-2 sheet 1 of 1.

Shennan, I., and Hamilton, S., 2006, Coseismic and pre-coseismic subsidence associated with great earthquakes in Alaska: Quaternary Science Reviews, v. 25, p. 1-8.

Shennan, I., Bruhn, R., and Plafker, G., 2009, *et al*. Multi-segment earthquakes and tsunami potential of the Aleutian megathrust: Quaternary Science Reviews, v. 28, p. 7-13.

Shennan, I., Bruhn, R., Barlow, N.L.M., Good, K., and Hocking, E.P., 2014, Late Holocene great earthquakes in the eastern part of the Aleutian megathrust: Quaternary science reviews, v. 84, p. 86-97.

Silva, W.J., Abrahamson, N., Toro, G., and Costantino, C, 1997, Description and Validation of the Stochastic Ground Motion Model: unpublished report prepared for Brookhaven National Laboratory by Pacific Engineering and Analysis.

Stover, C.W., and Coffman, J.L., 1993, Seismicity of the United States, 1568-1989 (Revised): U.S. Geological Survey Professional Paper 1527, 415 p.

Tape, C., and Haeussler, P.J., 2019, Tectonic and Geologic Setting of the 2018 Anchorage Earthquake: presentation at the Anchorage Earthquake Conference, 9/24/2019

Tichelaar, B.W., and Ruff, L.J., 1993, Depth of seismic coupling along subduction zones: Journal of Geophysical Research, v. 98, p. 2017-2037.

Tinti, S., and Mulargia, F., 1985, Completeness analysis of a seismicity catalog: Annals of Geophysics, v.3, p.407–414.

Travasarou, T., Bray, J.D., and Abrahamson, N.A., 2003, Empirical attenuation relationship for Arias intensity: Earthquake Engineering and Structural Dynamics, v. 32, p. 1133-1155.

Trifunac, M. D. and Brady, A.G., 1975, On the correlation of seismic intensity scales with the peaks of recorded strong ground motion: Bulletin of the Seismological Society of America, v. 65, p. 139–162.

United States Geological Survey (USGS), 2008, Deaths in the United States from Earthquakes, http://earthquake.usgs.gov/regional/states/us_deaths.php

U.S. Geological Survey, 2021, Preliminary earthquake catalog for use in the National Seismic Hazard Mapping Project Update of the Alaska Seismic Hazard Maps: unpublished database provided by P. Powers, Nov 29, 2021.

Veilleux, A.M., and Doser, D.I., 2007, Studies of Wadati-Benioff zone seismicity of the Anchorage, Alaska, Region: Bulletin of the Seismological Society of America, v. 97, p. 52-62.

Watson-Lamprey, J. and Abrahamson, N., 2006, Selection of ground motion time series and limits on scaling: Soil Dynamics and Earthquake Engineering, v. 26, p. 477-482.

Wells, D.L. and Coppersmith, K.J., 1994, New empirical relationships among magnitude, rupture length, rupture width, rupture area, and surface displacement: Bulletin of the Seismological Society of America, v. 84, p. 974-1002.

Wesnousky, S.G., 1986, Earthquakes, Quaternary faults, and seismic hazard in California: Journal Geophysical Research, v. 91, p. 12,587-12,631.

Wesson, R.L., Boyd, O.S., Mueller, C.S., Bufe, C.G., Frankel, A.D., and Petersen, M.D., 2007, Revision of time-independent probabilistic seismic hazard maps for Alaska: U.S. Geological Survey Open-File Report 2007-1043, 33 p.

West, M.E., Bender, A., Gardine, M., Gardine, L., Gately, K., Haeussler, P., Hassan, W., Meyer, F., Richards, C., Ruppert, N.A., *et al*., 2019, The 30 November 2018 MW 7.1 Anchorage Earthquake: Seismological Research Letters, v. 91, p. 66-84.

Wilson, F.H., Hults, C.P., Schmoll, H.R., Haeussler, P.J., Schmidt, J.M., Yehle, L.A., Labay, K.A., 2012, Geologic map of the Cook Inlet region, Alaska, including parts of the Talkeetna, Talkeetna Mountains,

Tyonek, Anchorage, Lake Clark, Kenai, Seward, Iliamna, Seldovia, Mount Katmai, and Afognak, USGS SIM 2153, 76 p., 2 sheets, sale 1:250,000.

Willis, J.B., Haeussler, P.J., Bruhn, R.L., Willis, G.C., 2007, Holocene slip rate for the western segment of the Castle Mountain fault, Alaska: Bulletin of the Seismological Society of America, v. 97, p. 1019–1024, June 2007.

Witter, R., Briggs, R., Dura, T., Engelhart, S., Nelson, A., Koehler, R., and Haeussler, P., 2022, Paleoseismological perspectives on megathrust locking, rupture, and tsunami hazard in Alaska: Seismological Society of America Annual Meeting, USGS.

Wong, I., Dawson, T., Dober, M., Russon, L., Knudsen, K., Terra, F., 2008, Site-specific probabilistic and deterministic seismic hazard analysis and development of earthquake ground motions for the Port of Anchorage Expansion Project, URS Corporation, prepared for Terracon Consultants, Inc., 120 p.

Wong, I. and Thomas, P., 2020, Implementing time-dependent seismic hazard in seismic design and building codes: it's time!: 17th World Conference on Earthquake Engineering, 17WCEE.

Wong, I., Thomas, P., Zachariasen, J., Bott, J., and Terra, F., 2014a, Site-specific seismic hazard analyses and development of earthquake ground motions for the Anchorage Port modernization project, Alaska: URS report prepared of Municipality of Anchorage.

Wong, I., Dober, M., and Zachariasen, J., 2014b, Earthquake ground shaking hazards in Anchorage, Alaska: Tenth U.S. National Conference on Earthquake Engineering Proceedings (CD-ROM).

Worthington, L.L., Van Avendonk, H.J.A., Gulick, S.P.S., Christeson, G.L., and Pavlis, T.L., 2012, Crustal structure of the Yakutat terrane and the evolution of subduction and collision in southern Alaska: Journal of Geophysical Research, v. 117, p. B01102.

Youngs, R.R. and Coppersmith, K.J., 1985, Implications of fault slip rates and earthquake recurrence models to probabilistic seismic hazard estimates: Bulletin of the Seismological Society of America, v. 75, p. 939-964.

Zoback, M.D., and Zoback, M.L., 1991, Tectonic stress field of North America and relative plate motions in Slemmons, D.B., Engdahl, E.R., Zoback, M.D., and Blackwell, D.D., eds., Neotectonics of North America: Boulder, Colorado, Geological Society of America, Decade Map Volume 1, p. 339-366.

Zweck, C., Freymueller, Cohen, S.C., 2002, Three-dimensional elastic dislocation modeling of the postseismic response to the 1964 Alaska earthquake: Journal of Geophysical Research, v. 107, p. ECV 1-1 to 1-12.

Tables

Table 1. Seismic Source Parameters for Quaternary Faults Used in the Analysis

FAULT NAME	RUPTURE MODEL	STYLE[1]	MAXIMUM RUPTURE LENGTH[2] (km)	MAXIMUM MAGNITUDE[3] (Mw)	DIP[4] (degrees)	MAXIMUM SEISMOGENIC DEPTH[5] (km)	PROBABILITY OF ACTIVITY[6]	SLIP RATE[7] (mm/yr)	COMMENTS
Broad Pass Thrust	Floating (0.5)	R	100	7.1 (0.2) 7.4 (0.6) 7.7 (0.2)	30 NW (0.2) 40 NW (0.6) 50 NW (0.2)	10 (0.2) 15 (0.6) 20 (0.2)	0.7	0.1 (0.3) 1.0 (0.4) 4.0 (0.3)	The Broad Pass fault represents a prominent bedrock structure south of the Denali fault at Broad Pass. As summarized by Haeussler *et al*. (2017b), the structure merges with the Denali fault at a location coincident with a 3 mm/yr decreases in the Denali fault slip rate with no other clear fault candidates to account for the slip rate change (Haeussler *et al*., 2017a, Haeussler *et al*., 2017b). The broad pass fault is interpreted as a low-angle thrust, although little is known about the fault and evidence for late Quaternary activity is equivocal. Our brief review of 10-m topography along the length of the fault found that much of the rangefront is characterized by fault-parallel glacial landforms or neoglacial features that would make identification of a blind structure difficult. There is no clear indication of fault scarps like those along the Castle Mountain and Pass Creek faults, suggesting that if the fault has been active since the LGM, deformation is likely blind. Haeussler *et al*. (2017a) indicate that in addition to the co-location of the fault and the slip rate change on the Denali, clear evidence for latest Pleistocene to Holocene normal fault activity on the Pass Creek fault in the hanging wall of the Broad Pass thrust supports an active designation. The Broad Pass was not included in the Koehler *et al*. (2012) Alaska Q fault database but is now included as a proposed source for the 2023 NSHM (Bender *et al*., 2021) based on the Haeussler *et al*. (2017a, 2017b) studies. Because the fault is ~200 km long and dips shallowly, it may have the potential to produce very large earthquakes (> M 7.5), although nothing is known of the rupture history and whether or not the entire fault could rupture in a single earthquake. Because of this uncertainty, we include scenarios for both a 100-km-long floating rupture and a 204-km full rupture. Haeussler *et al*. (2017a) note that if the fault does account for the full rate decrease along the Denali then the shortening rate across the fault could be as high as 4 mm/yr, yielding a dip-slip rate well above this. However, because the fault lacks clear evidence of recent activity along the mapped trace, we use 4 mm/yr as the upper slip rate bound.
	Full Rupture (0.5)		204	7.4 (0.2) 7.7 (0.6) 8.0 (0.2)					
Bruin Bay Fault	Floating (1.0)	R	35 (0.7) 100 (0.3)	6.6 (0.2) 6.9 (0.6) 7.2 (0.2) 7.1 (0.2) 7.4 (0.6) 7.7 (0.2)	30 NW (0.2) 45 NW (0.6) 60 NW (0.2)	15 (0.2) 20 (0.6) 25 (0.2)	0.5	0.01 (0.4) 0.2 (0.4) 0.5 (0.2)	The Bruin Bay fault represents a major tectonic structure that defines the northwest margin of the Cook Inlet. Schmoll and Yehle (1987) found no geologic evidence of activity on the Bruin Bay fault or related structures during late Pleistocene or Holocene time (the last~120,000 years) and the fault is classified as a Neogene fault by Plafker *et al*. (1994). However, there is some uncertainty whether there are enough Quaternary deposits spanning the fault and spanning a larger (pre-LGM) time period to preclude Quaternary activity. Based on the apparent lack of activity during the past 120,000 years, we assign a slip rate that is low, with broad uncertainties to reflect the potential for large but infrequent earthquakes on the fault. Our rate distribution encompasses the Oligocene uplift rate of 0.2-0.4 mm/yr presented by Betka *et al*. (2017). Because the fault is in a favorable orientation for activity in the present stress regime, we believe that it may still be capable of producing moderate to large earthquakes. In addition, the northeastern terminus of the fault is co-located with the southwest end of the Castle Mountain fault, interpreted as the break between the Holocene active Castle Mountain fault to the northeast and the far less active or inactive Lake Clark fault to the southwest. The coincidence of the Bruin Bay fault intersection and the change in activity along the Castle Mountain/Lake Clark faults supports potential activity on the Bruin Bay fault. Alternatively, the folds and associated faults in the Cook Inlet to the east could accommodate nearly all of the change in rate along the Castle Mountain-Lake Clark system without a Bruin Bay contribution. We assign an Mmax in the shorter of the two floating earthquake models based on the historical 1933 M 6.9 earthquake that occurred in the Cook Inlet, suggesting that earthquakes of at least this size, along parallel structures, are possible in the region. In addition, we consider a larger (100-km) floating rupture along the Bruin Bay fault, as the structure (composite of many faults) is much longer than the other Cook Inlet faults to the east. Given the equivocal evidence for Quaternary

FAULT NAME	RUPTURE MODEL	STYLE[1]	MAXIMUM RUPTURE LENGTH[2] (km)	MAXIMUM MAGNITUDE[3] (Mw)	DIP[4] (degrees)	MAXIMUM SEISMOGENIC DEPTH[5] (km)	PROBABILITY OF ACTIVITY[6]	SLIP RATE[7] (mm/yr)	COMMENTS
									activity, and the fault's exclusion from the Koehler *et al*. (2012) and Bender *et al*. (2021) active fault and seismic source compilations (respectively), we assign a P(a) of 0.5 to the Bruin Bay fault.
Bulchitna Lake	Full Rupture (1.0)	R	34	6.5 (0.2) 6.8 (0.6) 7.1 (0.2)	45 E (0.3) 60 E (0.4) 75 E (0.3)	10 (0.2) 15 (0.6) 20 (0.2)	1.0	0.1 (0.3) 0.5 (0.4) 1.2 (0.3)	The Bulchitna Lake fault represents a north striking fault with a southern endpoint located between the northern ends of Mt. Susitna and Little Mt. Susitna, about 15 km northwest of the Susitna River. The northern end of the fault is located up to 34 km to the north (per Haeussler *et al*, 2017) based on seismic reflection presented by Lewis *et al*. (2015). The fault is recognized from LiDAR-based elevation models (Haeussler *et al*., 2017a, this study) and from seismic reflection data presented by Lewis *et al*. (2015). The fault vertically displaces latest Pleistocene and younger deposits and Mesozoic bedrock in an up-to-the-east sense, like the adjacent Leech Lake and Kahiltna faults to the east. Maximum vertical surface displacement appears to be similar to the Kahiltna's 13 m, the with max height more likely including pre-LGM Quaternary offset. Haeussler *et al*. (2017a) indicate only 3-4 m of surface displacement for the Kahiltna, but profiles cut for this study appear to support significantly more displacement. Like the adjacent Kahiltna, the Bulchitna Lake fault generally lacks the acute scarps of other faults observed in the region, suggesting it may be partially blind, accommodates a lower slip rate, or has not ruptured since the time during or immediately after the LGM. Clear evidence for latest Pleistocene to Holocene faulting warrants a P(a) of 1.0, while vertical surface displacement warrants a maximum slip rate range of about 1.2 mm/yr if the displacement is almost entirely postglacial. The preferred rate is 0.5 mm/yr assuming a little more than half of the surface displacement is postglacial.
Castle Mountain – Caribou Fault System	Layered (1.0)	SS (0.75)			70 N (0.5)	10 (0.2)			At a distance of 38 km from the POA, the Holocene-active Castle Mountain – Caribou Fault System is the closest fault source to the site with a preferred slip rate > 1mm/yr. Based on mapping by Detterman *et al*. (1976) and seismicity analysis following the Mb 5.7 1984 earthquake and aftershock sequence (Lahr *et al*., 1986), the fault likely dips approximately 70° to 90° north. Willis *et al*. (2007) documented post-last glacial maximum (LGM) displacements along the western section of the fault zone and calculated dextral slip rates that ranged from 2.1 to 3.6 mm/yr with no more than a few meters of vertical displacement. More recent work in preparation for the Alaska hazard map update presented by Tape and Haeussler (2019) documents mostly vertical deformation along the fault from detailed topography review. However, based on the focal mechanisms (e.g., Lahr *et al*., 1986), near-vertical fault, evidence for limited shortening related to the last three or four events (Haeussler *et al*, 2002), and evidence for primarily lateral displacement (Willis *et al*., 2007, this study), we model the fault as primarily strike slip. Along the Holocene active section, our review of the LiDAR-based 10-m digital elevation model (DEM) found an obvious and remarkably linear to curvilinear series of scarps that each extend largely unbroken for many kilometers. These scarps are typically several meters high and almost exclusively display down-to-the-southeast displacement. The section with unequivocal post-LGM morphology extends for at least 62 km (modeled as 80 given limitations of fault visibility at east and west ends) and has a midpoint that is nearly the closest approach of the fault to the POA. En-echelon left steps along the fault are locally abundant. Additionally, the few locations of clear left (restraining) and right (releasing) steps are associated with localized graben and/or bulges interpreted to represent localized extension and shortening, respectively. These features are consistent with a dextral fault accommodating some oblique shortening on a north-dipping structure. Based on evidence for repeated Holocene activity along the Western section (recurrence interval of ~700 years), with only Pleistocene activity identified on the Eastern section (Haeussler *et al*., 2002), we consider a layered model for the Castle Mountain fault. This is the only fault in the Anchorage area (< 50 km) with both a constrained slip rate and a constrained Late Holocene earthquake chronology. The fault has ruptured four times during the past 2700 years (Haeussler *et al*., 2002). To adequately model hazard along the highest rate section of the Castle Mountain, we utilize two
	Western (most active)	R (0.25)	62	6.8 (0.2) 7.1 (0.6) 7.4 (0.2)	90 (0.5)	15 (0.6) 20 (0.2)	1.0	1.12 (0.2) 2.06 (0.6) 2.625 (0.2)	
	Western (Full)		108	7.0 (0.2) 7.3 (0.6) 7.6 (0.2)			1.0	0.375 (0.2) 0.69 (0.6) 0.875 (0.2)	
	Eastern + Caribou		85	6.9 (0.2) 7.2 (0.6) 7.5 (0.2)			0.6	0.005 (0.2) 0.25 (0.6) 0.5 (0.2)	
	Full Rupture		193	7.4 (0.2) 7.7 (0.6) 8.0 (0.2)			1.0	0.005 (0.2) 0.25 (0.6) 0.5 (0.2)	

FAULT NAME	RUPTURE MODEL	STYLE[1]	MAXIMUM RUPTURE LENGTH[2] (km)	MAXIMUM MAGNITUDE[3] (Mw)	DIP[4] (degrees)	MAXIMUM SEISMOGENIC DEPTH[5] (km)	PROBABILITY OF ACTIVITY[6]	SLIP RATE[7] (mm/yr)	COMMENTS
									segments in a layered format for the western section; the geomorphically youthful 62-km section carries 75% of the total western section target rate while the full western section carries the remaining 25 percent (distributed over two layers), resulting in overlap section carrying the full rate of 1.5, 3.0, and 4.0 mm/yr, respectively. Because of the apparent along-strike continuity of the fault in map view between the Western and Eastern sections, we also include a floating rupture model that is allowed to rupture anywhere along the fault system. However, this is given a relatively low weight because of the paleoseismic record that clearly shows the Western Castle Mountain fault has repeatedly ruptured during the Holocene, while the Eastern Castle Mountain (Caribou) fault has not. This is consistent with the clear morphology along the western section and apparent lack thereof on the eastern section. Due to this apparent lack of recent activity, and the suggestion that the slip rate should decrease to the east due to being on the edge of the Yakutat – North America collision that may drive the Castle Mountain Fault, we assign the Eastern Castle Mountain – Caribou Fault System a lower preferred and max slip rate compared to the Western Castle Mountain fault.
Denali Fault System	Floating (0.5)	SS	90 (0.4)	6.9 (0.2)	75 N (0.2)	10 (0.2)	1.0	5.0 (0.2)	We consider the three segments of the Denali Fault System closest to the 200 km radius surrounding the Port of Alaska in our source model, despite the fault being entirely beyond the 200-km radius. Due to the relatively continuous trace, we consider both floating and segmented models to reflect rate decreases and fault geometry changes. Segments are defined by the sections shown in the Haeussler *et al*. (2017b), with slip rates from individual sections utilizing the Haeussler *et al*. (2017a) slip rate summary. In lieu of developing a more complex layered model for the floating scenarios, we utilize the average slip rate of 8 ± 3 mm/yr (same as the center west section) for the full length given the relatively consistent drop in slip rate from east to west along the fault. We utilize the full rupture length of the 2002 event for the larger of the two floating events and a 90-km length, consistent with evidence of smaller events in the M7.2-7.4 range (Carver *et al*., 2004), and full segment lengths for the segment scenarios.
				7.2 (0.6)	90 (0.6)	15 (0.6)		8.0 (0.6)	
				7.5 (0.2)	75 S (0.2)	20 (0.2)		11.0 (0.2)	
			320 (0.6)	7.5 (0.2)					
				7.8 (0.6)					
				8.1 (0.2)					
	Segmented (0.5)								
	West		255	7.4 (0.2)				3.0 (0.2)	
				7.7 (0.6)				5.0 (0.6)	
				8.0 (0.2)				7.0 (0.2)	
	Center West		112	7.0 (0.2)				5.0 (0.2)	
				7.3 (0.6)				8.0 (0.6)	
				7.6 (0.2)				11.0 (0.2)	
	Center		93	7.0 (0.2)				8.0 (0.2)	
				7.3 (0.6)				11.0 (0.6)	

FAULT NAME	RUPTURE MODEL	STYLE[1]	MAXIMUM RUPTURE LENGTH[2] (km)	MAXIMUM MAGNITUDE[3] (Mw)	DIP[4] (degrees)	MAXIMUM SEISMOGENIC DEPTH[5] (km)	PROBABILITY OF ACTIVITY[6]	SLIP RATE[7] (mm/yr)	COMMENTS
				7.6 (0.2)				13.0 (0.2)	
Kahiltna	Full Rupture (1.0)	R	26	6.4 (0.2) 6.7 (0.6) 7.0 (0.2)	45 E (0.3) 60 E (0.4) 75 E (0.3)	10 (0.2) 15 (0.6) 20 (0.2)	1.0	0.05 (0.3) 0.5 (0.4) 1.2 (0.3)	The Kahiltna fault represents a north striking fault with a southern endpoint located between the northern ends of Mt. Susitna and Little Mt. Susitna, about 15 km northwest of the Susitna River. The northern end of the fault is located 34 km to the north. Much like the Bulchitna fault to the east, the Kahiltna fault is recognized from LiDAr-based elevation models (Haeussler *et al*., 2017a, this study) and from seismic reflection data presented by Lewis *et al*. (2015). The fault vertically displaces latest Pleistocene and younger deposits and Mesozoic bedrock in an up-to-the-east sense, like the adjacent Leech Lake and Bulchitna faults to the east and west, respectively. Maximum vertical surface displacement is 13 m (Haeussler *et al*, 2017a) the with max height more likely including pre-LGM Quaternary offset. Like the adjacent Bulchitna, the Kahiltna fault generally lacks the acute scarps of other faults observed in the region, suggesting it may be partially blind or accommodates a lower slip rate. Clear evidence for latest Pleistocene to Holocene faulting warrants a P(a) of 1.0, while vertical surface displacement warrants a maximum slip rate range of about 1.2 mm/yr if the displacement is almost entirely postglacial. The preferred rate is 0.5 mm/yr assuming a little more than half of the surface displacement is postglacial.
Lake Clark Fault	Floating (0.7)	R (0.25) SS (0.75)	20	6.2 (0.2) 6.5 (0.6) 6.8 (0.2)	75 N (0.5) 90 (0.5)	10 (0.2) 15 (0.6) 20 (0.2)	0.6	0.01 (0.2) 0.05 (0.6) 0.5 (0.2)	The Quaternary activity of the Lake Clark remains poorly understood, but in general, the fault lacks the clear evidence of post-LGM displacement that the adjacent Castle Mountain fault displays. Schmoll and Yehle (1987) report some evidence for Pleistocene movement, but no Holocene movement along the fault near its intersection with the Castle Mountain Fault. More recently, Koehler and Reger, 2011 reviewed as section the Lake Clark fault near its west end and found no compelling evidence for offset OIS stage 4 (~70 ka) or younger glacial deposits. We reviewed sections of the fault in this area as well and the large outwash fans of the Chuitkilnachna River (about 25 m above the modern channel) are clearly undisturbed within the limit of resolution, further supporting a lack of post-LGM deformation. As such, we utilize a lower probability of activity of 0.6 together with a low slip rate. We include three rupture models to characterize the behavior of this fault. Very little weight is given to an unsegmented rupture model, based on an apparent discontinuous trace between the western and eastern sections. We give higher weight to a floating earthquake model with a magnitude set at near the threshold of surface rupture. This is our preferred rupture model because it implies that, if the fault is active, displacements would be relatively small, and geomorphic evidence of recent activity would be quickly erased and not identifiable in this climate. The slip rate is poorly constrained for the Lake Clark Fault. The average slip rate over the past 34-39 Ma is about 0.7 mm/yr (Haeussler and Saltus, 2004). However, this may be an overestimate for current slip rates given the lack of demonstrable Quaternary deformation along the length of this fault. Based on this, and the general lack of information regarding shorter term slip rates on this fault, we assign a preferred slip rate of 0.05 mm/yr to reflect the notion that, if this fault is active, it has a very low slip rate and consequently, very little geomorphic signature indicative of active tectonics.
	Full Rupture (0.1)		247	7.4 (0.2) 7.7 (0.6) 8.0 (0.2)					
	Segmented (0.2)								
	Western		116	7.1 (0.2) 7.4 (0.6) 7.7 (0.2)					
	Eastern		134	7.1 (0.2) 7.4 (0.6) 7.7 (0.2)					
Leech Lake	Full Rupture (1.0)	R	31	6.5 (0.2) 6.8 (0.6)	45 E (0.3) 60 E (0.4)	10 (0.2) 15 (0.6)	0.9	0.1 (0.3) 0.3 (0.4)	The Leech Lake fault, as named for this study, represents a north-south-striking fault that offsets LGM glacial and post-LGM outwash/terrace deposits near the confluence of the Yentna and Susitna Rivers, approximately 10 km due north of the Castle Mountain fault. The fault is parallel to and about 5-6 km east of the Kahiltna River fault. Similar to the adjacent Bulchitna and Kahiltna faults, the

FAULT NAME	RUPTURE MODEL	STYLE[1]	MAXIMUM RUPTURE LENGTH[2] (km)	MAXIMUM MAGNITUDE[3] (Mw)	DIP[4] (degrees)	MAXIMUM SEISMOGENIC DEPTH[5] (km)	PROBABILITY OF ACTIVITY[6]	SLIP RATE[7] (mm/yr)	COMMENTS
				7.1 (0.2)	75 E (0.3)	20 (0.2)		0.5 (0.3)	Leech Lake fault displays offset in a down-to-the-west sense, with the largest displacements approaching four meters, but mostly about 2.5 to 3 m across the highest outwash deposits. Scarps on younger/lower surfaces are typically smaller, but unlike the Bulchitna and Kahiltna, scarps are sharp and acute. Scarp heights suggest a vertical rate of about 0.2 to 0.3 mm/yr assuming the deposits postdate the ~11 ka LGM. Dip slip rates of up to about 0.4 mm/yr are calculated an assumed 60° dipping (west-dipping) fault. The Leech Lake fault is not included in any of the published active fault databases for Alaska (e.g., Koehler *et al*., 2012 and related USGS Q-fault database, Bender *et al*., 2021) nor is it mentioned in publications of faulting in Susitna Basin or Cook Inlet region folds (e.g., Haeussler and Saltus, 2011; Haeussler *et al*, 2017a). The southern half of the source is well expressed west of the Yentna River but the fault intersects and likely parallels the river along the its northern half, where geomorphic expression is more subdued and equivocal. Despite clear evidence of late-glacial and post-glacial fault scarps, we assign a P(a) of 0.9 for the Leech Lake fault because it is not documented in the available literature. We recognize a subtle topographic high to the south in glacioestuarine deposits (which should be nearly flat) that may be related to post-glacial uplift/fold growth and a possible southerly extension of the Leech Lake fault. Alternatively, this could be a postglacial isostatic adjustment feature (Peter Haeussler, pers comm., June 2022) but it is quite localized along the projection of the Leech Lake fault. This area occurs a largely uneroded glacioestuarine surface (Wilson *et al*., 2012) that extends parallel to the Susitna River for approximately 16 km. South of the Susitna River and along strike of the Leech Lake fault, the surface appears to be warped/uplifted approximately 3 m (similar to the vertical displacement observed across the scarps) over a fault-parallel elongated area 3-4 km long. The apparent uplift is prominent when viewed on Susitna River-parallel topographic profiles. As such, we conservatively extend the Leech Lake fault an additional 7 km south to include the area of apparent uplift, with recognition that additional study is necessary to better evaluate this structure. The total length of the source is 31 km.
Montague Strait Fault	Full Rupture (1.0)	N	75	6.9 (0.2) 7.2 (0.6) 7.5 (0.2)	45 SE (0.3) 60 SE (0.4) 75 SE (0.3)	10 (0.2) 15 (0.6) 20 (0.2)	0.2	2.0 (0.3) 3.7 (0.4) 5.0 (0.3)	The Montague Strait fault represents an ~75-km-long normal fault in the accretionary wedge that overrides the megathrust. The fault is clearly defined by both bathymetry and from thermochronology-based exhumation rates calculated by Haeussler *et al*. (2015) for the Prince William Sound region that also includes the Patton Bay fault. While this source is considered independent of the subduction zone as a source of strong ground shaking based on the occurrence of seismicity along the fault, we recognize that the fault *may* largely accommodate strain during megathrust events. Haeussler *et al*. (2015) interpret a dip of 61° SE based on the nodal plane solution from a 2012 M4.8 earthquake on the fault. Given that the source is nearly 200 km from the site, we consider only a full rupture for the source model. Ongoing work suggests that splay faults of the megathrust (e.g., Patton Bay) rupture during megathrust events, although not during every event (Peter Haeussler, pers. comm., June 2022). As such, we assign a low P(a) to the source to represent the low likelihood of the fault producing a large rupture independent of a megathrust event. Slip rate for the Montague straight is based on the 3.6 and 41 m offsets of the neoglacial and LGM unconformities, respectively.
Pass Creek	Full Rupture (1.0)	N	45	6.7 (0.2) 7.0 (0.6) 7.3 (0.2)	45 N (0.2) 60 N (0.6) 75 N (0.2)	15 (0.2) 20 (0.6) 25 (0.2)	1.0	0.1 (0.2) 0.3 (0.6) 0.7 (0.2)	This Pass Creek fault occurs as a north-dipping normal fault in the hanging wall of the Broad Pass thrust, likely the result of a ramp-flat transition or a triangle zone (MacKay *et al*., 1996). The fault vertically displaces latest Pleistocene to early Holocene glacial deposits (interpreted as ~11 ka) up to 6 m, as reported by Haeussler *et al*. (2017). They document a preferred fault dip of 38° related to the scarp itself, which a steep fault scarp and suggests recent activity. The subsurface dip is unknown. Using a dip of 50° and an 11-ka age for the offset deposits yields a maximum dip slip rate of 0.7 mm/yr, which we utilize as the upper slip rate bound. The total source length is approximately 45 km using a combination of the Bender *et al*. (2021) and the slightly longer Koehler *et al*.

FAULT NAME	RUPTURE MODEL	STYLE[1]	MAXIMUM RUPTURE LENGTH[2] (km)	MAXIMUM MAGNITUDE[3] (Mw)	DIP[4] (degrees)	MAXIMUM SEISMOGENIC DEPTH[5] (km)	PROBABILITY OF ACTIVITY[6]	SLIP RATE[7] (mm/yr)	COMMENTS
									(2012) geometries. Clear evidence of post-glacial deformation warrants a P(a) of 1.0.
Patton Bay Fault	Full Rupture	R	90	7.0 (0.2) 7.3 (0.6) 7.6 (0.2)	40 NW (0.3) 55 NW (0.4) 70 NW (0.3)	10 (0.2) 15 (0.6) 20 (0.2)	0.2	2.0 (0.3) 5.0 (0.4) 7.0 (0.3)	The Patton Bay fault represents a reverse fault splay of the megathrust, located nearly 200 km west of the site. The fault accommodated up to 12 m of displacement during the historic megathrust event. Ongoing work suggests the fault rupture during megathrust events, although not during every event (Peter Haeussler, pers. comm., June 2022). As such, we assign a low P(a) to the source to represent the low likelihood of the fault producing a large rupture independent of a megathrust event. The slip rate estimate is developed from the post-LGM vertical displacement of 56 m (in ~ 11 to 15 ka) by Liberty *et al*. (2013) on a fault dipping 55°, yielding a dip slip rate of about 5 to 7 mm/yr. We use 2 mm/yr as the inferred lower bound given data presented in Liberty *et al*. (2013)
COOK INLET – BLIND SOURCES*									
Middle Ground Shoal + Granite Point	Full Rupture (1.0)	R	63	6.9 (0.2) 7.2 (0.6) 7.5 (0.2)	45 NW (0.3) 60 NW (0.4) 75 NW (0.3)	15 (0.2) 20 (0.6) 25 (0.2)	1.0	0.39 (0.3) 0.82 (0.4) 2.72 (0.3)	This pair of structures deforms Pliocene deposits and may deform Quaternary sediments (Haeussler *et al*., 2000). Slip rate is based on the range of possible slip rates reported by Haeussler *et al*. (2000). Geometry for this source uses Haeussler and Saltus (2011) and Bender *et al*. (2021).
Kenai Lowlands (*formerly Naptown + Sunrise Lake + Beaver Creek*)	Full Rupture (1.0)	R	55	6.8 (0.2) 7.1 (0.6) 7.4 (0.2)	45 NW (0.3) 60 NW (0.4) 75 NW (0.3)	15 (0.2) 20 (0.6) 25 (0.2)	0.3	0.39 (0.3) 0.82 (0.4) 2.72 (0.3)	The Kenai Lowlands homocline (Haeussler and Saltus, 2011; Haeussler *et al*., 2000) is located several kilometers east of the Swanson River anticline and is likely composed of several inferred sub-parallel structures. Collectively, these structures deform Pliocene deposits and may deform Quaternary sediments (Haeussler *et al*., 2000). There are no independent slip rate estimates available. We have applied the range of possible slip rates reported by Haeussler *et al*. (2000) for the Middle Ground Shoal as a proxy for this structure. The Kenai Lowlands source is not included in either the Koehler *et al*. (2012) Alaska active fault database or the Bender *et al*. (2021) proposed 2023 NSHM sources. However, given the possibility that it *may* deform Quaternary-age deposits and it's orientation is consistent with the modern strain field, we include it as a crustal source, albeit with a low P(a).
North Cook Inlet-SRS Anticline	Full Rupture (1.0)	R	23	6.4 (0.2) 6.7 (0.6) 7.0 (0.2)	45 NW (0.3) 60 NW (0.4) 75 NW (0.3)	15 (0.2) 20 (0.6) 25 (0.2)	1.0	0.04 (0.3) 0.08 (0.4) 0.27 (0.3)	The North Cook Inlet anticline likely folds Quaternary sediments (Haeussler el al., 2000) and has been attributed as one of the possible sources of the 1933 M 6.9 earthquake (Haeussler *et al*., 2000; Flores and Doser, 2005). We use this magnitude as the preferred Mmax for this structure. Slip rate is based on Haeussler *et al*. (2000). The more recent work by Haeussler and Saltus (2011) considers the North Cook Inlet and SRS anticlines to be part of one structure, as model for this seismic hazard analysis.
Lewis River – Beluga River	Full Rupture (1.0)	R	35	6.6 (0.2) 6.9 (0.6) 7.2 (0.2)	45 NW (0.3) 60 NW (0.4) 75 NW (0.3)	15 (0.2) 20 (0.6) 25 (0.2)	1.0	0.04 (0.3) 0.08 (0.4) 0.27 (0.3)	Based on geomorphic evidence and the presence of gas fields, Haeussler *et al*. (2000) suggest that these anticlines are active. Given that these anticlines form a fairly continuous northwest trending zone, we have combined these structures to form one potential seismic source. Because this structure is near the source area of the 1933 M 6.9 Cook Inlet earthquake, we assign a preferred M max based on the magnitude of that earthquake. There are no measured slip rates available for this structure, therefore, we assign a slip rate based on the slip rate of the North Cook Inlet field (Haeussler *et al*., 2000).
Pitman Anticline	Full Rupture (1.0)	R	62	6.9 (0.2) 7.2 (0.6) 7.5 (0.2)	45 SE (0.3) 60 SE (0.4) 75 SE (0.3)	15 (0.2) 20 (0.6) 25 (0.2)	0.8	0.01 (0.3) 0.05 (0.4) 0.20 (0.3)	This source is included in the proposed 2023 revision (Bender *et al*., 2021a) of the NSHM and is based on the trace presented by Koehler *et al*. (2012) as part of the Alaska Quaternary fault and fold database, reported as simply <1.6 Ma. The northeast-southwest-striking fold is located several kilometers southeast of the Castle Mountain fault with the causative fault dipping southeast based on the Bender *et al*. (2021a) model. The dip is reported in the Bender *et al*. (2021a) source model as an assumed 45° based on the assumption the fault is

FAULT NAME	RUPTURE MODEL	STYLE[1]	MAXIMUM RUPTURE LENGTH[2] (km)	MAXIMUM MAGNITUDE[3] (Mw)	DIP[4] (degrees)	MAXIMUM SEISMOGENIC DEPTH[5] (km)	PROBABILITY OF ACTIVITY[6]	SLIP RATE[7] (mm/yr)	COMMENTS
									purely reverse. However, the strike of the fault nearly parallel to the Castle Mountain suggests the fault may accommodate a lateral component and have a potentially steeper dip.
Swanson River	Full Rupture	R	40	6.7 (0.2) 7.0 (0.6) 7.3 (0.2)	45 NW (0.3) 60 NW (0.4) 75 NW (0.3)	15 (0.2) 20 (0.6) 25 (0.2)	0.8	0.04 (0.3) 0.08 (0.4) 0.27 (0.3)	The Swanson River anticline represents an approximately 40-km-long structure located about 55 km southwest of the POA at its closest point. The fold is identified from seismic reflection data, aeromag surveys, and oil and gas wells (Haeussler *et al*., 2000; Haeussler and Saltus, 2011). Haeussler *et al*. (2000) indicate the fold deforms Pliocene or younger deposits and the Koehler *et al*. (2012) database assigns a Quaternary age for the structure (referencing Haeussler and Saltus, 2011), although we have found no definitive evidence in the literature of the structure deforming Quaternary age deposits. As such, we assign a P(a) of 0.8 given its inclusion in the Alaska Q fault database (Koehler *et al*., 2012).
Turnagain Arm	Full Rupture (1.0)	R	22	6.7 (0.2) 7.0 (0.6) 7.3 (0.2)	45 SE (0.3) 60 SE (0.4) 75 SE (0.3)	15 (0.2) 20 (0.6) 25 (0.2)	0.3	0.04 (0.3) 0.08 (0.4) 0.27 (0.3)	Little is known about this structure, which is the closest structure to the Port of Anchorage with possible Quaternary activity. Haeussler *et al*. (2000) identified this as a possible Quaternary structure capable of a M 6.4 earthquake. More recent work by Haeussler and Saltus (2011) indicates an "enigmatic" structure, and Haeussler and Saltus (2011) note that they "remain unconvinced as to the presence or nature of the structure at this location". We include it as a potential source given this uncertainty and close proximity to the POA, but assign a low P(a). Slip rate is based on Haeussler *et al*. (2000).
Wasilla St. No. 1 – Needham Anticline	Full Rupture (1.0)	R	45	6.7 (0.2) 7.0 (0.6) 7.3 (0.2)	45 NW (0.3) 60 NW (0.4) 75 NW (0.3)	15 (0.2) 20 (0.6) 25 (0.2)	0.8	0.01 (0.3) 0.05 (0.4) 0.20 (0.3)	This source is included in the proposed 2023 revision (Bender *et al*., 2021) of the NSHM and is based on the trace presented by Koehler *et al*. (2012) as part of the Alaska Quaternary fault and fold database, reported as simply <1.6 Ma. The northeast-southwest-striking fold is located approximately 6 to 20 km southeast of the Castle Mountain fault. The Wasilla source likely intersects the Pittman blind fault and/or the Castle Mountain fault if the dip is less than about 65°. The dip is reported in the Bender *et al*. (2021) source model is an assumed 45° based on the assumption the fault is purely reverse. The strike of the fault nearly parallel to the Castle Mountain at its eastern end suggests the fault may accommodate a lateral component and have a potentially steeper dip. The Wasilla anticline represents one of the closest sources to the POA.

Notes:

- Values in parentheses are epistemic weights.

1 N Normal; O Oblique; N/O Normal-Oblique; SS Strike-Slip; R Reverse (high-angle).

2 The maximum length of individual faults and fault zones are generally measured straight-line, end-to-end distance, excepting sources with significant changes in geometry along strike.

3 Preferred Mw values for faults are estimated using the average value of Wells and Coppersmith (1994) surface rupture length (all) and Leonard (2010) area relations. Values are estimated based on maximum surface rupture length.

4 Average fault dips and directions. The sources are assumed to be planes. For simplicity, the earthquake location model places the events randomly along an idealized, straight and continuous source zone.

5 Maximum seismogenic depths are used with fault dip angles and directions to distribute seismic moment and calculate source-to-site distances for ground motions. Maximum seismogenic depths are estimated on the basis of the depth that encompasses 95% of the seismicity in a given seismotectonic province, of interest to this study.

6 Probability of activity, P(a), is the likelihood that a fault or structural zone is a seismogenic source and is active within the modern stress field.

7 Rates of fault activity are average net slip rates (in mm/yr). Recurrence models are weighted (0.7) characteristic and (0.3) maximum magnitude for crustal fault sources.

* Given that most Cook Inlet sources are offshore, parameters such as activity, slip rate, and length are presented with large uncertainties. All Cook Inlet sources are assumed to be reverse faults in the model, with recognition that some *may* accommodate oblique shortening.

Table 2. Completeness Estimates and Number of Earthquakes in Each Magnitude Interval for the Modeled Seismic Source Zones

Magnitude Range	YB Zone		SABCI Zone		Slab Zone	
	Beginning of Usable Period (yr)	Earthquake Count	Beginning of Usable Period (yr)	Earthquake Count	Beginning of Usable Period (yr)	Earthquake Count
3.00 – 3.49	1970	31	1970	47	NA	NA
3.50 – 3.99	1970	28	1970	48	1970	901
4.00 – 4.49	1964	6	1964	25	1964	648
4.50 – 4.99	1964	7	1964	4	1964	249
5.00 – 5.49	1964	1	1964	0	1964	87
5.50 – 5.99	1932	0	1932	4	1955	59
6.00 – 6.49	1932	1	1932	1	1932	26
6.50 – 6.99	1910	0	1910	1	1898	14
≥ 7.00	1898	1	1898	2	1898	4

Table 3. Recurrence Parameters for the Crustal Source and Intraslab Zones

REALIZATION	*b*-VALUE	N(M>5)	WEIGHT
YB Zone			
1	0.73	0.05442	[0.125]
2	0.74	0.05642	[0.125]
3	0.79	0.04875	[0.125]
4	0.82	0.05053	[0.125]
5	0.66	0.09891	[0.125]
6	0.93	0.03369	[0.125]
7	0.84	0.04793	[0.125]
8	0.87	0.03800	[0.125]
SABCI Zone			
1	0.59	0.19007	[0.125]
2	0.62	0.17850	[0.125]
3	0.55	0.17494	[0.125]
4	0.52	0.22679	[0.125]
5	0.63	0.12653	[0.125]
6	0.65	0.11685	[0.125]
7	0.57	0.16327	[0.125]
8	0.60	0.17080	[0.125]
Slab Zone			
1	0.81	3.37588	[0.125]
2	0.80	3.09326	[0.125]
3	0.84	2.94113	[0.125]
4	0.82	3.14311	[0.125]
5	0.87	2.60756	[0.125]
6	0.84	2.82002	[0.125]
7	0.83	3.09693	[0.125]
8	0.81	3.07805	[0.125]

Table 4. Estimated Recurrence Intervals for the Seismic Source Zones

Realization	YB Zone		SABCI Zone		Slab Zone	
	M ≥ 5	M ≥ 6	M ≥ 5	M ≥ 6	M ≥ 5	M ≥ 6
1	18.4	117.2	5.3	25.8	0.30	2.0
2	17.7	116.0	5.6	28.8	0.32	2.1
3	20.5	147.5	5.7	26.2	0.34	2.5
4	19.8	151.1	4.4	19.1	0.32	2.2
5	10.1	56.3	7.9	41.9	0.38	3.0
6	29.7	283.8	8.6	47.1	0.35	2.6
7	20.9	163.9	6.1	28.8	0.32	2.3
8	26.3	221.9	5.9	29.2	0.32	2.2

Table 5. Seismic Source Parameters for Alaskan Subduction Zone

Fault Name	Probability of Activity	Rupture Model	Source	Preferred Mmax (M)	b-value	Dip (degrees)	Rupture Depth (km)	Recurrence Interval (Yrs)	Comments
Eastern section (Western Yakutat/Prince William Sound/Kodiak)	1.0	Unsegmented (0.7)	Kodiak + PWS/WY	9.1 (0.2) 9.2 (0.6) 9.3 (0.2)	1.00	3.0 N (0.2) 6.0 N (0.6) 9.0 N (0.2)	25 (0.2) 35 (0.6) 50 (0.2)	500 (0.2) 600 (0.6) 700 (0.2)	1964 Earthquake
		Segmented (0.3)	PWS/WY	8.8 (0.2) 9.0 (0.6) 9.2 (0.2)	1.00	3.0 N (0.2) 6.0 N (0.6) 9.0 N (0.2)	25 (0.2) 35 (0.6) 50 (0.2)	500 (0.2) 600 (0.6) 700 (0.2)	
			Kodiak	8.5 (0.2) 8.8 (0.6) 9.1 (0.2)	1.00	5.0 N (0.2) 7.0 N (0.6) 9.0 N (0.2)	30 (0.5) 50 (0.5)	400 (0.2) 500 (0.6) 600 (0.2)	Ruptured independently at least 4 times in past 2000 years. One to two times ruptured in the same time period with PWS.
Semidi	1.0	Unsegmented (1.0)		7.9 (0.2) 8.2 (0.6) 8.5 (0.2)	0.71	6 N (0.5) 10 N (0.5)	20 (0.2) 24 (0.6) 28 (0.2)	180 (0.2) 225 (0.6) 270 (0.2)	Ruptured in 1788 and 1938. RI 180-270 years.

Table 6. Time-Dependent Equivalent Poisson Recurrence Intervals

Source	Poisson Recurrence Interval (yr)	*Poisson Recurrence Interval Weight*	COV	*COV Weight*	BPT Probability	Equivalent Poisson Rate (1/yr)	Equivalent Poisson Recurrence Interval (yr)	*Equivalent Poisson Recurrence Interval Weight*
Kodiak+PWS/WY	500	*0.2*	0.3	*0.5*	1.65E-08	3.29E-10	> 100,000,000	*0.1*
	600	*0.6*	0.3	*0.5*	1.09E-10	2.17E-12	> 100,000,000	*0.3*
	700	*0.2*	0.3	*0.5*	6.50E-13	1.30E-14	> 100,000,000	*0.1*
	500	*0.2*	0.5	*0.4*	6.33E-04	1.27E-05	78,989	*0.08*
	600	*0.6*	0.5	*0.4*	9.80E-05	1.96E-06	509,954	*0.24*
	700	*0.2*	0.5	*0.4*	1.48E-05	2.96E-07	3,382,171	*0.08*
	500	*0.2*	0.7	*0.1*	1.34E-02	2.71E-04	3,695	*0.02*
	600	*0.6*	0.7	*0.1*	5.03E-03	1.01E-04	9,908	*0.06*
	700	*0.2*	0.7	*0.1*	1.86E-03	3.72E-05	26,857	*0.02*
Kodiak	400	*0.2*	0.3	*0.5*	2.33E-06	4.66E-08	21,445,466	*0.1*
	500	*0.6*	0.3	*0.5*	1.65E-08	3.29E-10	> 100,000,000	*0.3*
	600	*0.2*	0.3	*0.5*	1.09E-10	2.17E-12	> 100,000,000	*0.1*
	400	*0.2*	0.5	*0.4*	4.04E-03	8.10E-05	12,339	*0.08*
	500	*0.6*	0.5	*0.4*	6.33E-04	1.27E-05	78,989	*0.24*
	600	*0.2*	0.5	*0.4*	9.80E-05	1.96E-06	509,954	*0.08*
	400	*0.2*	0.7	*0.1*	3.57E-02	7.27E-04	1,375	*0.02*
	500	*0.6*	0.7	*0.1*	1.34E-02	2.71E-04	3,695	*0.06*
	600	*0.2*	0.7	*0.1*	5.03E-03	1.01E-04	9,908	*0.02*

Note: Recurrence intervals for Segmented PWS/WY are the same as those for Kodiak+PWS/WY.

Table 7. Probabilistic Ground Motions at Selected Return Periods

Return period (years)	PGA (g) Mean [5th, 95th percentiles]	1.0 Sec SA (g) Mean [5th, 95th percentiles]
72	0.201 [0.099,0.340]	0.115 [0.067,0.176]
475	0.563 [0.257,0.967]	0.320 [0.174,0.490]
975	0.791 [0.350,1.349]	0.449 [0.237,0.686]
2,475	1.187 [0.504,2.000]	0.671 [0.344,1.019]

Table 8. Controlling Earthquakes

Period		Return Period (Years)			
		72	475	975	2,475
PGA	M*	7.1	7.1	7.1	7.1
	D*	92.5	67.5	57.5	57.5
	M-bar	6.7	6.9	6.9	7.0
	D-bar	90.6	76.7	72.8	68.5
0.2 sec	M*	7.1	7.1	7.1	7.1
	D*	92.5	67.5	57.5	57.5
	M-bar	6.7	6.9	6.9	7.0
	D-bar	92.3	78.2	74.2	69.7
1.0 sec	M*	7.1	7.1	7.1	9.3
	D*	37.5	37.5	57.5	32.5
	M-bar	6.9	7.1	7.1	7.1
	D-bar	105.8	87.2	81.7	75.6
1.5 sec	M*	7.1	7.1	7.1	9.3
	D*	37.5	37.5	37.5	32.5
	M-bar	7.0	7.1	7.1	7.1
	D-bar	107.4	87.2	81.2	74.5
2.0 sec	M*	7.1	7.1	7.1	9.3
	D*	37.5	37.5	37.5	32.5
	M-bar	7.0	7.1	7.2	7.2
	D-bar	109.6	88.7	82.3	75.2

Table 9. Horizontal UHS for Vs30 760 m/sec

Period (sec)	Horizontal Spectral Acceleration (g)			
	72-Year Return Period	475-Year Return Period	975-Year Return Period	2,475-Year Return Period
0.01	0.201	0.563	0.791	1.187
0.02	0.211	0.597	0.841	1.266
0.03	0.236	0.672	0.949	1.428
0.05	0.308	0.881	1.247	1.895
0.075	0.388	1.109	1.573	2.398
0.1	0.440	1.259	1.784	2.715
0.15	0.472	1.361	1.929	2.927
0.2	0.456	1.313	1.864	2.835
0.25	0.430	1.232	1.749	2.664
0.3	0.387	1.106	1.568	2.385
0.4	0.318	0.908	1.283	1.943
0.5	0.265	0.750	1.058	1.595
0.75	0.168	0.473	0.665	0.997
1.0	0.115	0.320	0.449	0.671
1.5	0.065	0.178	0.249	0.372
2.0	0.044	0.121	0.169	0.255
3.0	0.022	0.062	0.087	0.130
4.0	0.014	0.038	0.053	0.080
5.0	0.0095	0.027	0.038	0.057
7.5	0.0041	0.014	0.020	0.030
10.0	0.0023	0.0081	0.012	0.019

Table 10. Comparison with the 2007 USGS National Seismic Hazard Map

Period (sec)	Study	Horizontal Spectral Acceleration (g)			
		72-Year Return Period	475-Year Return Period	975-Year Return Period	2,475-Year Return Period
PGA	USGS 2007	0.211	0.435	0.543	0.691
	This Study	0.201	0.563	0.791	1.187
	Comparison	-5%	29%	46%	72%
1.0	USGS 2007	0.148	0.345	0.454	0.615
	This Study	0.115	0.320	0.449	0.671
	Comparison	-22%	-7%	-1%	9%

Note: Comparison shows percent change from USGS 2007 values to site-specific values.

Table 11. Inputs for DSHA

Input parameter	Input parameter Definition	Intraslab	Megathrust
M	Moment magnitude	7.6	9.2
R_{RUP}	Closest distance to coseismic rupture (km)	25	31
R_{JB}	Closest distance to surface projection of coseismic rupture (km)	3	0
R_X	Horizontal distance from top of rupture measured perpendicular to fault strike (km)	3	291
R_{y0}	The horizontal distance off the end of the rupture measured parallel to strike (km)	0	0
U	Unspecified-mechanism factor: 1 for unspecified; 0 otherwise	0	0
F_{RV}	Reverse-faulting factor: 0 for strike slip, normal, normal-oblique; 1 for reverse, reverse-oblique and thrust	1	1
F_N	Normal-faulting factor: 0 for strike slip, reverse, reverse-oblique, thrust and normal-oblique; 1 for normal	0	0
F_{HW}	Hanging-wall factor: 1 for site on down-dip side of top of rupture; 0 otherwise	0	0
Z_{TOR}	Depth to top of coseismic rupture (km)	24	7
Dip	Average dip of rupture plane (degrees)	90	90
V_{S30}	The average shear-wave velocity (m/s) over a subsurface depth of 30 m	760	760
Z_{HYP}	Hypocentral depth from the earthquake	38	29
$Z_{1.0}$	Depth to Vs=1 km/sec (km)	0.5	0.5
$Z_{2.5}$	Depth to Vs=2.5 km/sec (km)	1.0	1.0
W	Fault rupture width (km)	27	400
$Region$	Specific Regions considered in the models	Global	Global

Table 12. Median and 84th Percentile Deterministic Horizontal Response Spectra

Period (sec)	Intraslab		Megathrust		Envelope	
	Median (g)	84th (g)	Median (g)	84th (g)	Median (g)	84th (g)
0.01	0.729	1.562	0.437	0.937	0.729	1.562
0.02	0.771	1.656	0.456	0.980	0.771	1.656
0.03	0.847	1.832	0.502	1.086	0.847	1.832
0.05	1.028	2.262	0.599	1.321	1.028	2.262
0.075	1.212	2.704	0.696	1.559	1.212	2.704
0.1	1.384	3.093	0.791	1.773	1.384	3.093
0.15	1.591	3.536	0.920	2.047	1.591	3.536
0.2	1.650	3.669	0.953	2.119	1.650	3.669
0.3	1.412	3.107	0.860	1.893	1.412	3.107
0.4	1.184	2.589	0.754	1.648	1.184	2.589
0.5	0.987	2.148	0.657	1.429	0.987	2.148
0.75	0.633	1.378	0.472	1.029	0.633	1.378
1	0.440	0.955	0.346	0.752	0.440	0.955
1.5	0.262	0.567	0.220	0.475	0.262	0.567
2	0.179	0.385	0.160	0.345	0.179	0.385
3	0.095	0.204	0.090	0.192	0.095	0.204
4	0.058	0.122	0.062	0.130	0.062	0.130
5	0.041	0.085	0.049	0.101	0.049	0.101
7.5	0.020	0.039	0.030	0.060	0.030	0.060
10	0.011	0.022	0.020	0.040	0.020	0.040

Table 13. CMS Conditioned at 0.2 and 2.0 Sec for the 975-Year Return Period

PERIOD (SEC)	CMS (g)	
	T = 0.2 SEC	T = 2.0 SEC
0.01	0.791	0.483
0.02	0.832	0.504
0.03	0.913	0.554
0.05	1.087	0.659
0.075	1.281	0.769
0.1	1.447	0.879
0.15	1.755	1.031
0.2	1.864	1.076
0.3	1.534	0.963
0.4	1.269	0.831
0.5	1.058	0.719
0.75	0.665	0.513
1	0.449	0.370
1.5	0.249	0.232
2	0.169	0.169
3	0.087	0.087
4	0.053	0.053
5	0.038	0.038
7.5	0.020	0.020
10	0.012	0.012

Table 14. Vertical Spectra for Vs30 760 m/sec

Period (sec)	Vertical Spectral Acceleration (g)			
	72-Year Return Period	475-Year Return Period	975-Year Return Period	2,475-Year Return Period
0.01	0.086	0.259	0.377	0.574
0.02	0.090	0.275	0.401	0.614
0.03	0.102	0.320	0.474	0.731
0.05	0.141	0.473	0.724	1.151
0.075	0.202	0.683	1.042	1.686
0.1	0.227	0.744	1.121	1.805
0.15	0.221	0.674	0.984	1.536
0.2	0.213	0.608	0.860	1.308
0.25	0.184	0.522	0.738	1.124
0.3	0.162	0.455	0.642	0.975
0.4	0.134	0.373	0.520	0.790
0.5	0.112	0.307	0.427	0.642
0.75	0.074	0.202	0.278	0.420
1.0	0.055	0.149	0.206	0.308
1.5	0.034	0.091	0.126	0.188
2.0	0.024	0.064	0.089	0.134
3.0	0.013	0.036	0.050	0.075
4.0	0.008	0.023	0.032	0.048
5.0	0.006	0.017	0.024	0.036
7.5	0.002	0.008	0.011	0.017
10.0	0.001	0.004	0.006	0.010

Figures

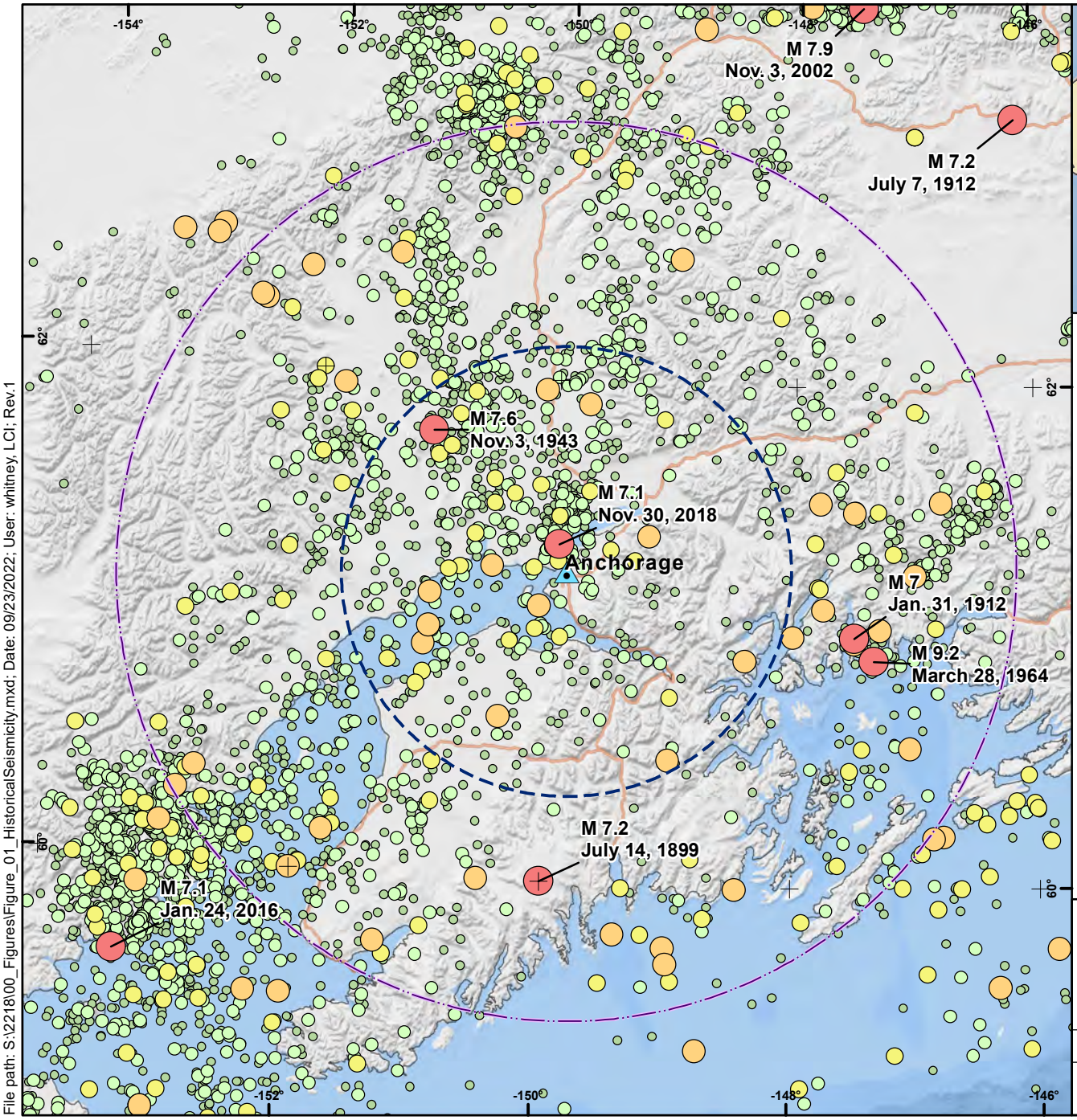

EXPLANATION

- Site location
- 100 km buffer
- 200 km buffer
- Fault, from Plafker (1994) and USGS (2012; 2021; 2023)

Seismicity [M]

- 3.0 - 3.9
- 4.0 - 4.9
- 5.0 - 5.9
- 6.0 - 6.9
- ≥ 7.0

Sources:
Seismicity catalog from USGS (2021)

N W E S

0 25 50 mi

0 50 100 km

Map projection and scale: NAD 1983 UTM Zone 6N, 1:2,700,000

Historical Seismicity in the Site Region, 1882 - 2020

PORT OF ALASKA

LCI Lettis Consultants International, Inc. | Figure 1

File path: S:\2218\00_Figures\Figure_01_HistoricalSeismicity.mxd; Date: 09/23/2022; User: whitney, LCI; Rev.1

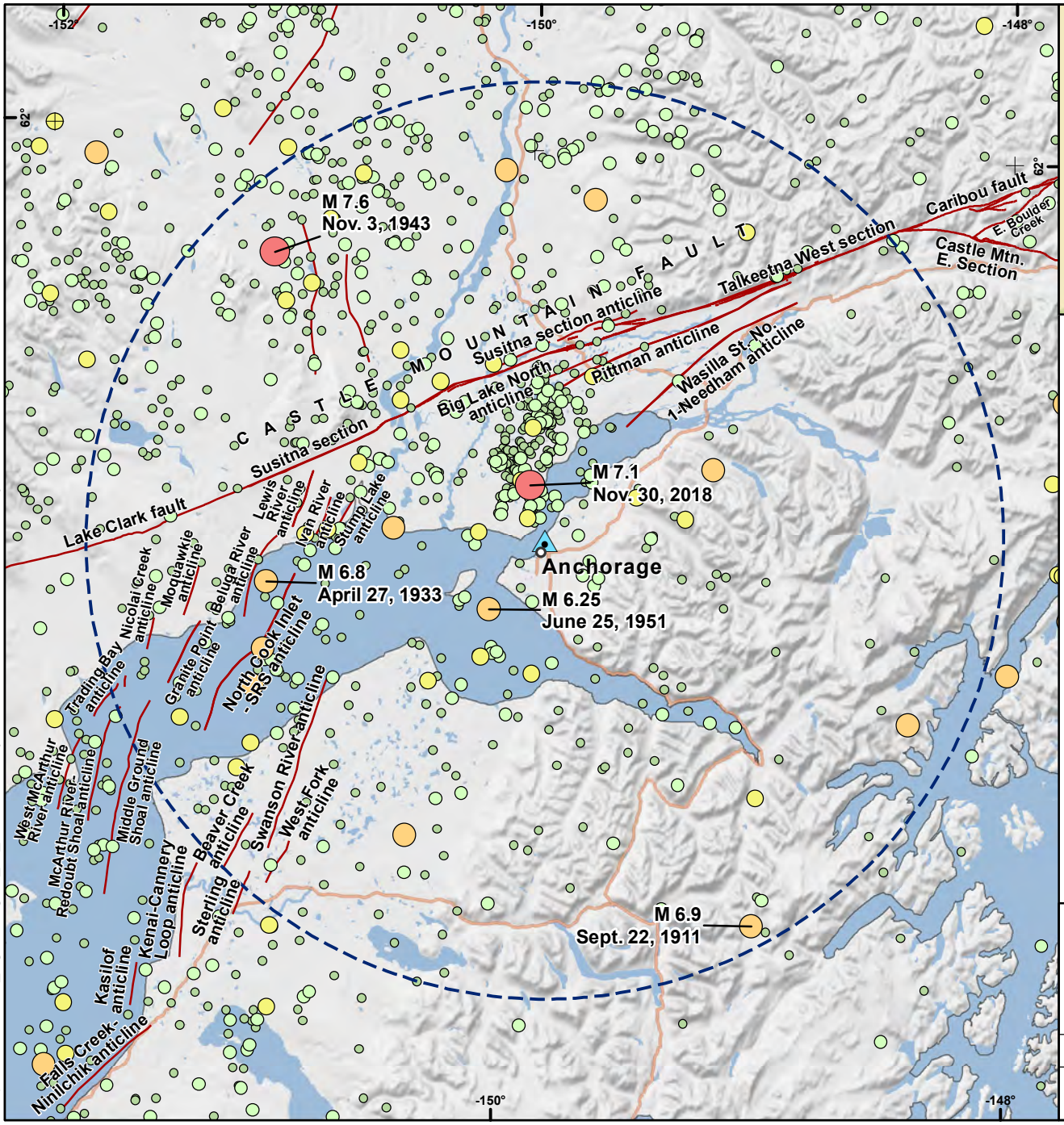

EXPLANATION

- Site location
- 100 km buffer
- 200 km buffer
- Fault, from Bender (2021a, b) and Koehler (2012)

Seismicity [M]

- 3.0 - 3.9
- 4.0 - 4.9
- 5.0 - 5.9
- 6.0 - 6.9
- ≥ 7.0

Sources:
Seismicity catalog from USGS (2021)

N W E S

0 10 20 mi

0 25 50 km

Map projection and scale: NAD 1983 UTM Zone 6N, 1:1,330,000

Historical Seismicity within 100 km of the Site, 1882 - 2020

PORT OF ALASKA

LCI Lettis Consultants International, Inc. | Figure **2**

File path: S:\2218\00_Figures\Figure_02_LocalSeismicity.mxd; Date: 09/23/2022; User: whitney, LCI; Rev.1

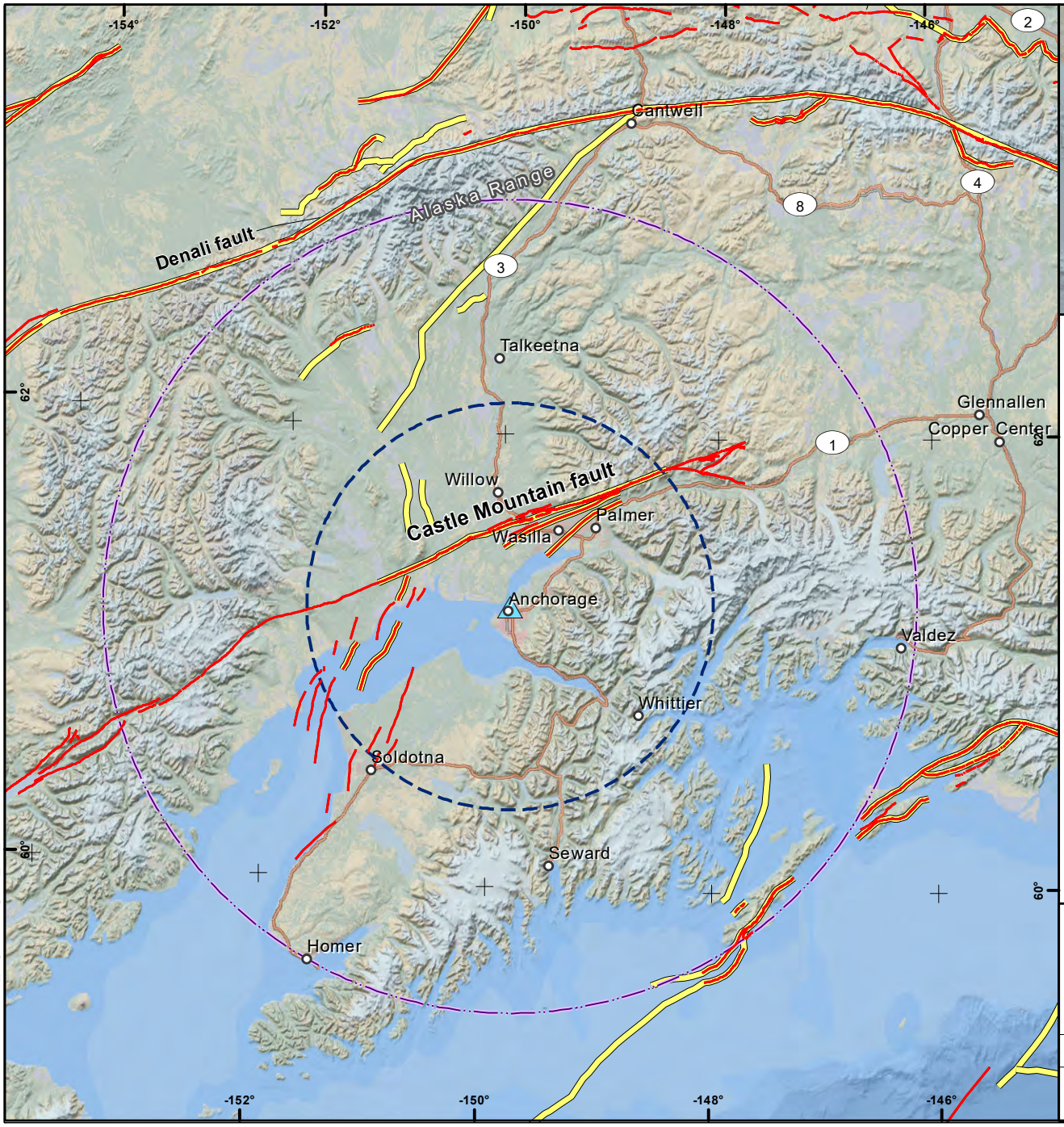

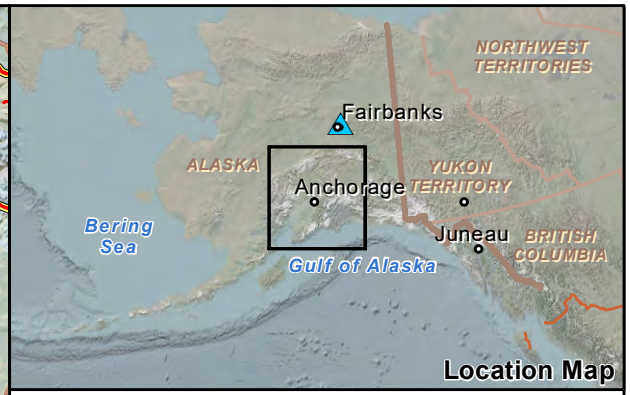

EXPLANATION

- Site location
- 100 km buffer
- 200 km buffer
- Fault, from Koehler (2012)
- Fault, from Bender (2021a)

Sources:

- Basemap compiled from NLCD (2020), GEBCO (2020), and ESRI.
- Quaternary fault databases shown:
  1. 2023 National Seismic Hazard Model (NSHM) (Bender et al. 2021a)
  2. Quaternary Fault and Folds in Alaska (Koehler et al. 2012)

N W E S

0 20 40 mi

0 40 80 km

Map projection and scale: NAD 1983 UTM Zone 6N, 1:3,000,000

Quaternary Faulting in Southcentral Alaska

PORT OF ALASKA

LCI Lettis Consultants International, Inc. | Figure 3

File path: S:\2218\00_Figures\Figure_03_Qfaults.mxd; Date: 11/14/2022; User: Brian, LCI; Rev.1

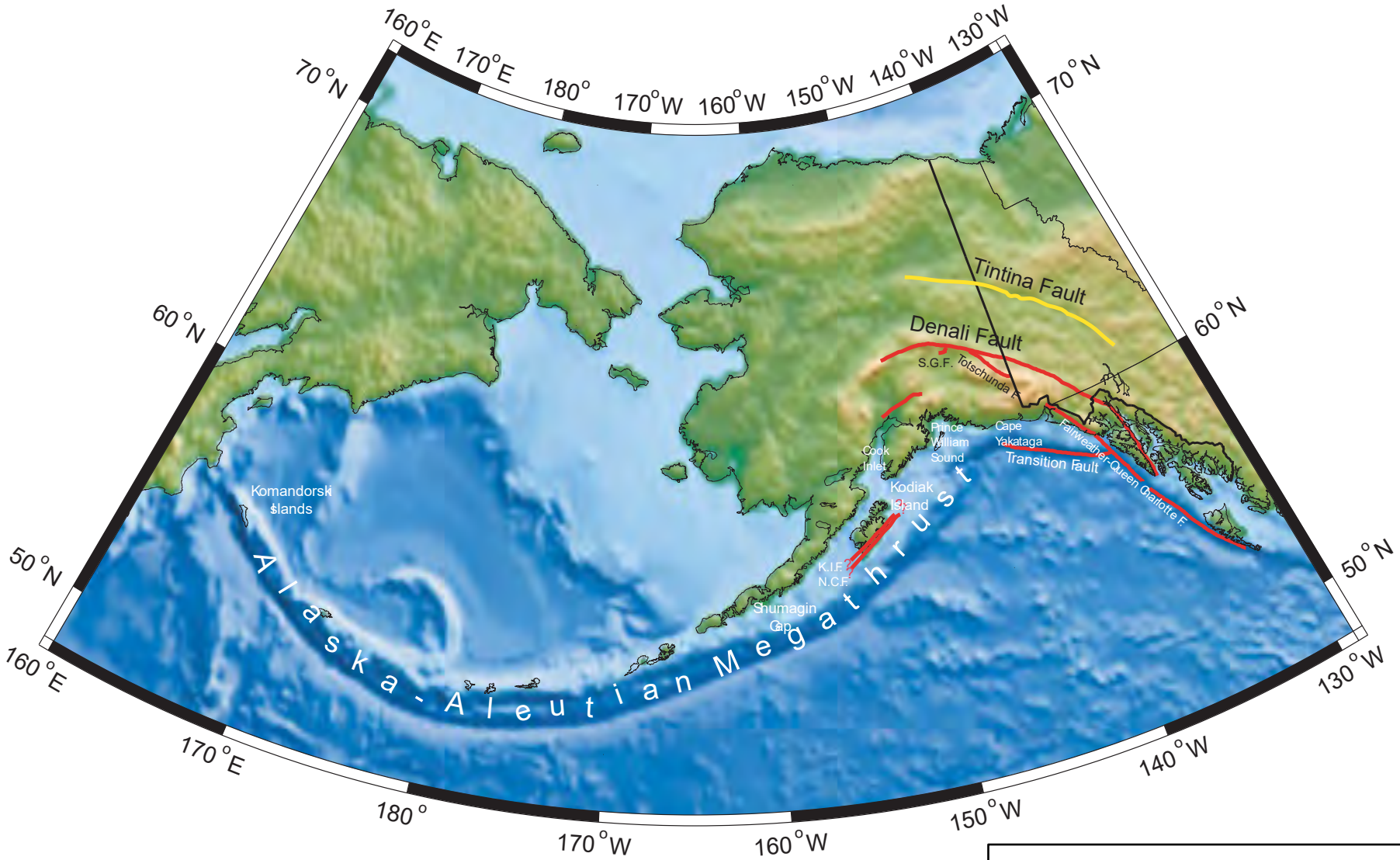

Source: Wesson et al. (2007)

Alaska-Aleutian Subduction Zone and Selected Crustal Faults

PORT OF ALASKA

Lettis Consultants International, Inc.

Figure **4**

File path: S:\2218\00_Figures\Figure_4_Schematic_Map.ai; Date: 09/21/2022; User: wka, LCI

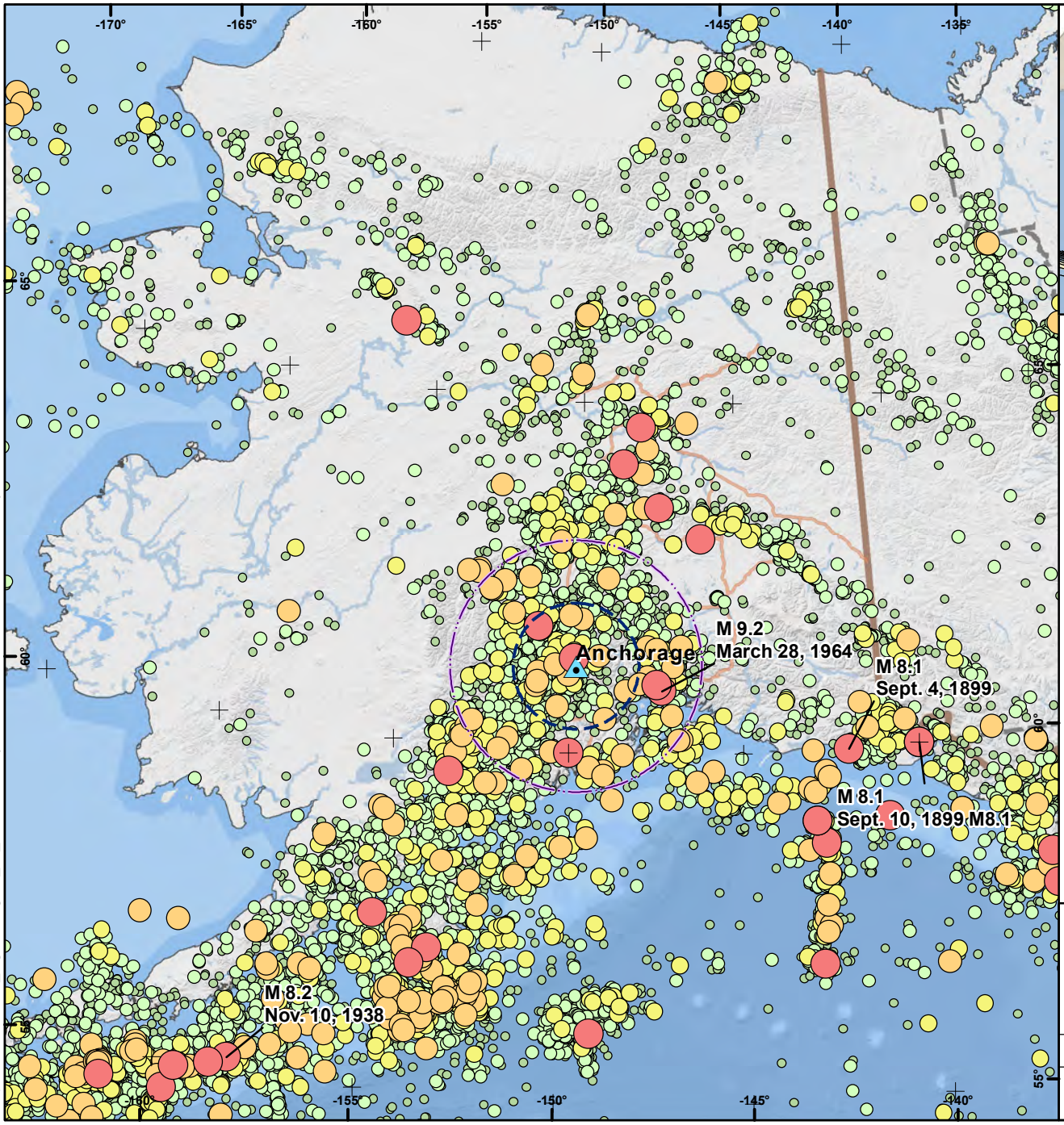

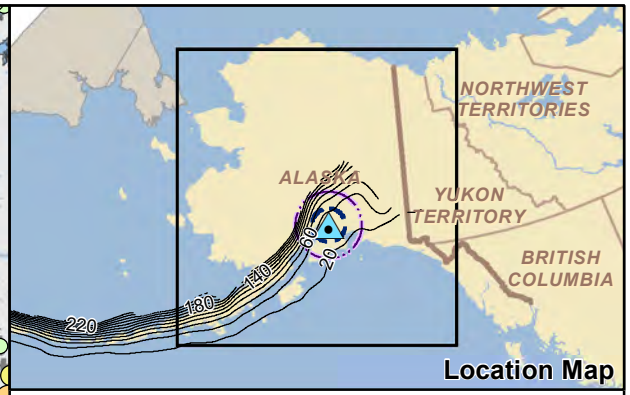

EXPLANATION

- Site location
- 100 km buffer
- 200 km buffer
- Slab depth contours

Seismicity [M]

- 3.0 - 3.9
- 4.0 - 4.9
- 5.0 - 5.9
- 6.0 - 6.9
- ≥ 7.0

Sources:
Seismicity catalog from USGS (2021)

N W E S

0 100 200 mi
0 100 200 km

Map projection and scale: NAD 1983 UTM Zone 6N, 1:9,692,227

Historical Seismicity and the Alaska-Aleutian Wadati-Benioff Zone

PORT OF ALASKA

LCI Lettis Consultants International, Inc. | Figure **5**

File path: S:\2218\00_Figures\Figure_05_SlabSeismicity.mxd; Date: 09/23/2022; User: whitney, LCI; Rev.1

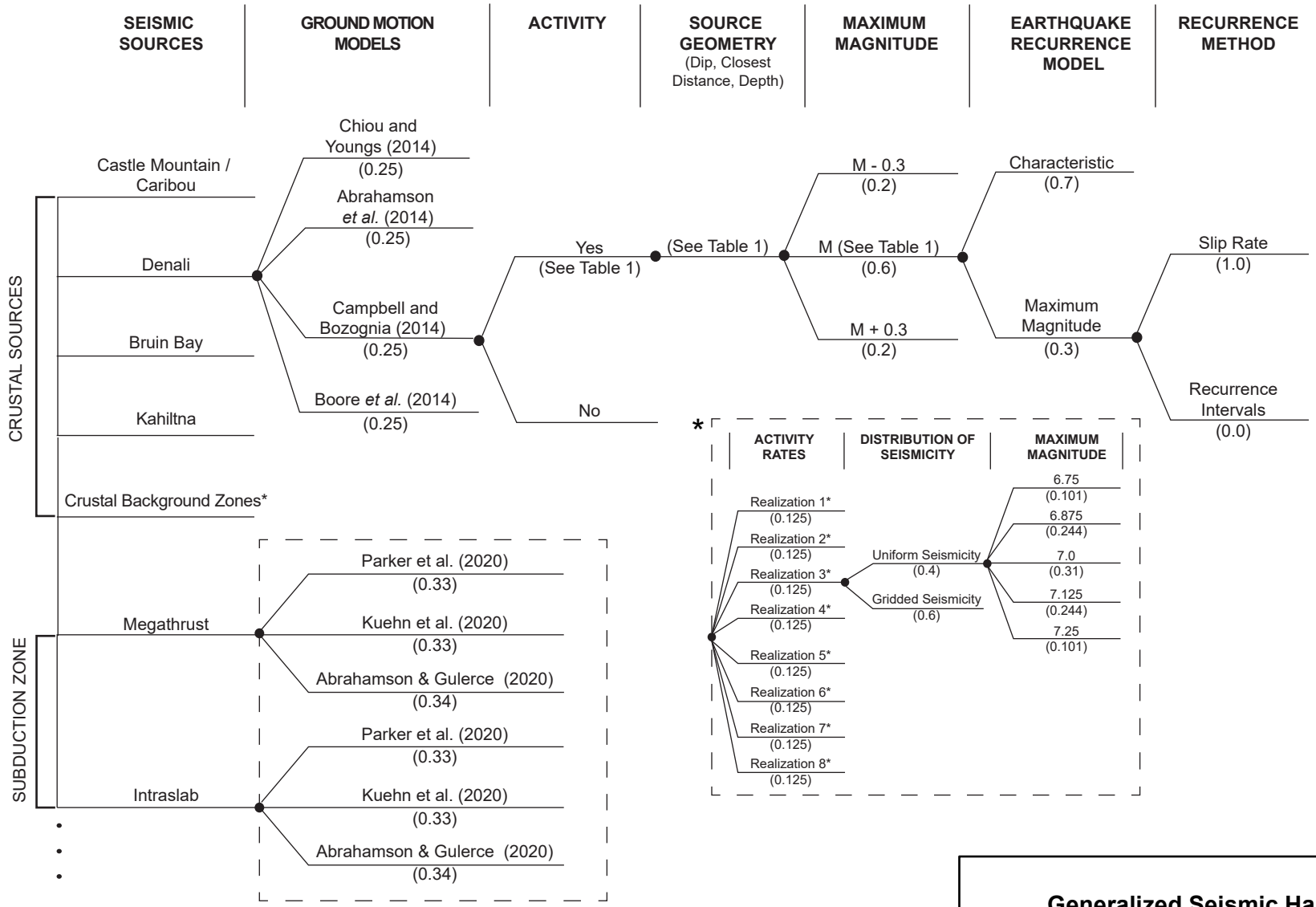

Notes:

1. Additional epistemic uncertainty added to NGA-West2 GMMs using Al Atik and Youngs (2014).
2. Global median NGA-Sub GMMs are used and additional epistemic uncertainty was added following the approach of Al Atik and Youngs (2014).

Generalized Seismic Hazard Model Logic Tree

PORT OF ALASKA

Lettis Consultants International, Inc.

Figure **6**

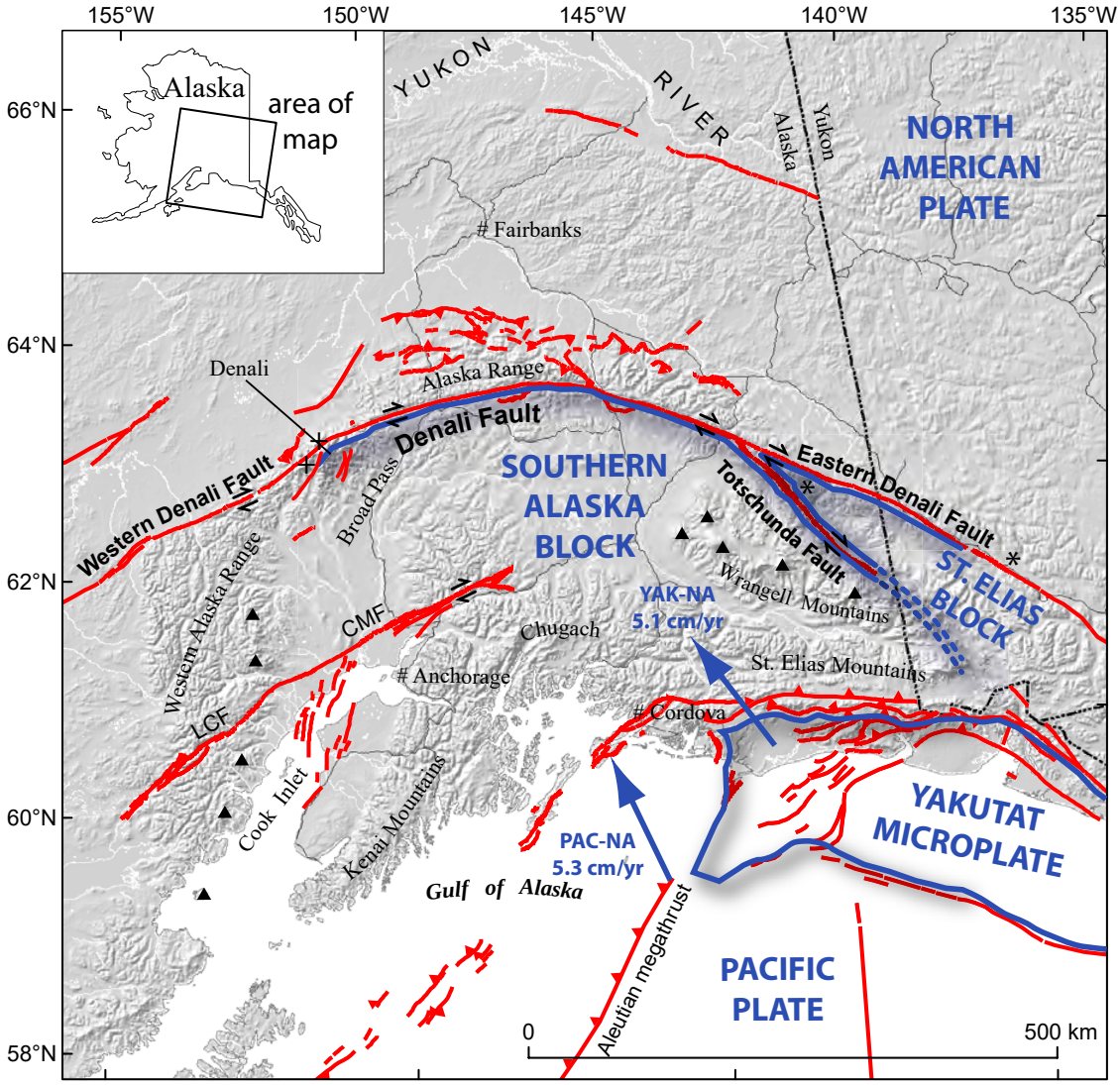

EXPLANATION

- Active faults
- + 38 Ma offset pluton piercing point locations interpreted by Reed and Lanphere (1974)
- ▲ Active volcano
- * Locations of Early(?) Cretaceous piercing points interpreted by Lowey (1998)
- Tectonic plate boundary

Abbreviations
LCF: Lake Clark fault
CMF: Castle Mountain fault

Tectonic Setting from Haeussler et al. 2017

PORT OF ALASKA

Lettis Consultants International, Inc. | Figure 7

File path: File path: S:\2218\00_Figures\Figure_07.ai; Date: 09/21/2022; User: wka, LCI

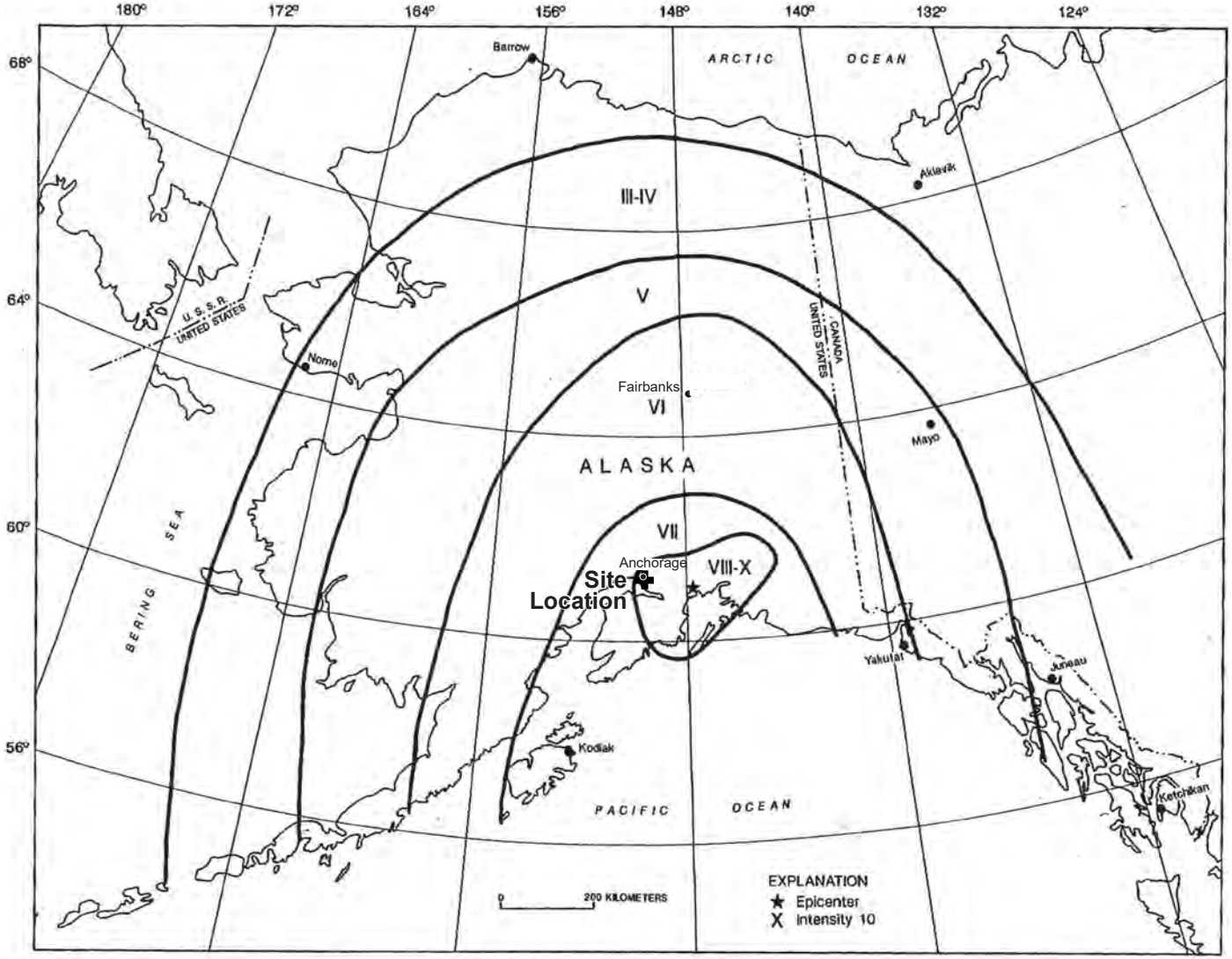

Source: Stover and Coffman (1993)

Isoseismal Map of the 28 March 1964 M 9.2 Great Alaska Earthquake

PORT OF ALASKA

Lettis Consultants International, Inc.

Figure **8**

File path: S:\2218\00_Figures\Figure_8.ai; Date: 10/11/2022; User: wka, LCI

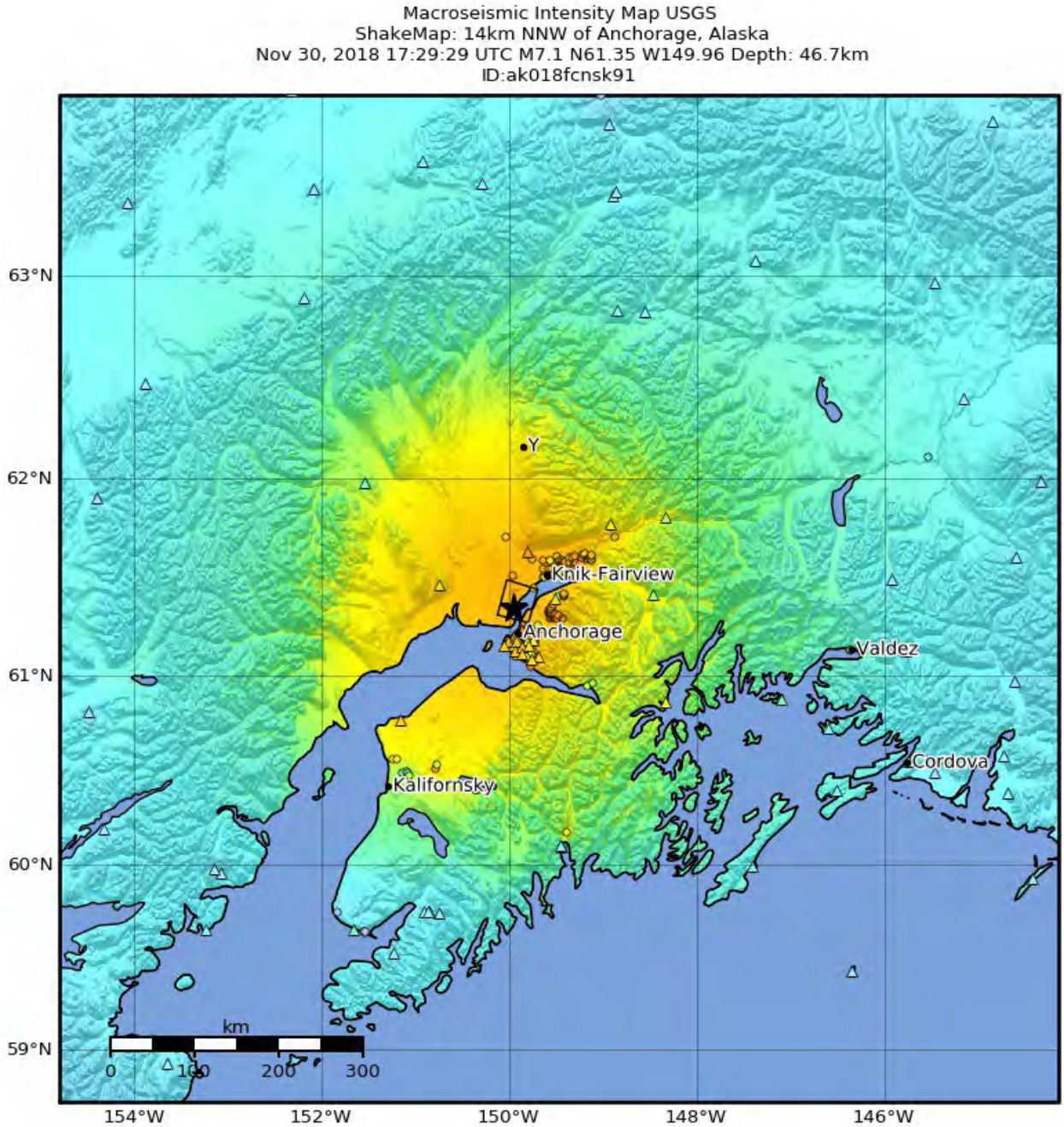

SHAKING	Not felt	Weak	Light	Moderate	Strong	Very strong	Severe	Violent	Extreme
DAMAGE	None	None	None	Very light	Light	Moderate	Moderate/heavy	Heavy	Very heavy
PGA(%g)	<0.0464	0.297	2.76	6.2	11.5	21.5	40.1	74.7	>139
PGV(cm/s)	<0.0215	0.135	1.41	4.65	9.64	20	41.4	85.8	>178
INTENSITY	I	II-III	IV	V	VI	VII	VIII	IX	X+

Scale based on Worden et al. (2012)

Version 1: Processed 2020-06-05T15:34:43Z

△ Seismic Instrument ○ Reported Intensity ★ Epicenter ▭ Rupture

2018 M 7.1 Anchorage Earthquake ShakeMap

PORT OF ALASKA

Lettis Consultants International, Inc.

Figure **9**

File path: File path: S:\2218\00_Figures\Figure_09.ai; Date: 10/11/2022; User: wka, LCI

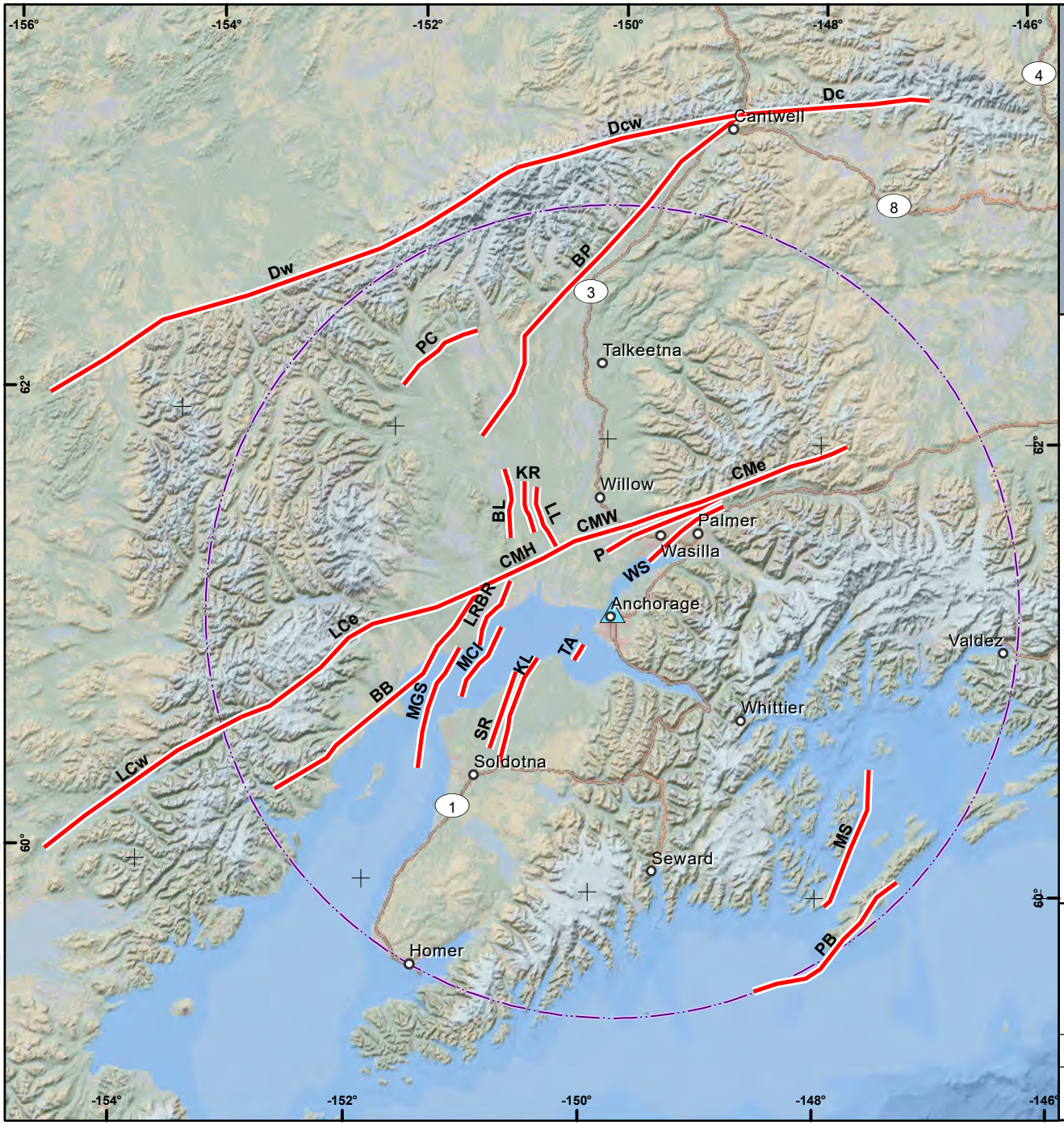

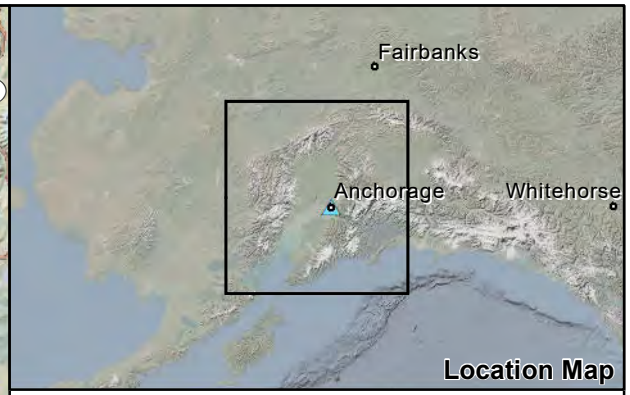

EXPLANATION

Site location

200 km buffer

Fault source

Abbreviations:

BB = Bruin Bay
BL = Bulchitna Lake
BP = Broad Pass thrust
CMe = Castle Mountain east - Caribou
CMH = Castle Mountain Holocene
CMW = Castle Mountain west
Dc = Denali center
Dcw = Denali center west
Dw = Denali west
KL = Kenai Lowlands
KR = Kahiltna River
LCe = Lake Clark eastern
LCw = Lake Clark western
LL = Leech Lake
LRBR = Lewis River - Beluga River
MCI = North Cook Inlet - SRS Anticline
MGS = Middle Ground Shoal - Granite Point
MS = Montague Strait
P = Pitman
PB = Patton Bay
PC = Pass Creek
SR = Swanson River
TA = Turnagain Arm
WS = Wasilla St. No. 1 - Needham

Source:
• Basemap compiled from NLCD (2020), GEBCO (2020), and ESRI.

N W E S

0 20 40 mi
0 40 80 km

Map projection and scale: NAD 1983 UTM Zone 6N, 1:3,000,000

Crustal Fault Sources Included in the PSHA

PORT OF ALASKA

LCI Lettis Consultants International, Inc. | Figure **10**

File path: S:\2218\00_Figures\Figure_10_CrustalSources.mxd; Date: 10/11/2022; User: whitney, LCI; Rev.1

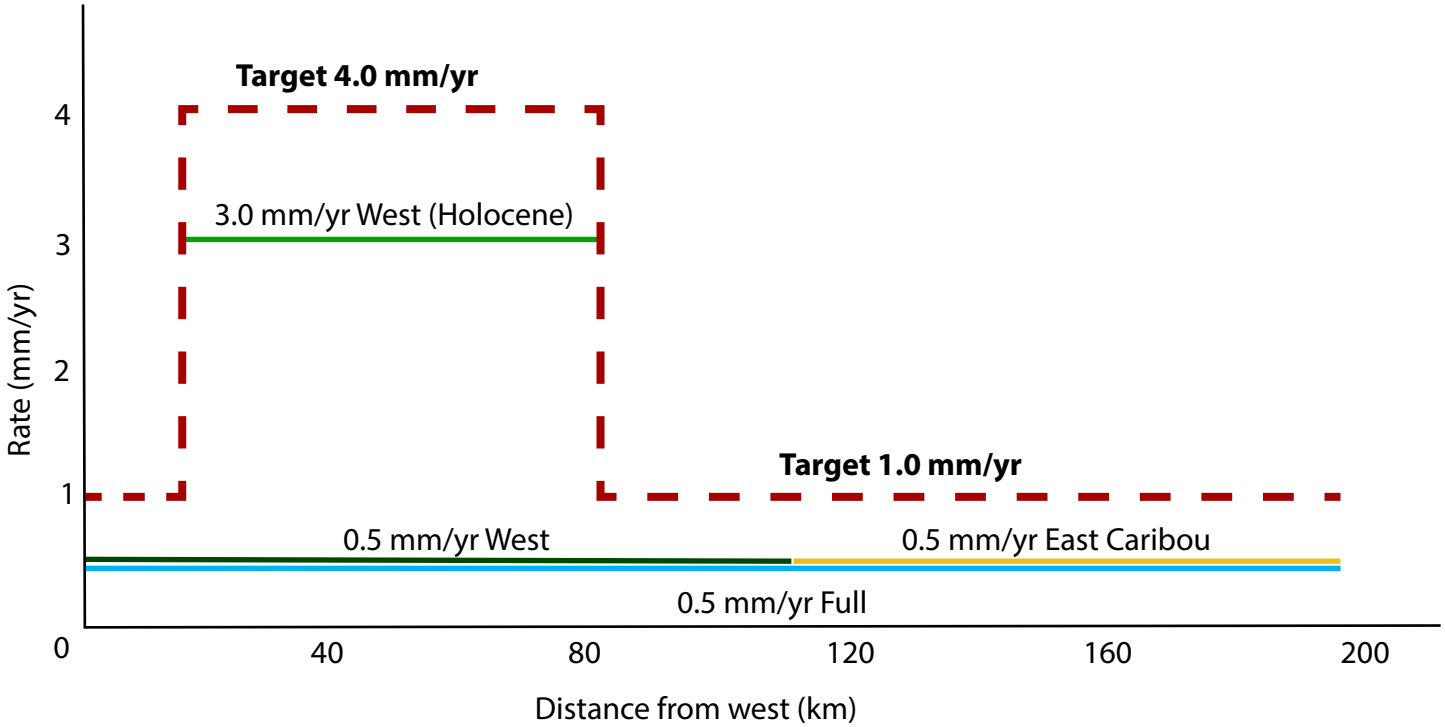

Layered Model for the Castle Mountain Fault

PORT OF ALASKA

Lettis Consultants International, Inc.

Figure **11**

S:\2218\00_Figures\Figure_11.ai; Date: 10/11/2022; User: wka, LCI

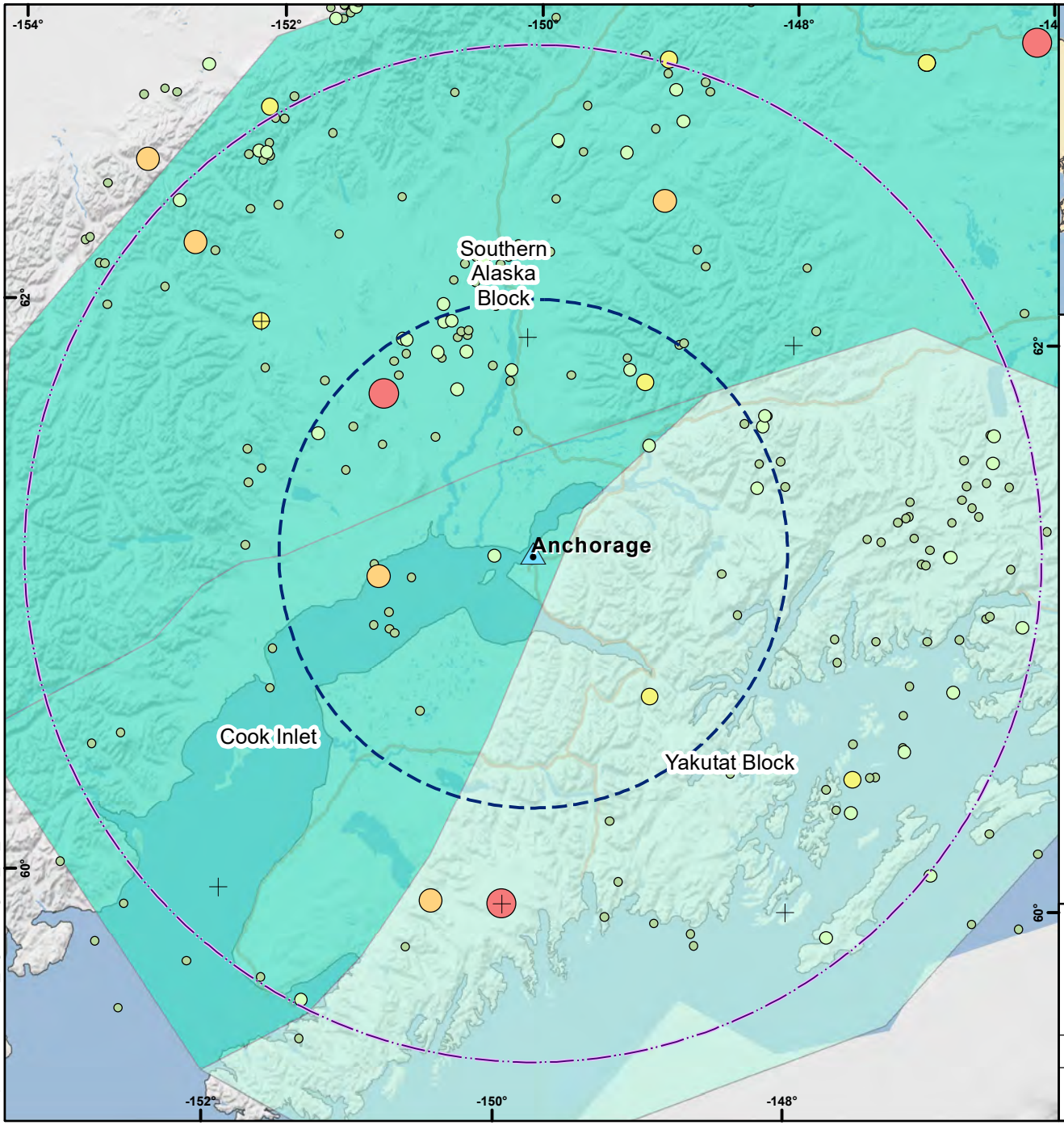

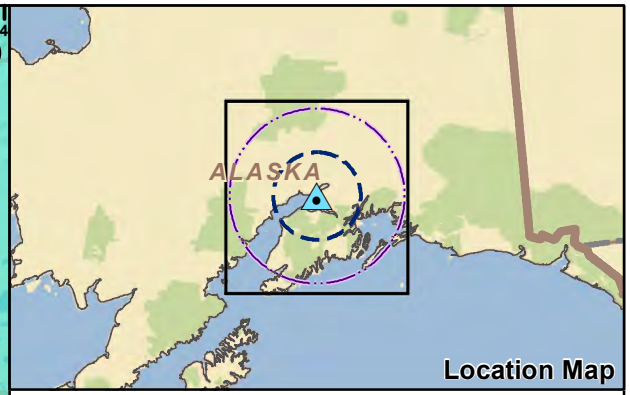

EXPLANATION

- Site location
- 100 km buffer
- 200 km buffer

Seismicity [M]

- 3.0 - 3.9
- 4.0 - 4.9
- 5.0 - 5.9
- 6.0 - 6.9
- ≥ 7.0

Source Zones

- Southern Alaska Block and Cook Inlet
- Yakutat Block

Sources:
Seismicity catalog from USGS (2021)

N W E S

0 30 60 mi
0 40 80 km

Map projection and scale: NAD 1983 UTM Zone 6N, 1:2,400,000

Seismic Source Zones and Declustered Crustal Catalog, 1882 - 2020

PORT OF ALASKA

LCI Lettis Consultants International, Inc. | Figure **12**

File path: S:\2218\00_Figures\Figure_12_SourceZones.mxd; Date: 10/07/2022; User: nora, LCI; Rev.1

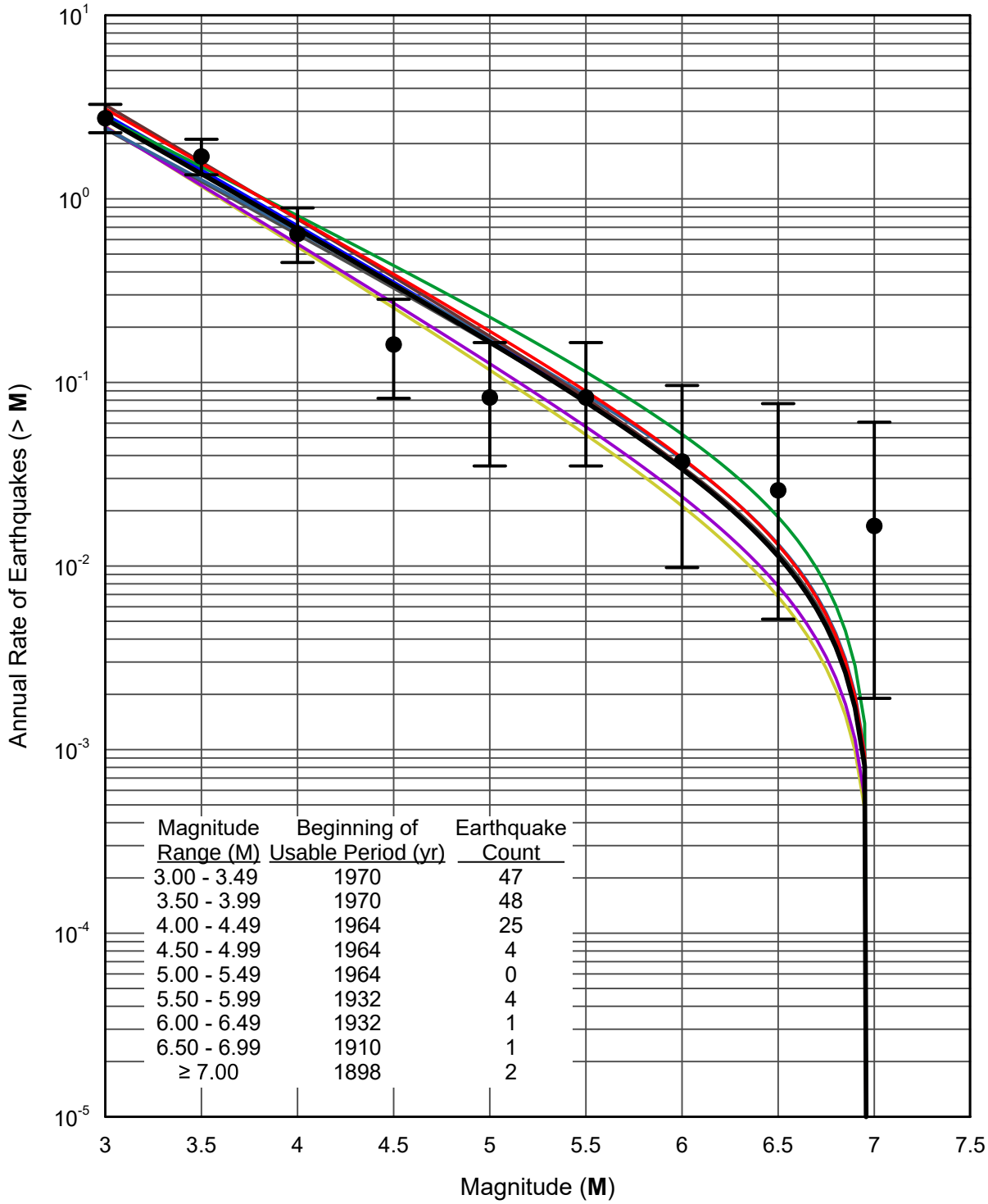

EXPLANATION

● Cumulative earthquake rate

ABSMOOTH Realization

1, 2, 3, 4, 5, 6, 7, 8, Mean

Note: Error bars on cumulative earthquake rate represent two standard deviations.

Cumulative Magnitude-Recurrence Curves for the Southern Alaska Block and Cook Inlet Source Zone for M_{MAX} 7.0

PORT OF ALASKA

Lettis Consultants International, Inc. | Figure **13**

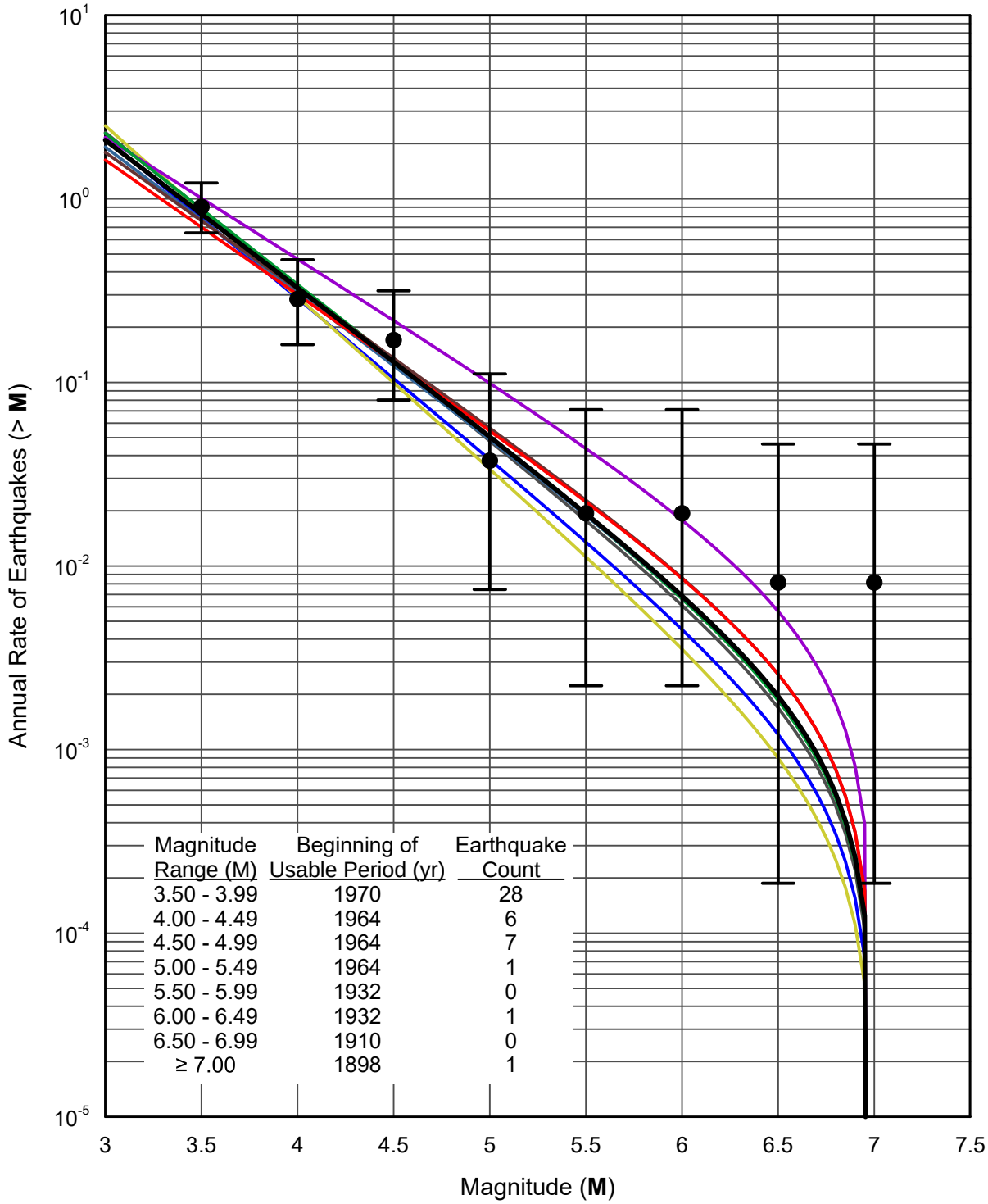

EXPLANATION

● Cumulative earthquake rate

ABSMOOTH Realization

1, 2, 3, 4, 5, 6, 7, 8, Mean

Note: Error bars on cumulative earthquake rate represent two standard deviations.

Cumulative Magnitude-Recurrence Curves for the Yakutat Block Source Zone for M_{MAX} 7.0

PORT OF ALASKA

Lettis Consultants International, Inc. Figure **14**

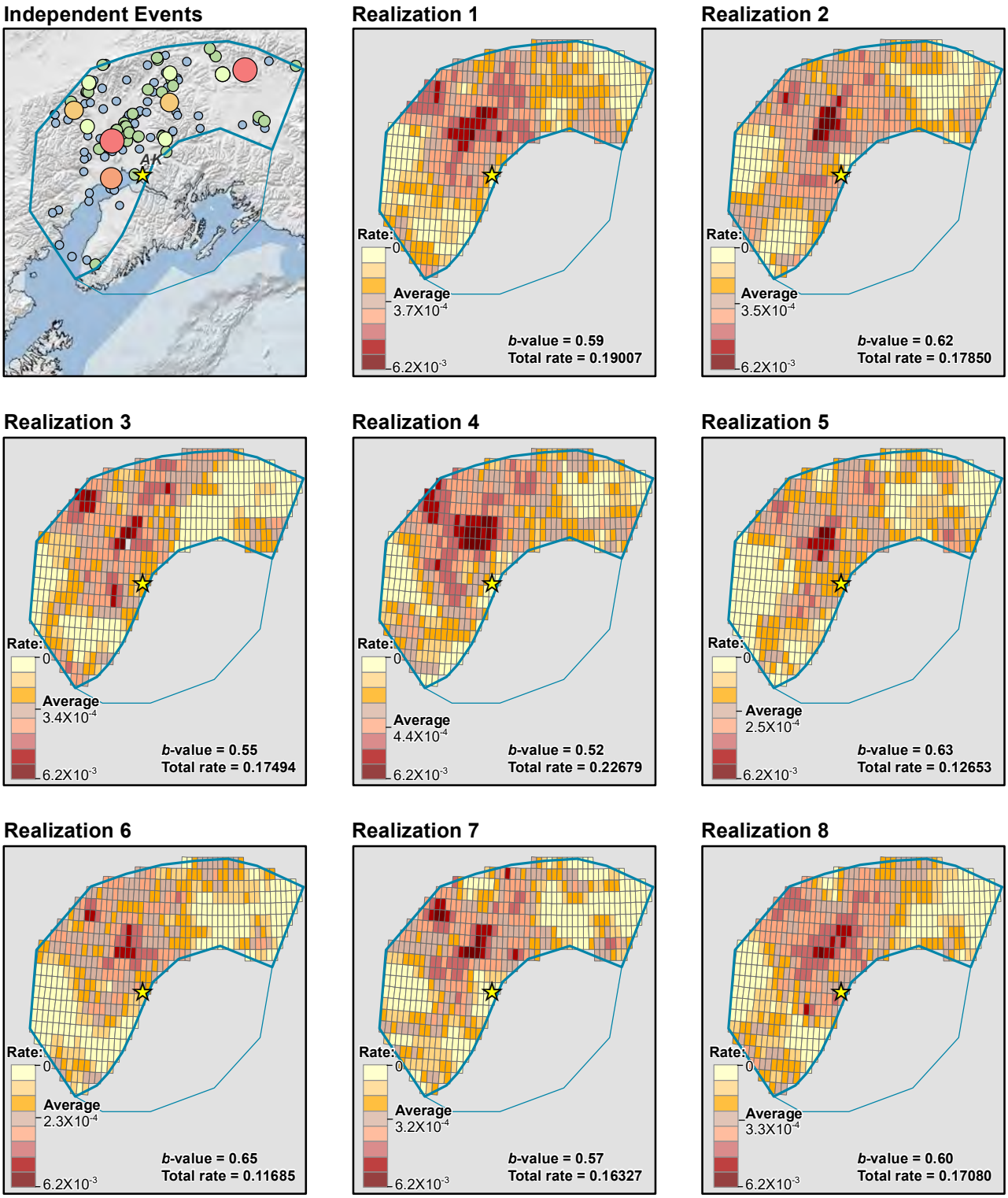

EXPLANATION

- Site location
- Southern Alaska Block and Cook Inlet source zone
- Other areal source zone boundary

Independent Seismicity [M]

- 3.00 - 3.99
- 4.00 - 4.99
- 5.00 - 5.99
- 6.00 - 6.49
- 6.50 - 6.99
- ≥ 7.00

Sources: Seismicity from USGS (2021)

N W E S

0 50 100 mi

0 100 200 km

Map projection and scale:
NAD 1983 UTM Zone 6N, 1:11,500,000

Gridded Seismicity for the Southern Alaska Block and Cook Inlet Source Zone

PORT OF ALASKA

Lettis Consultants International, Inc.

Figure **15**

File path: S:\2218\00_Figures\Figure_15-SABCI_Gridded_Seismicity.mxd; Date: 10/07/2022; User: nora, LCI; Rev.1

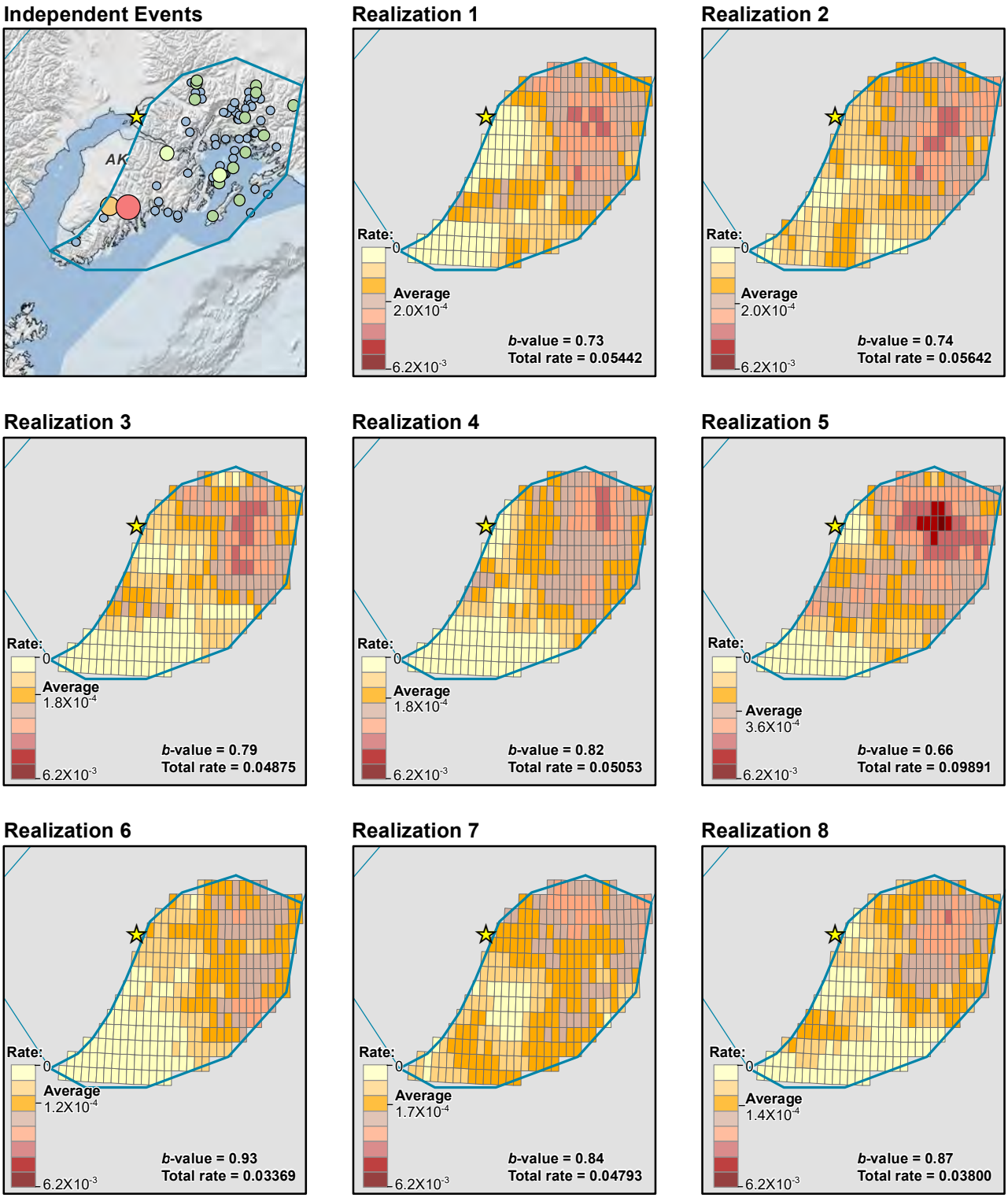

Map projection and scale:
NAD 1983 UTM Zone 6N, 1:9,000,000

EXPLANATION

- Site location
- Yakutat Block source zone
- Other areal source zone boundary

Independent Seismicity [M]

- 3.00 - 3.99
- 4.00 - 4.99
- 5.00 - 5.99
- 6.00 - 6.49
- 6.50 - 6.99
- ≥ 7.00

Sources: Seismicity from USGS (2021)

Gridded Seismicity for the Yakutat Block Source Zone

PORT OF ALASKA

Lettis Consultants International, Inc.

Figure **16**

File path: S:\2218\00_Figures\Figure_16-YB_Gridded_Seismicity.mxd; Date: 10/07/2022; User: nora, LCI; Rev.1

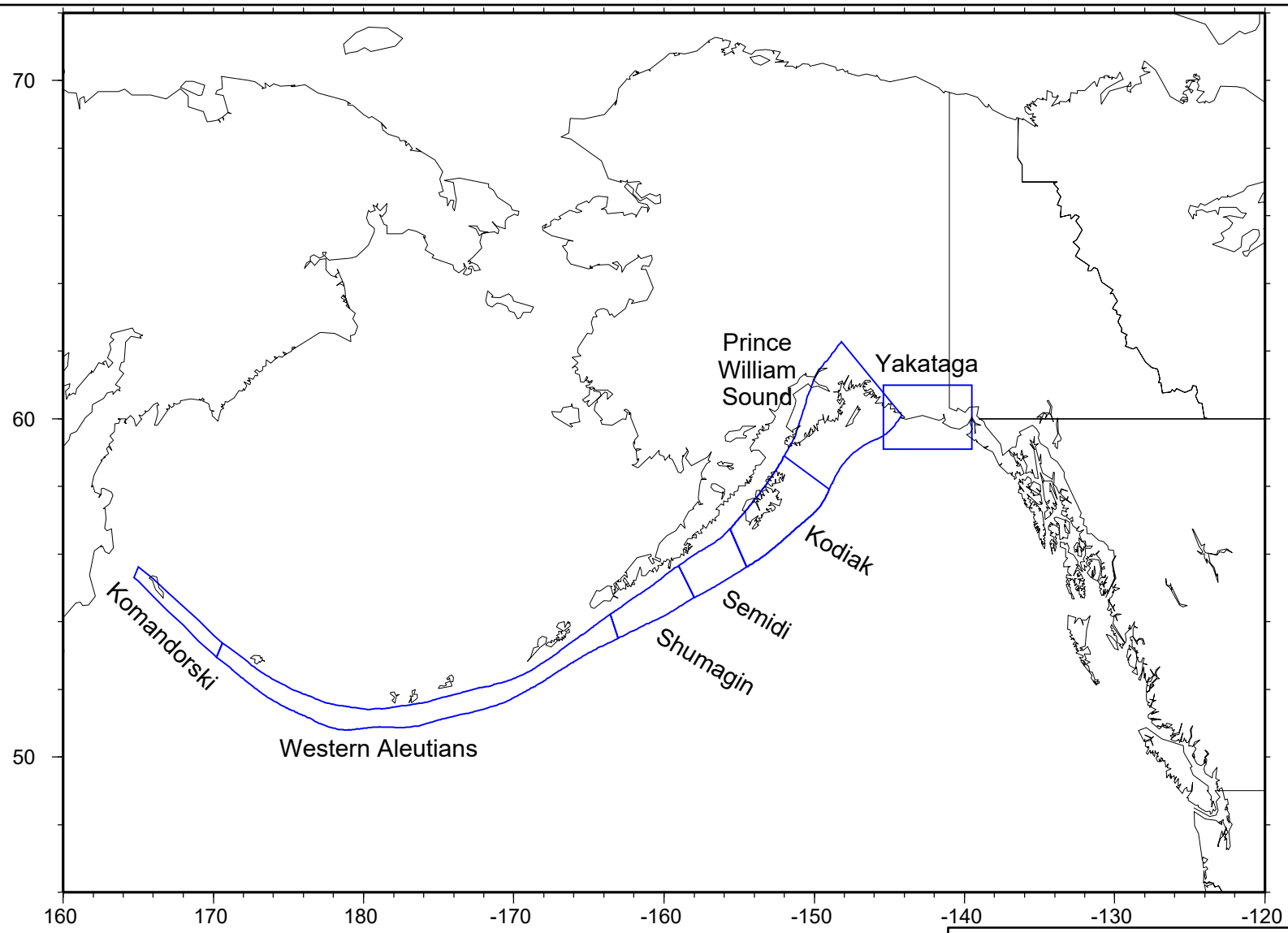

Source: Wesson et al. (2007)

Segmentation of the Alaska-Aleutian Subduction Zone

PORT OF ALASKA

LCI Lettis Consultants International, Inc.

Figure **17**

File path: S:\2218\00_Figures\Figure_17_Schematic_Map.ai; Date: 10/11/2022; User: wka, LCI

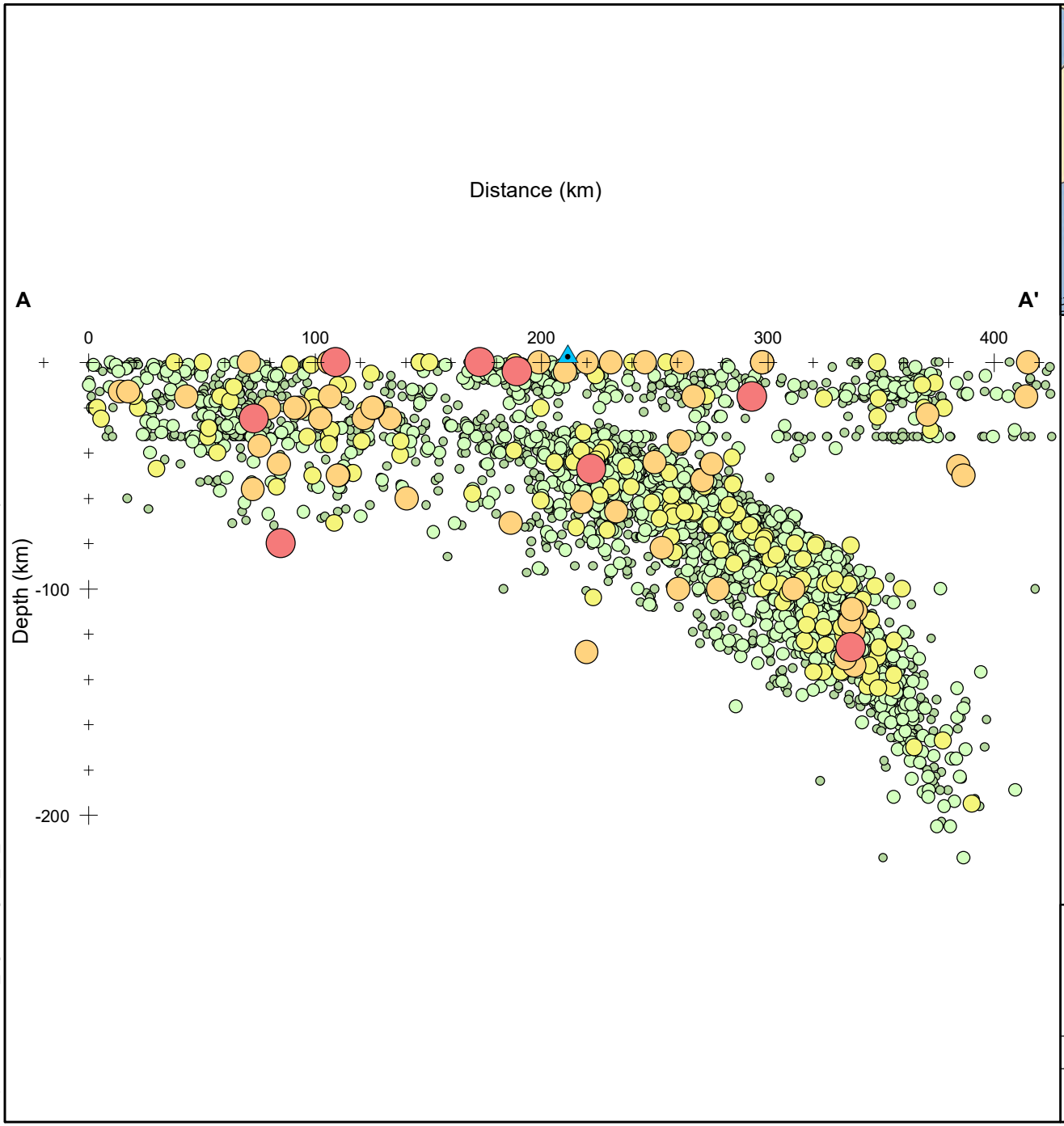

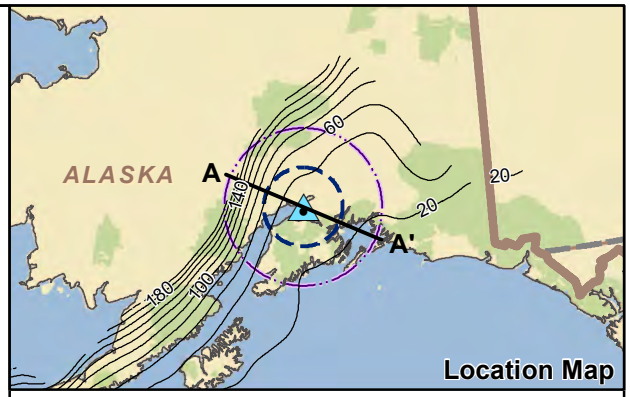

EXPLANATION

- Site location
- 100 km buffer
- 200 km buffer
- Line of cross section
- Slab depth contours

Seismicity [M]

- 3.0 - 3.9
- 4.0 - 4.9
- 5.0 - 5.9
- 6.0 - 6.9
- ≥ 7.0

Sources:
Seismicity catalog from USGS (2021)

N W E S

0 50 100 mi

0 50 100 km

Map projection and scale: NAD 1983 UTM Zone 6N, 1:2,700,000

Cross Section of the Historical Seismicity in the Alaska-Aleutian Wadati-Benioff Zone

PORT OF ALASKA

LCI Lettis Consultants International, Inc. | Figure **18**

File path: S:\2218\00_Figures\Figure_18_CrossSection.mxd; Date: 09/23/2022; User: whitney, LCI; Rev.1

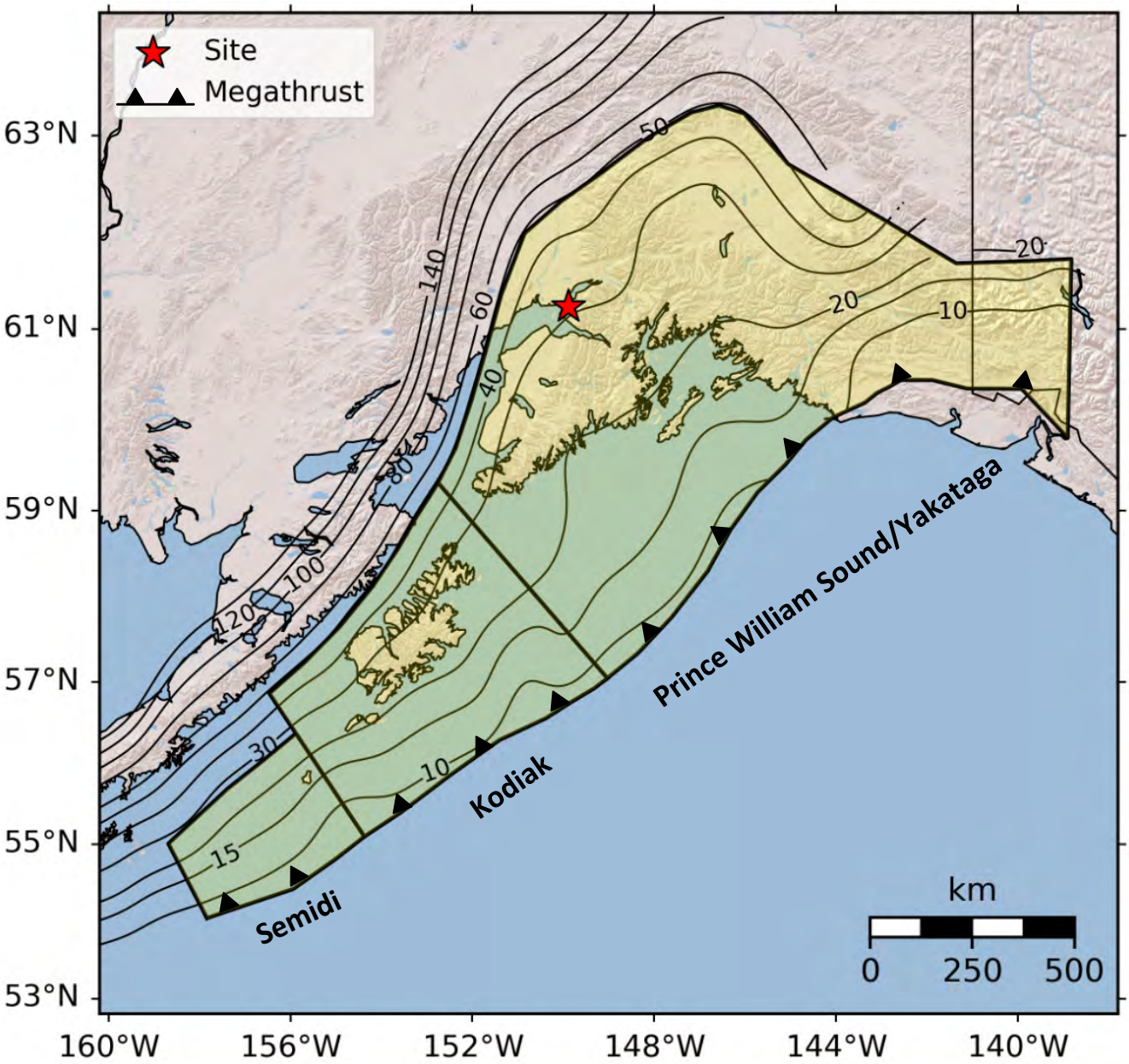

Contour Map of Top of Megathrust and Wadati-Benioff Zone

PORT OF ALASKA

Lettis Consultants International, Inc.

Figure **19**

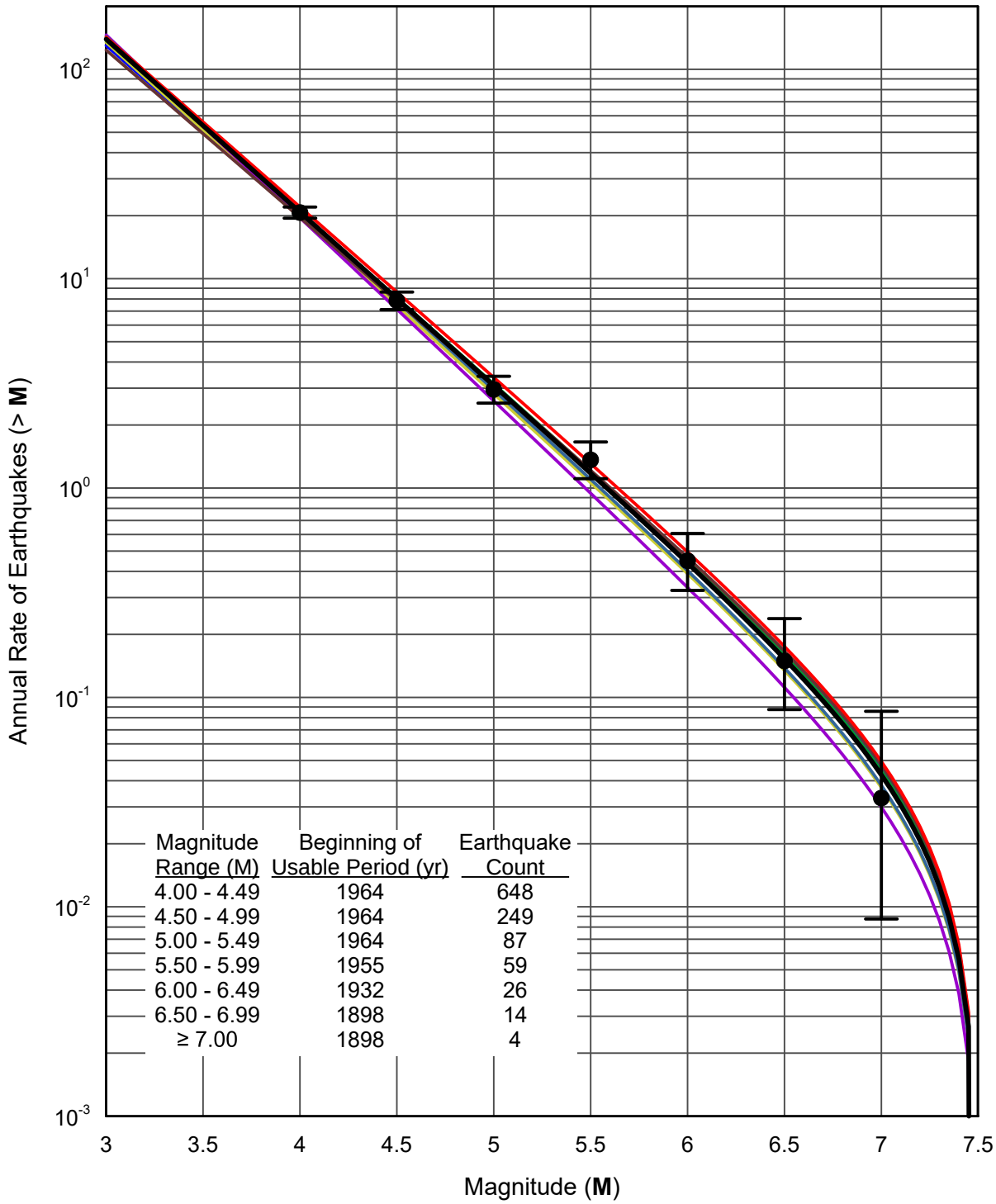

EXPLANATION

● Cumulative earthquake rate

ABSMOOTH Realization

1, 2, 3, 4, 5, 6, 7, 8, Mean

Note: Error bars on cumulative earthquake rate represent two standard deviations.

Cumulative Magnitude-Recurrence Curves for the Intraslab Source Zone for M_{MAX} 7.5

PORT OF ALASKA

Lettis Consultants International, Inc. Figure **20**

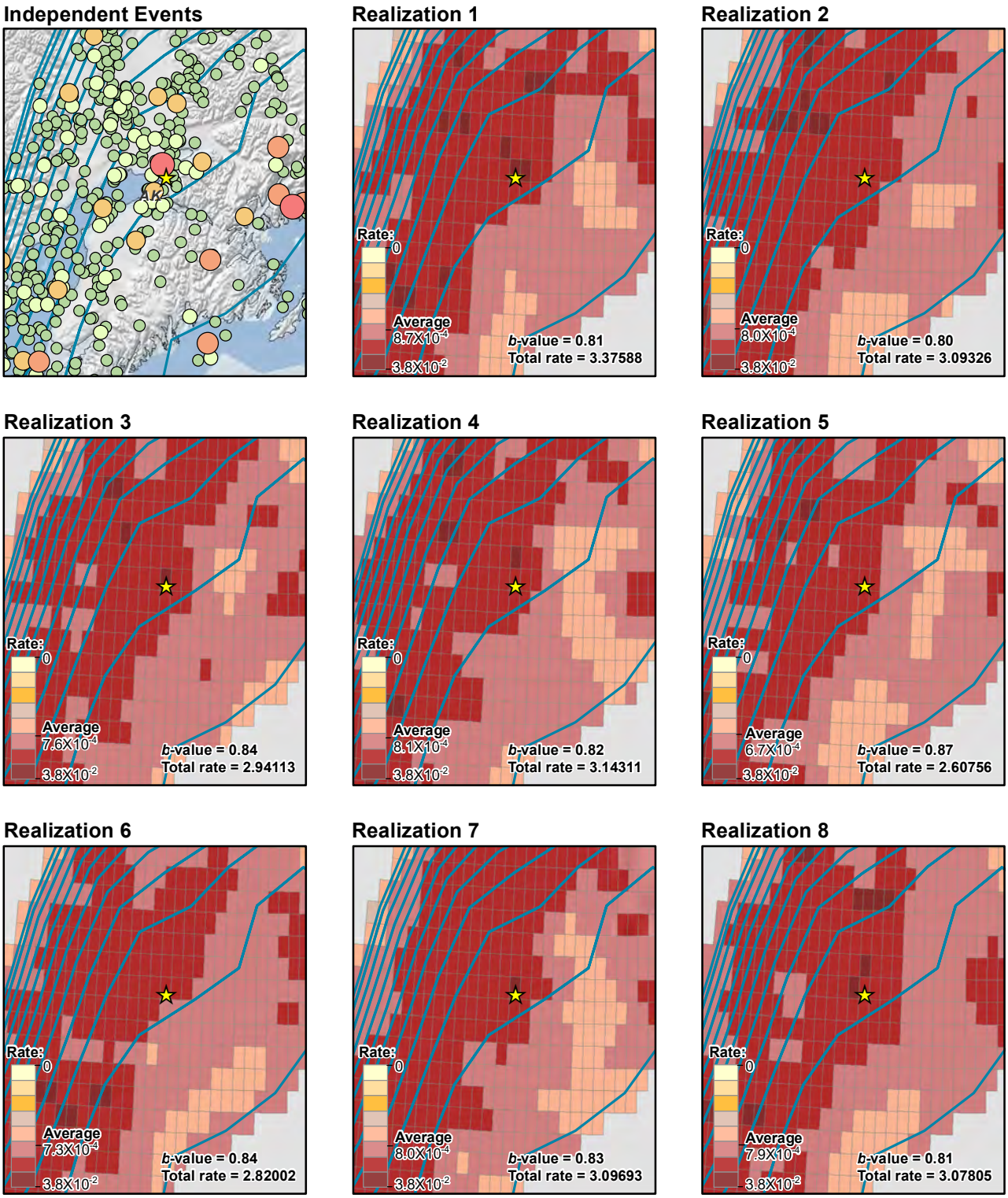

EXPLANATION

Site location

Slab block boundary

Independent Seismicity [M]

- 4.00 - 4.99
- 5.00 - 5.99
- 6.00 - 6.49
- 6.50 - 6.99
- ≥ 7.00

Sources: Seismicity from USGS (2021)

N W E S

0 50 100 mi

0 100 200 km

Map projection and scale:
NAD 1983 UTM Zone 6N, 1:6,000,000

Gridded Seismicity for the Intraslab Zone

PORT OF ALASKA

Lettis Consultants International, Inc.

Figure **21**

File path: S:\2218\00_Figures\Figure_21-Slab_Gridded_Seismicity.mxd; Date: 10/07/2022; User: nora, LCI; Rev.1

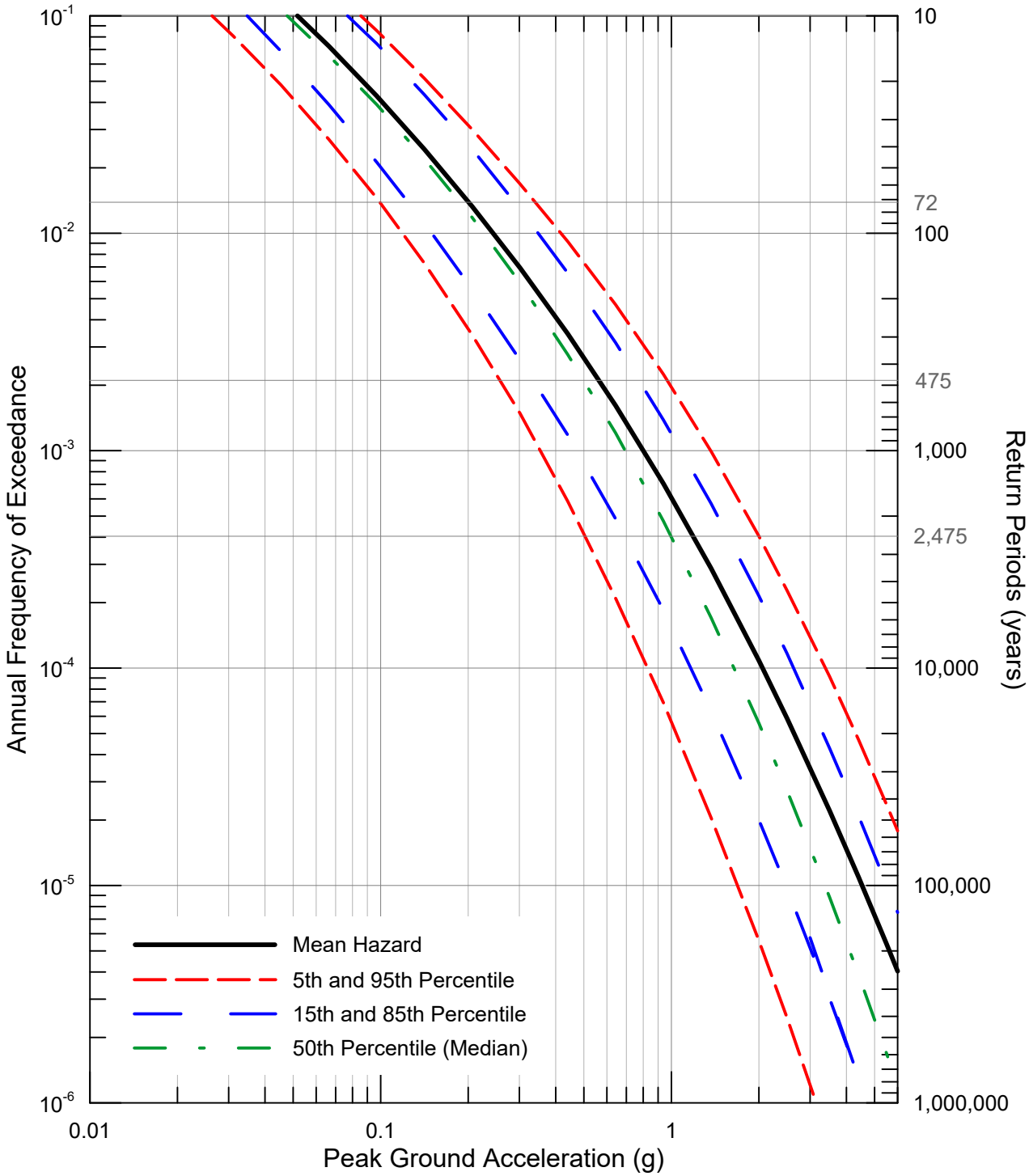

Seismic Hazard Curves
for Peak Horizontal Acceleration
for V_S30 760 m/sec

PORT OF ALASKA

Lettis Consultants International, Inc. | Figure **22**

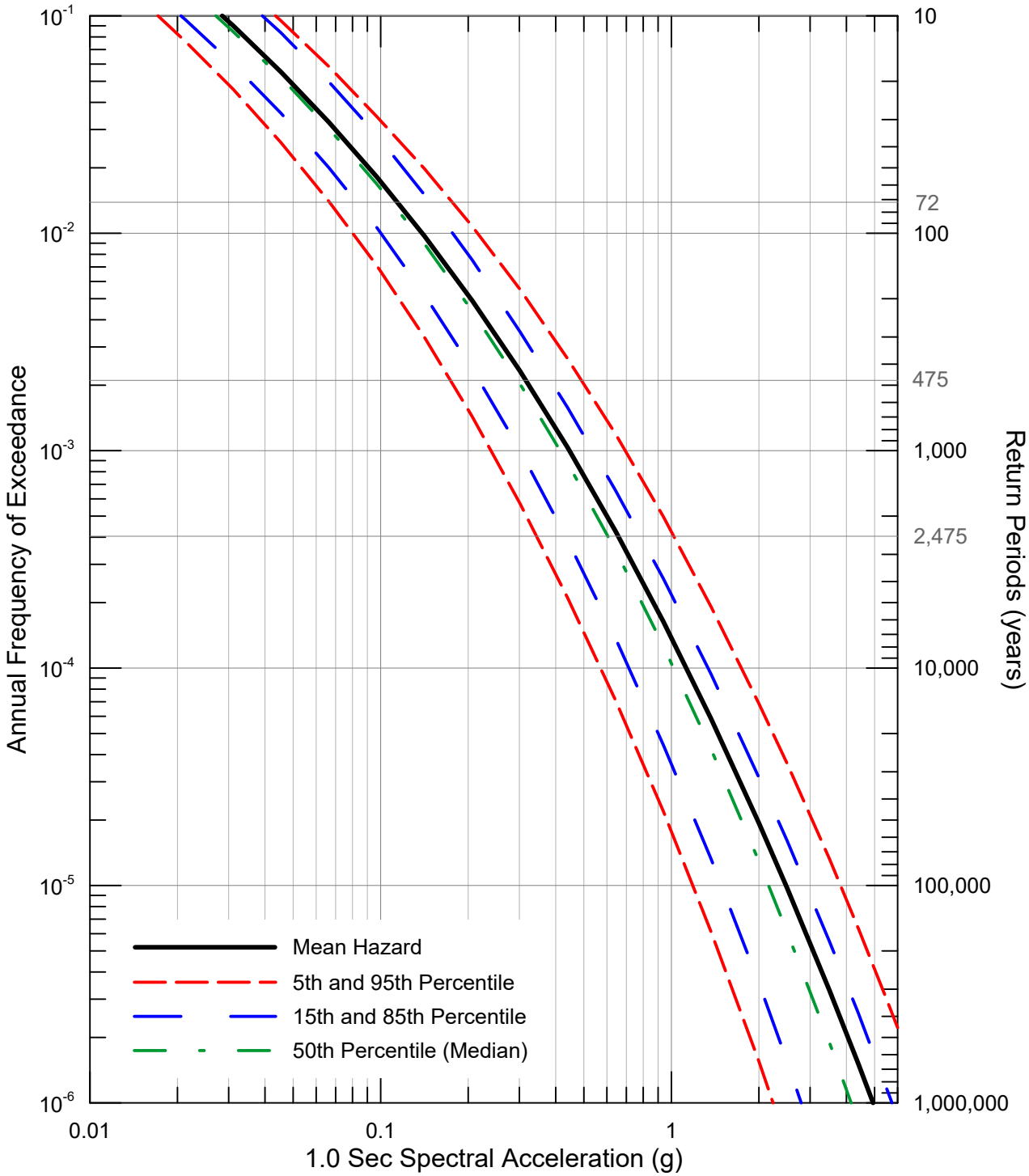

Seismic Hazard Curves for 1.0 Sec Horizontal Spectral Acceleration for V_s30 760 m/sec

PORT OF ALASKA

Lettis Consultants International, Inc.

Figure **23**

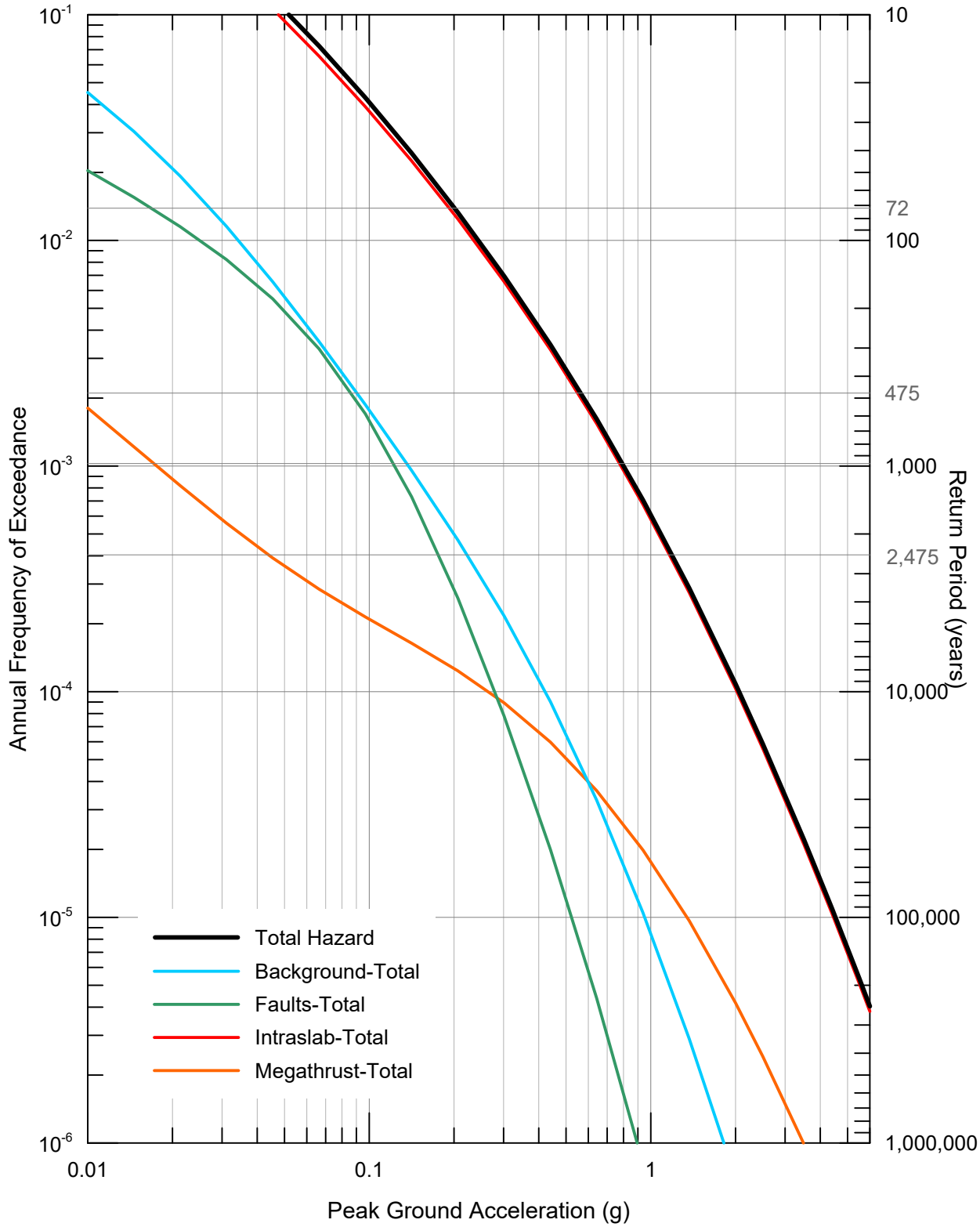

Seismic Source Contributions to Mean Peak Horizontal Acceleration Hazard for V_s30 760 m/sec

PORT OF ALASKA

Lettis Consultants International, Inc. Figure **24**

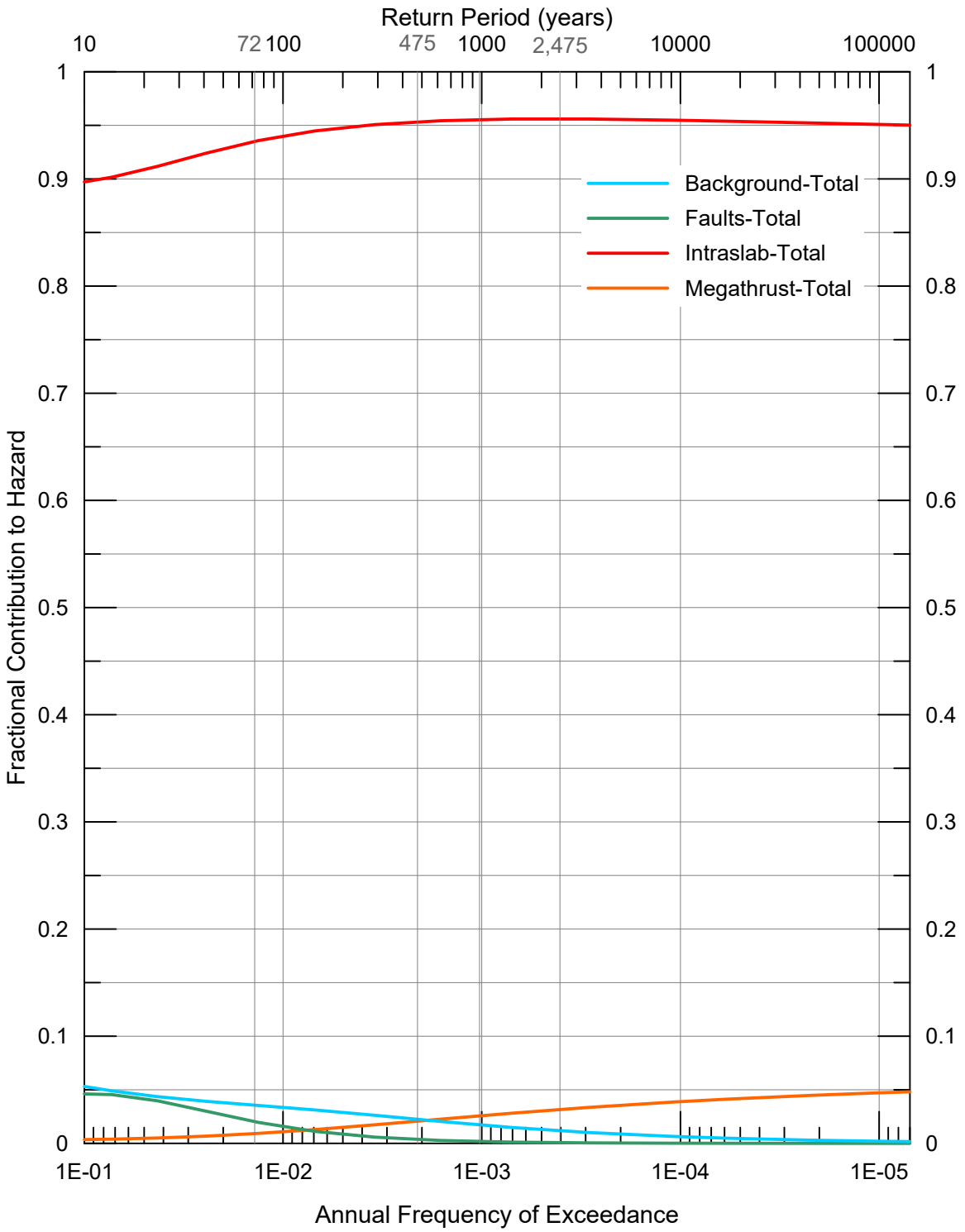

Seismic Source Fractional Contributions to Mean Peak Horizontal Acceleration Hazard for V_s30 760 m/sec

PORT OF ALASKA

Lettis Consultants International, Inc. Figure **25**

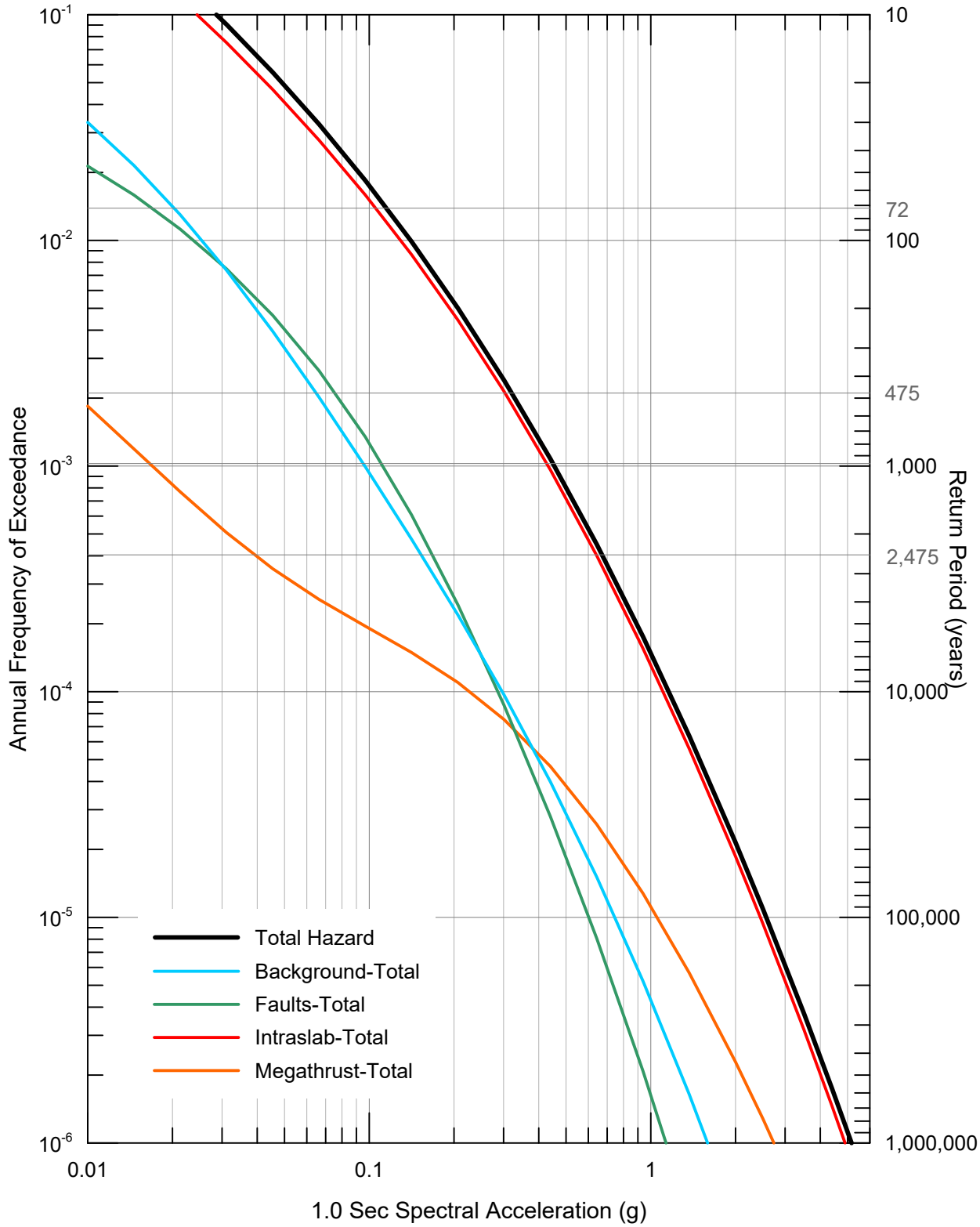

Seismic Source Contributions to Mean 1.0 Sec Horizontal Acceleration Hazard for V_s30 760 m/sec

PORT OF ALASKA

Lettis Consultants International, Inc. Figure **26**

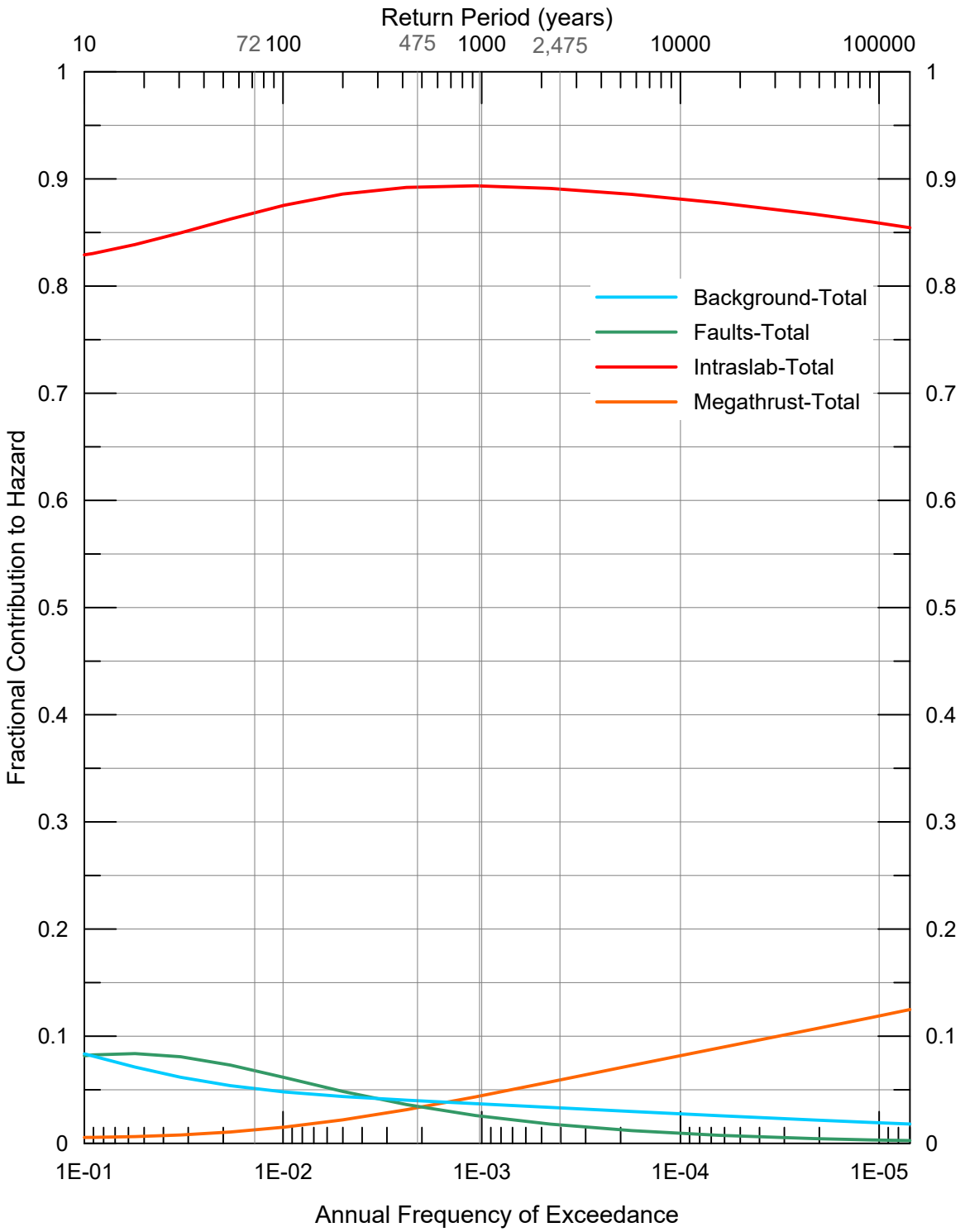

Seismic Source Fractional Contributions to Mean 1.0 Sec Horizontal Acceleration Hazard for V_s30 760 m/sec

PORT OF ALASKA

Lettis Consultants International, Inc. Figure **27**

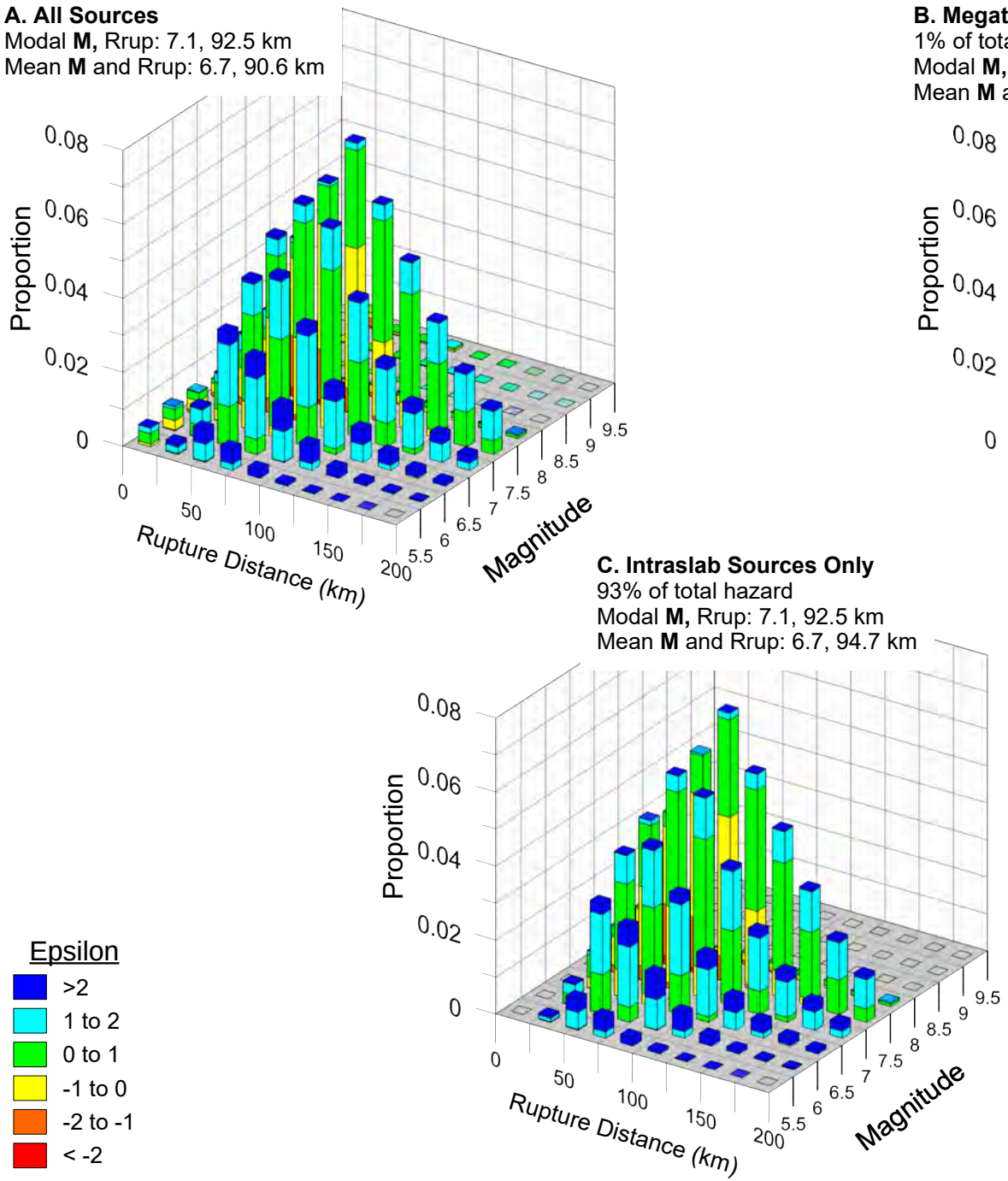

Magnitude, Distance, and Epsilon Contributions to the Mean Peak Horizontal Acceleration Hazard at 72-Year Return Period for V_s30 760 m/sec

PORT OF ALASKA

Lettis Consultants International, Inc.

Figure **28a**

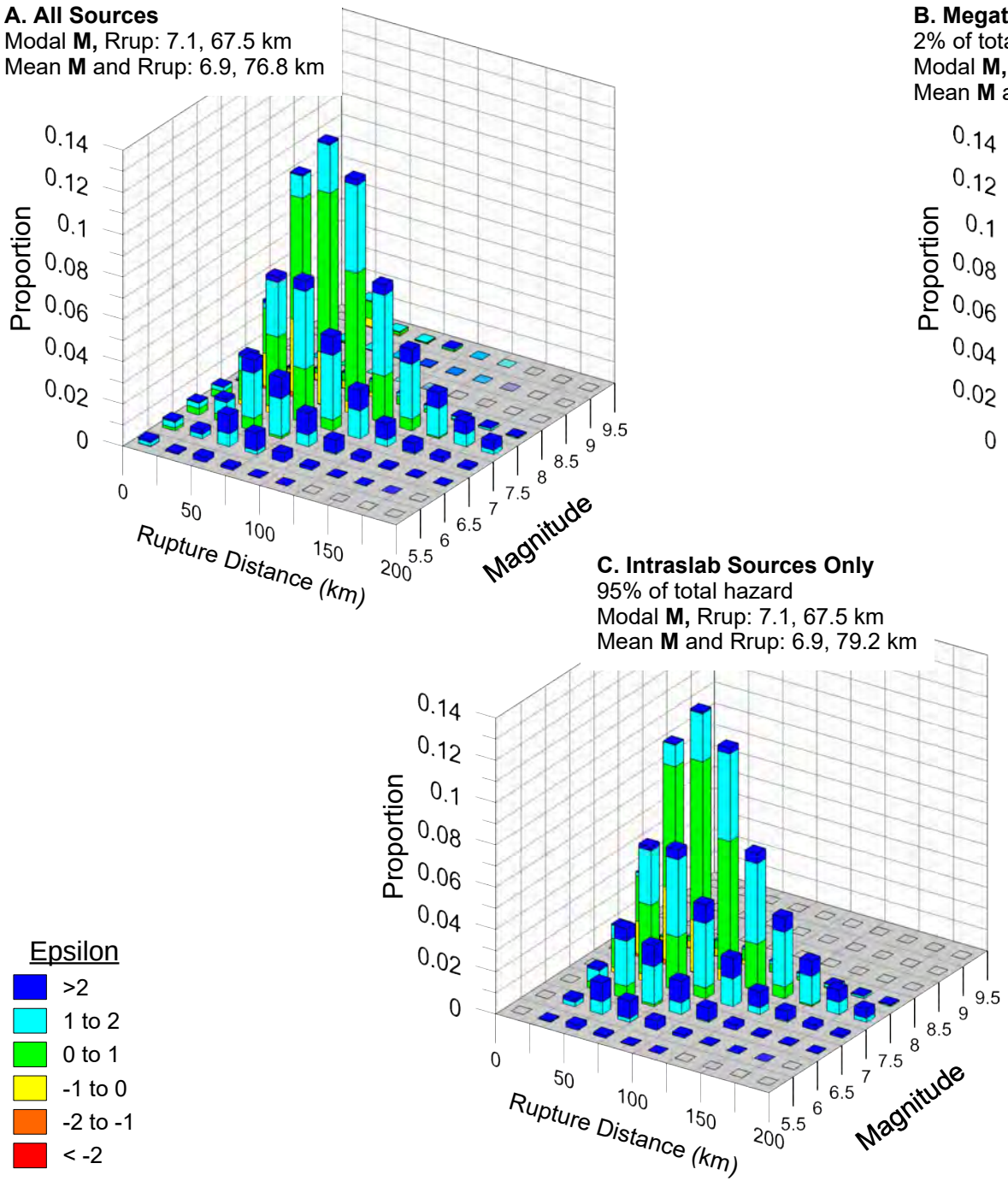

Magnitude, Distance, and Epsilon Contributions to the Mean Peak Horizontal Acceleration Hazard at 475-Year Return Period for V_s30 760 m/sec

PORT OF ALASKA

LCI **Lettis Consultants International, Inc.**

Figure **28b**

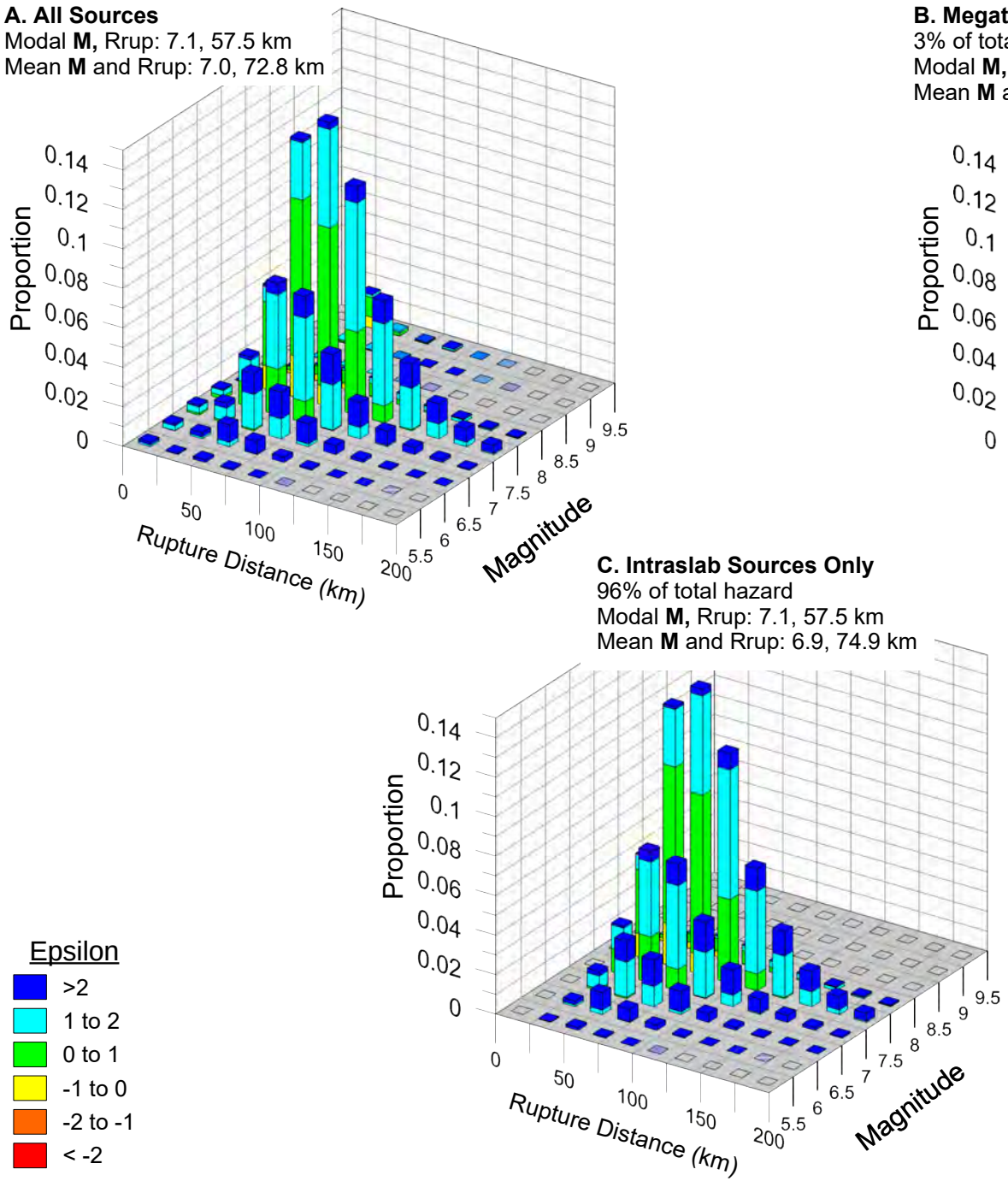

Magnitude, Distance, and Epsilon Contributions to the Mean Peak Horizontal Acceleration Hazard at 975-Year Return Period for V_s30 760 m/sec

PORT OF ALASKA

Lettis Consultants International, Inc.

Figure **28c**

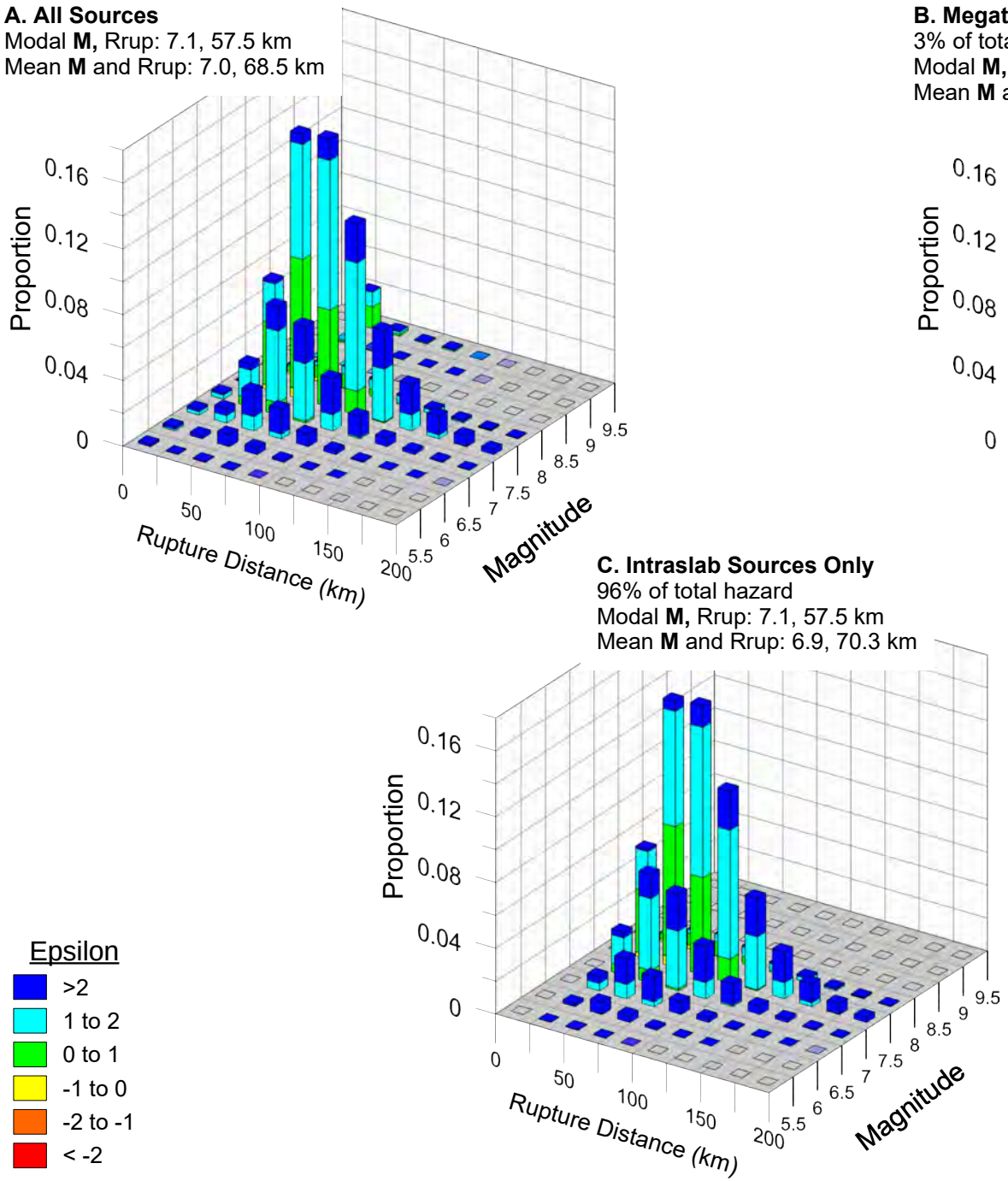

Magnitude, Distance, and Epsilon Contributions to the Mean Peak Horizontal Acceleration Hazard at 2,475-Year Return Period for V_s30 760 m/sec

PORT OF ALASKA

Lettis Consultants International, Inc.

Figure **28d**

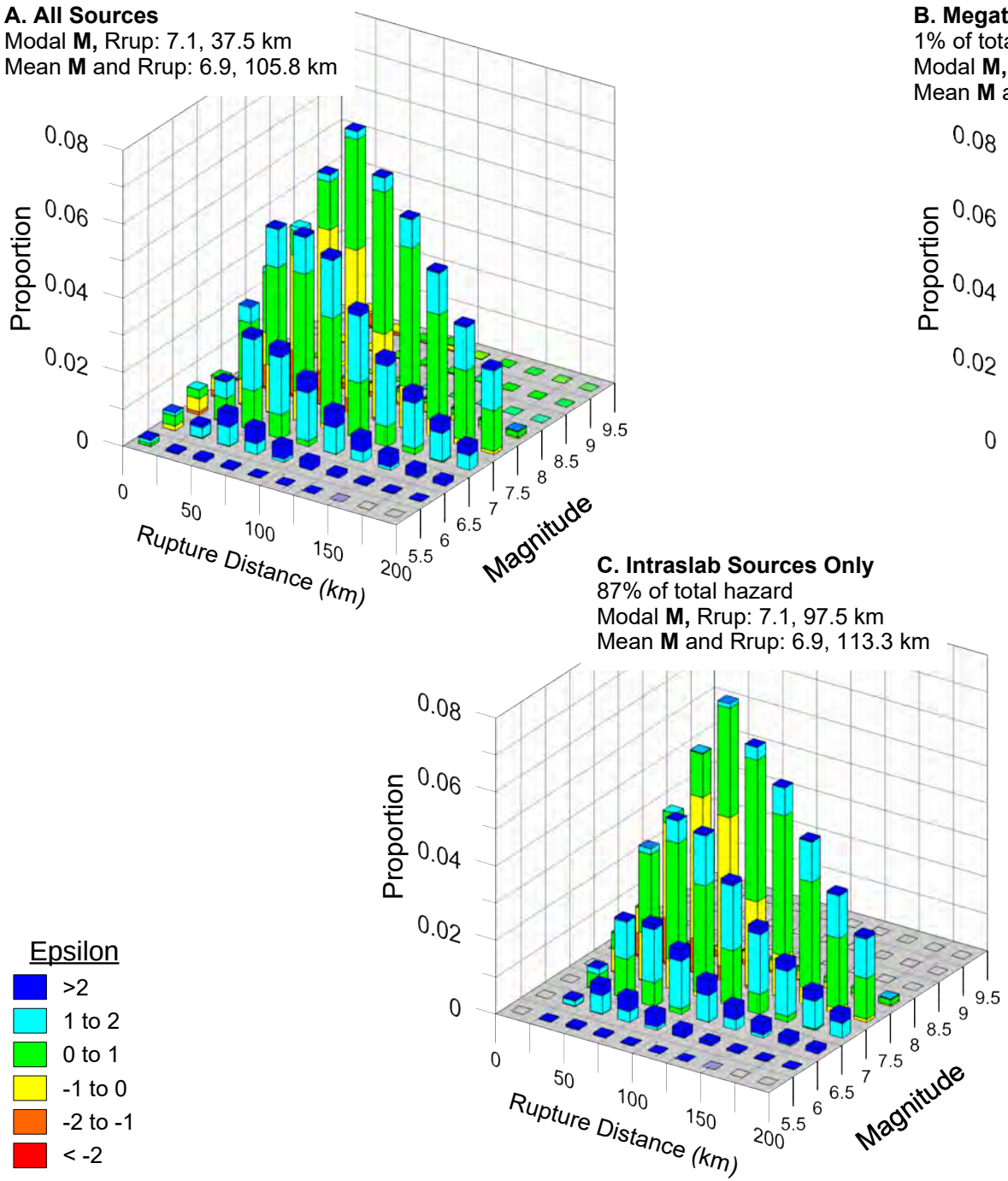

Magnitude, Distance, and Epsilon Contributions to the Mean 1.0 Sec Horizontal Acceleration Hazard at the 72-Year Return Period for V_s30 760 m/sec

PORT OF ALASKA

Lettis Consultants International, Inc.

Figure **29a**

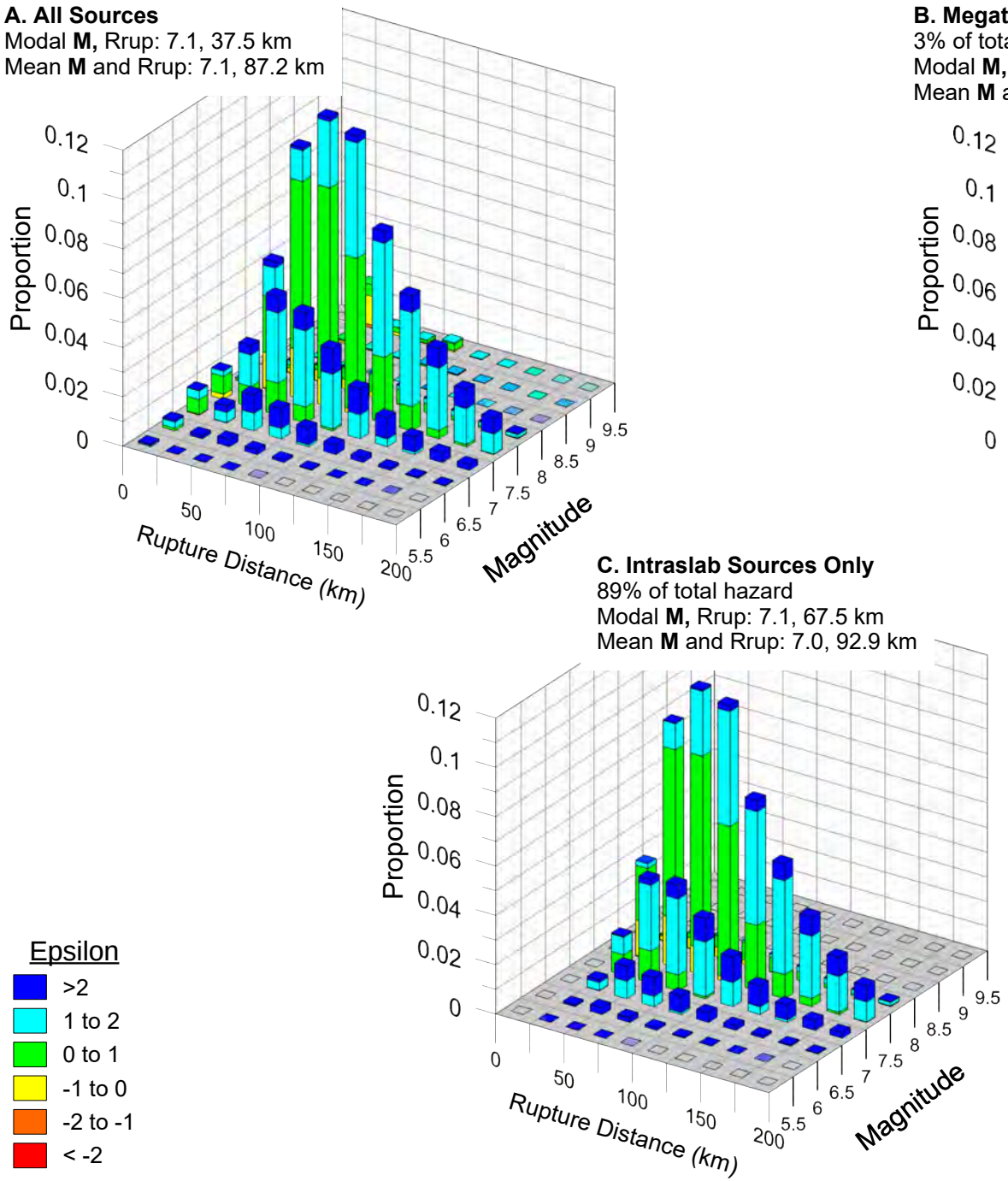

Magnitude, Distance, and Epsilon Contributions to the Mean 1.0 Sec Horizontal Acceleration Hazard at the 475-Year Return Period for V_s30 760 m/sec

PORT OF ALASKA

Lettis Consultants International, Inc.

Figure **29b**

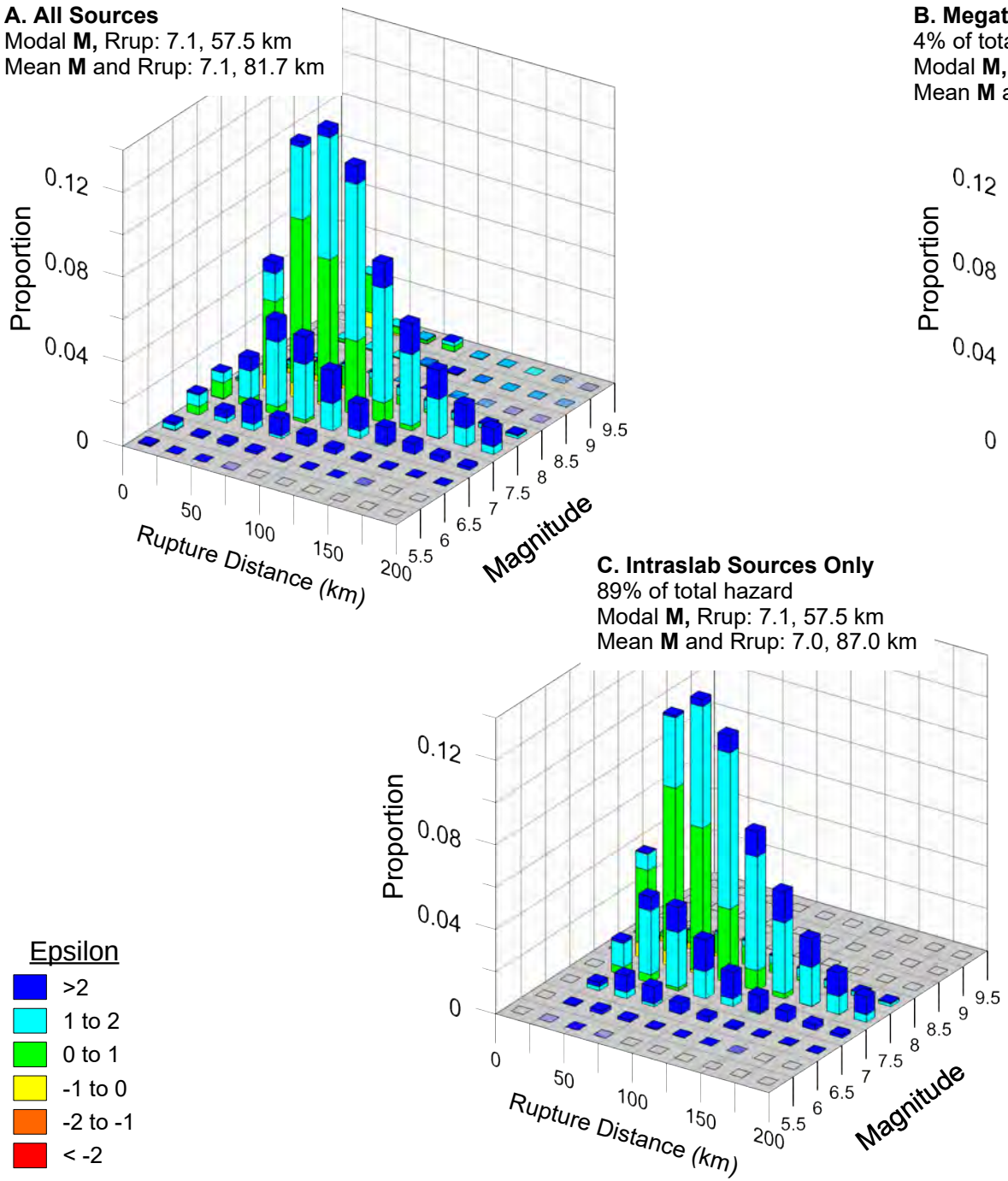

Magnitude, Distance, and Epsilon Contributions to the Mean 1.0 Sec Horizontal Acceleration Hazard at the 975-Year Return Period for V_s30 760 m/sec

PORT OF ALASKA

Lettis Consultants International, Inc.

Figure **29c**

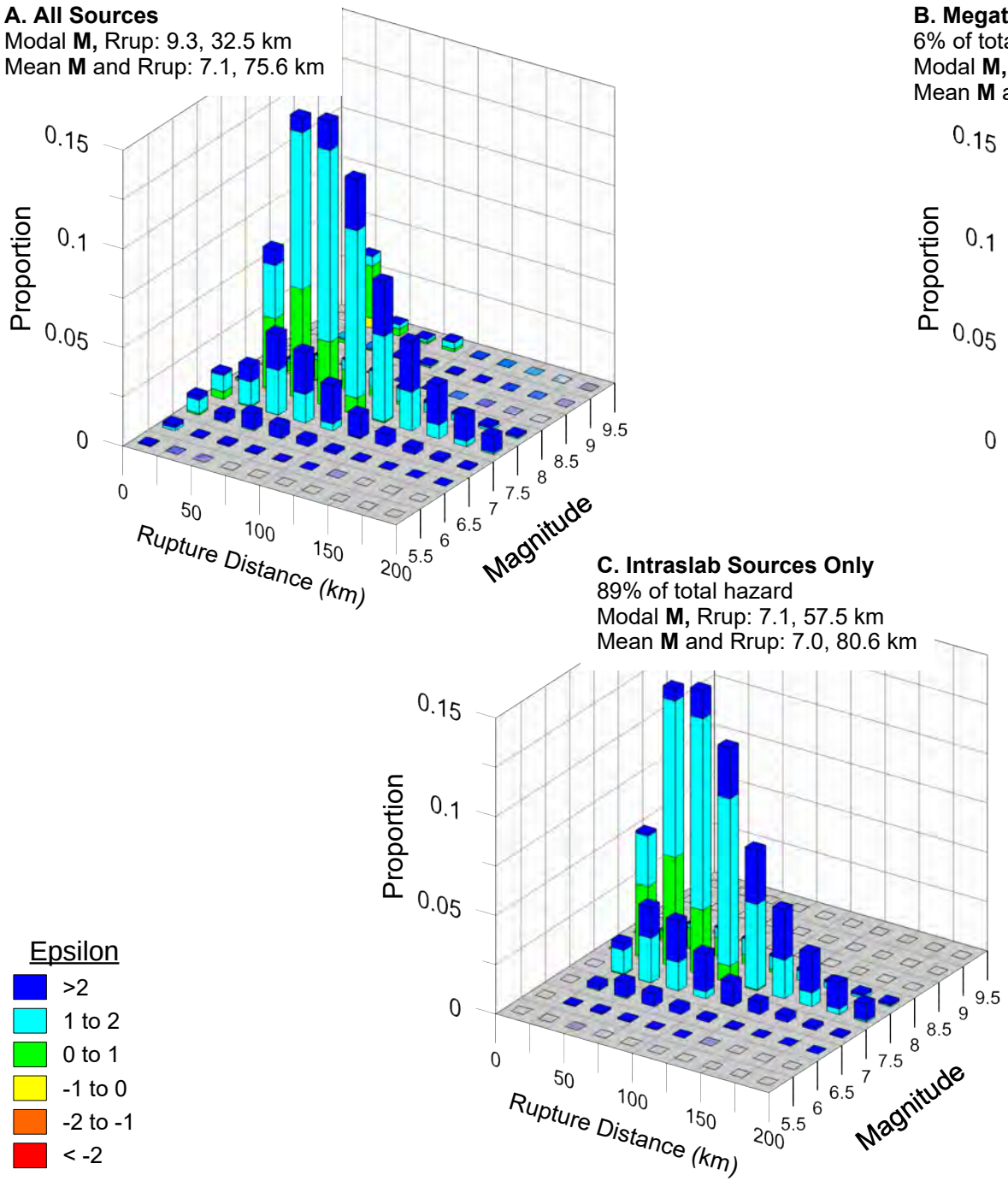

Magnitude, Distance, and Epsilon Contributions to the Mean 1.0 Sec Horizontal Acceleration Hazard at the 2,475-Year Return Period for V_s30 760 m/sec

PORT OF ALASKA

Lettis Consultants International, Inc.

Figure **29d**

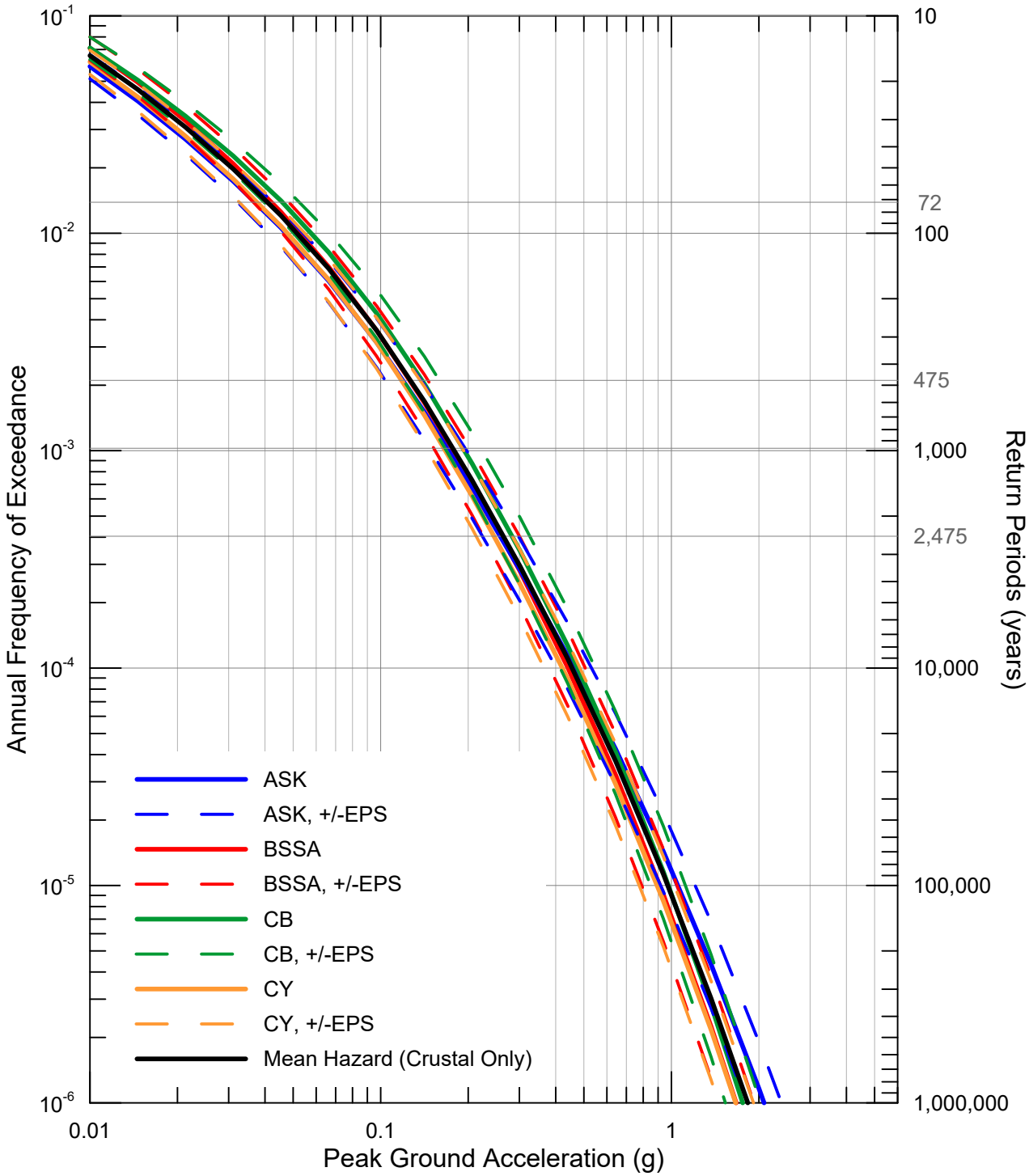

Sensitivity of Mean Peak Horizontal Acceleration Hazard to Crustal GMMs for V_S30 760 m/sec

PORT OF ALASKA

Lettis Consultants International, Inc. Figure **30**

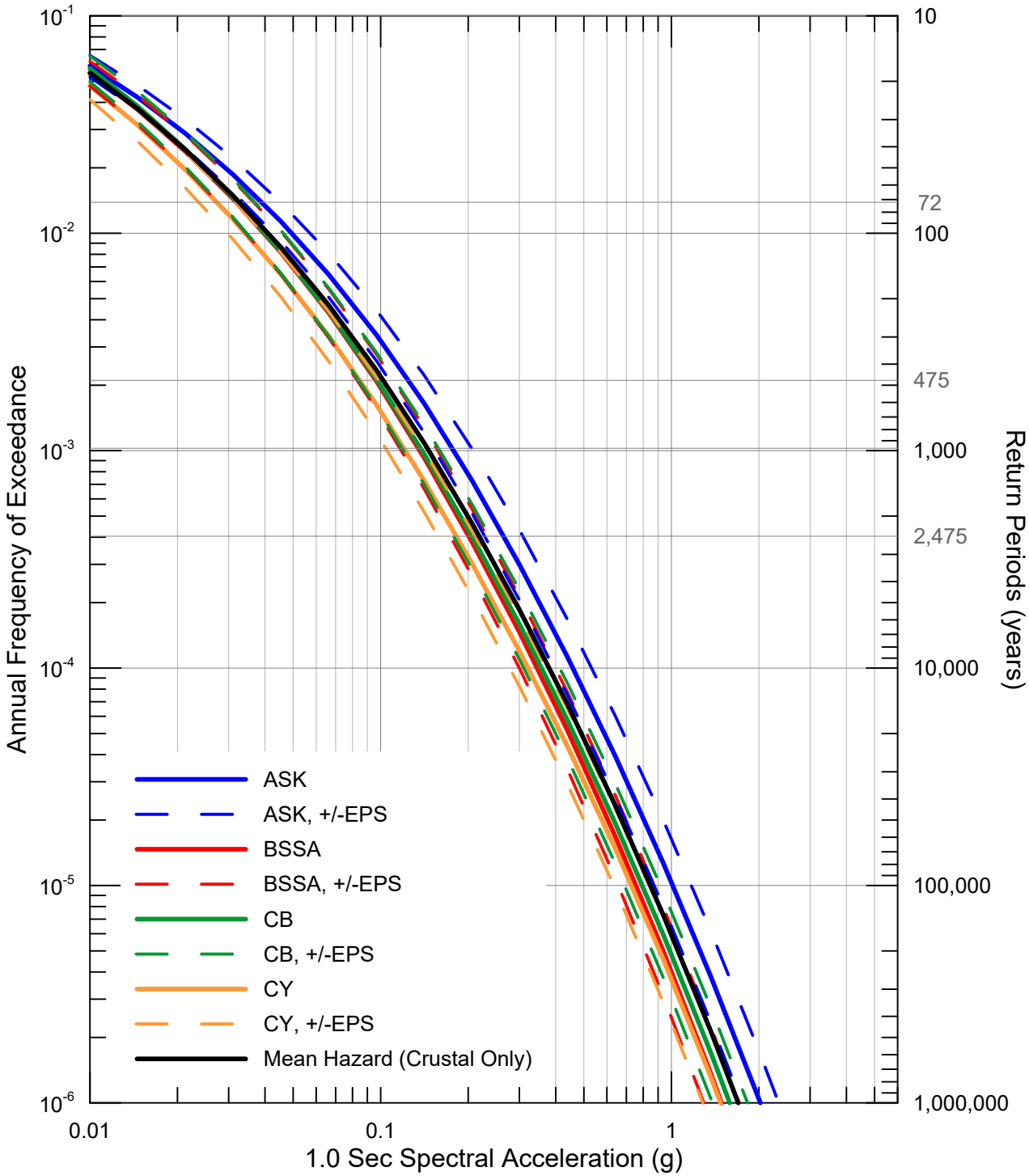

Sensitivity of Mean 1.0 Sec Horizontal Spectral Acceleration to Crustal GMMs for V_s30 760 m/sec

PORT OF ALASKA

Lettis Consultants International, Inc. Figure **31**

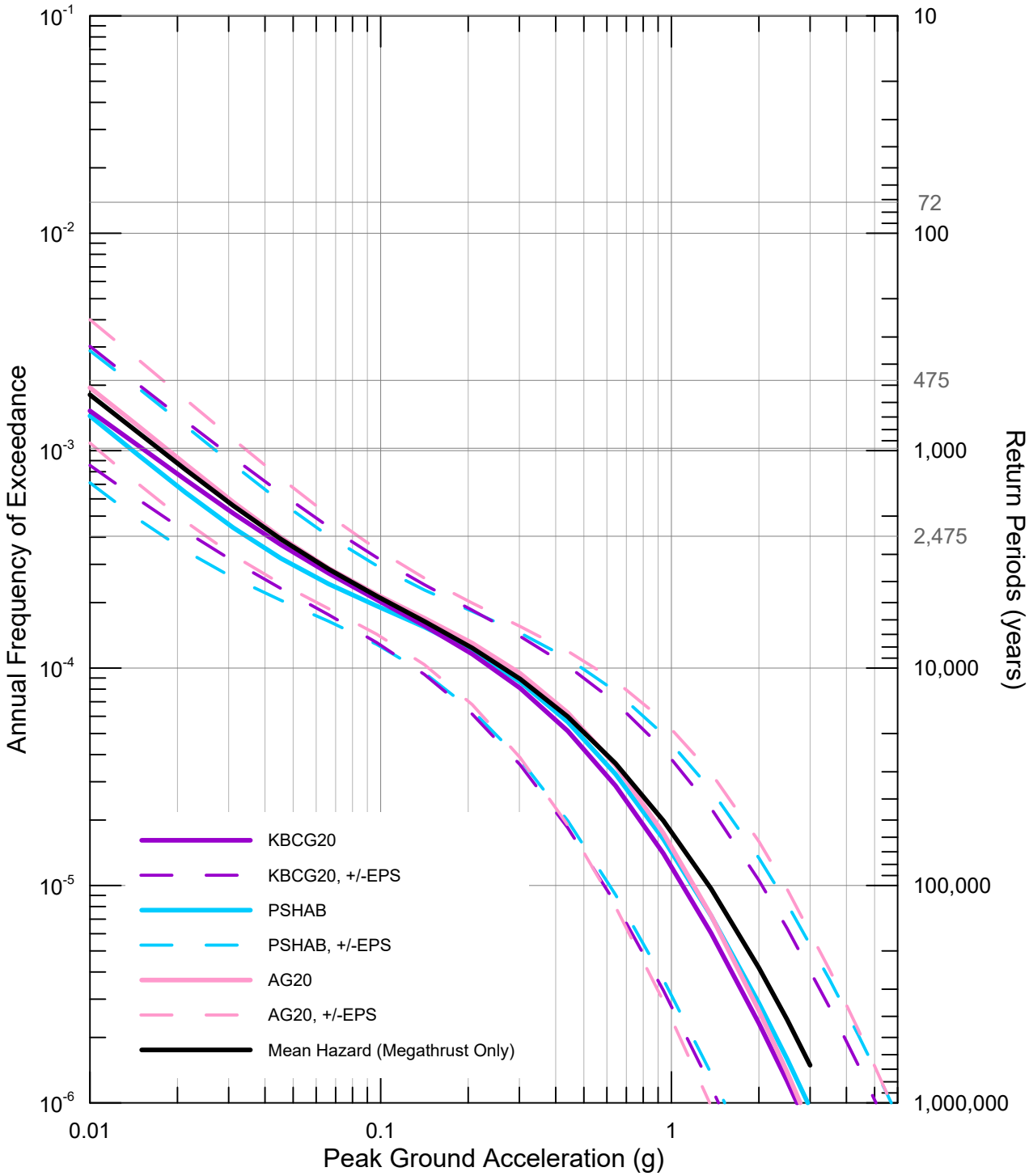

Sensitivity of Mean Peak Horizontal Acceleration Hazard to Megathrust GMMs for V_s30 760 m/sec

PORT OF ALASKA

Lettis Consultants International, Inc. Figure **32**

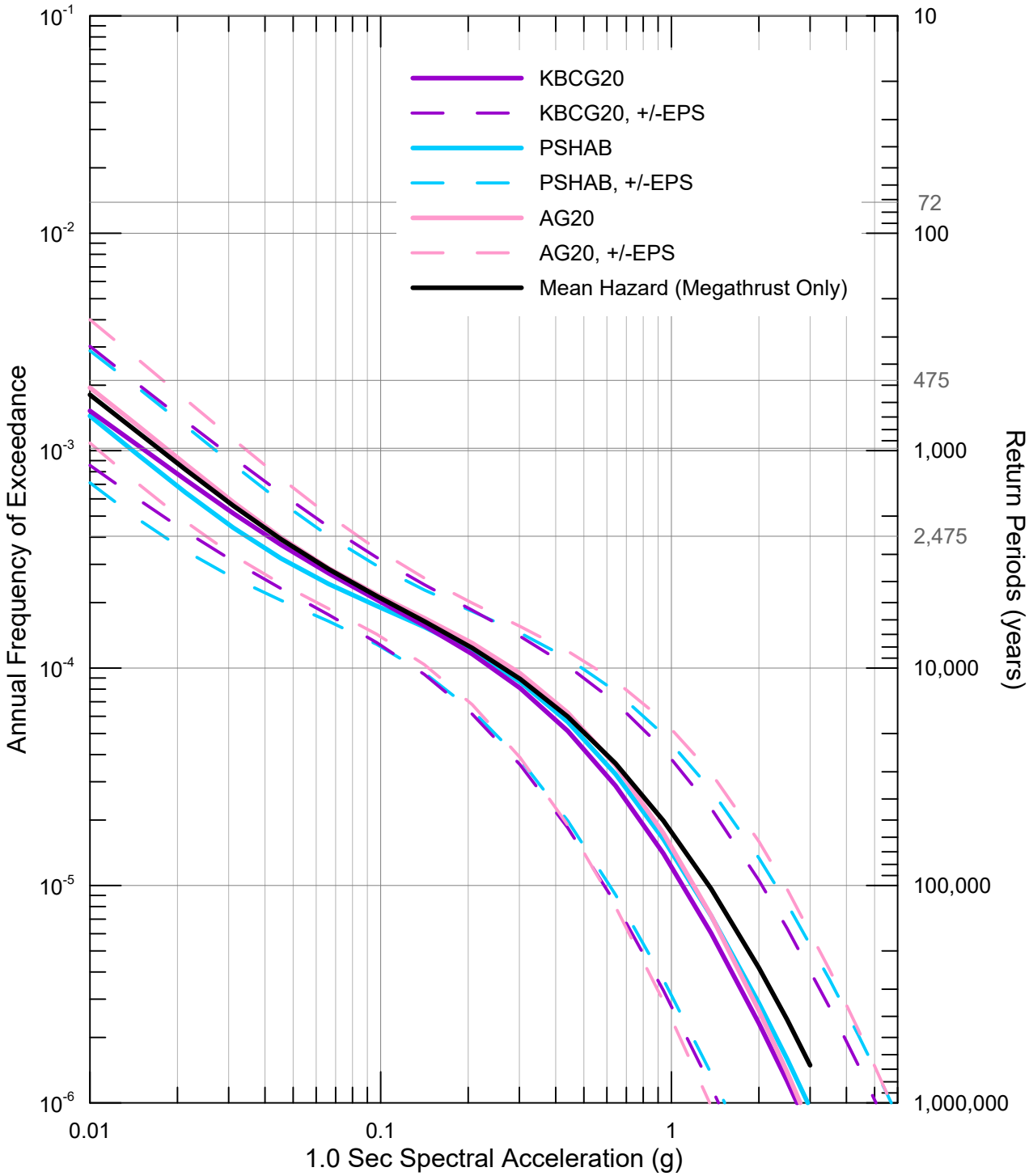

Sensitivity of Mean 1.0 Sec Horizontal Spectral Acceleration to Megathrust GMMs for V_s30 760 m/sec

PORT OF ALASKA

Lettis Consultants International, Inc. | Figure **33**

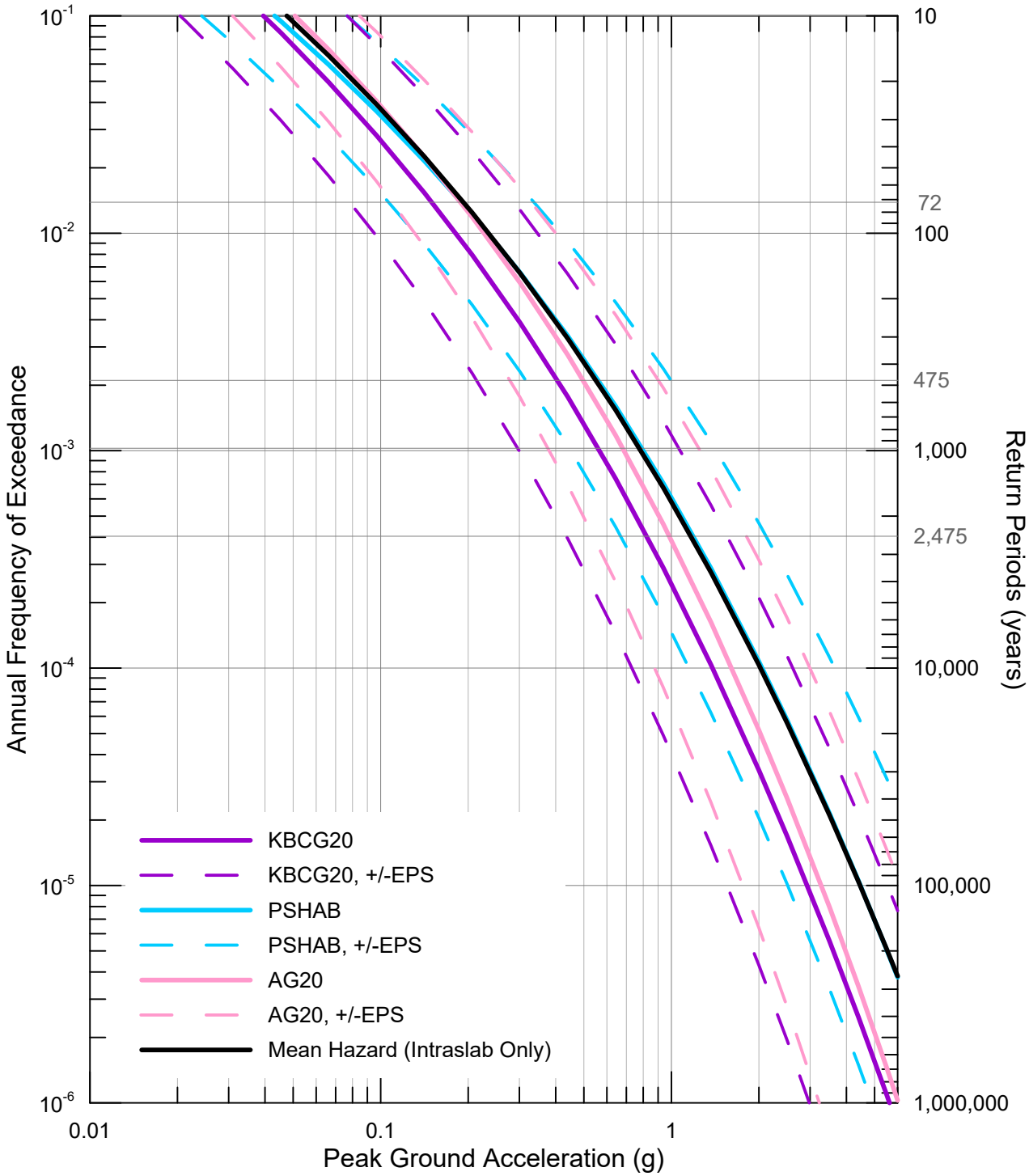

Sensitivity of Mean Peak Horizontal Acceleration Hazard to Intraslab GMMs for V_s30 760 m/sec

PORT OF ALASKA

Lettis Consultants International, Inc. Figure **34**

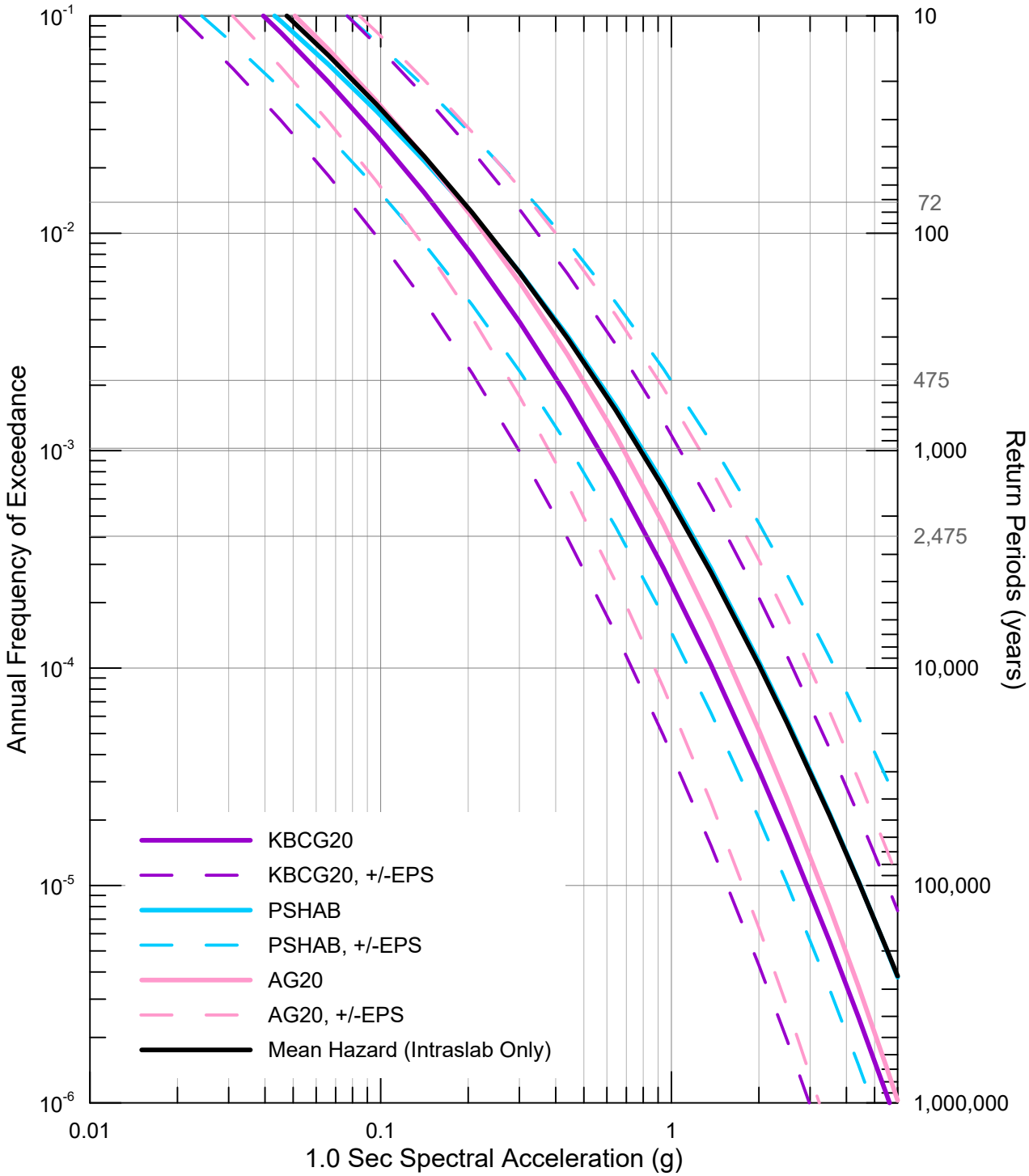

Sensitivity of Mean 1.0 Sec Horizontal Spectral Acceleration to Intraslab GMMs for V_s30 760 m/sec

PORT OF ALASKA

Lettis Consultants International, Inc. Figure **35**

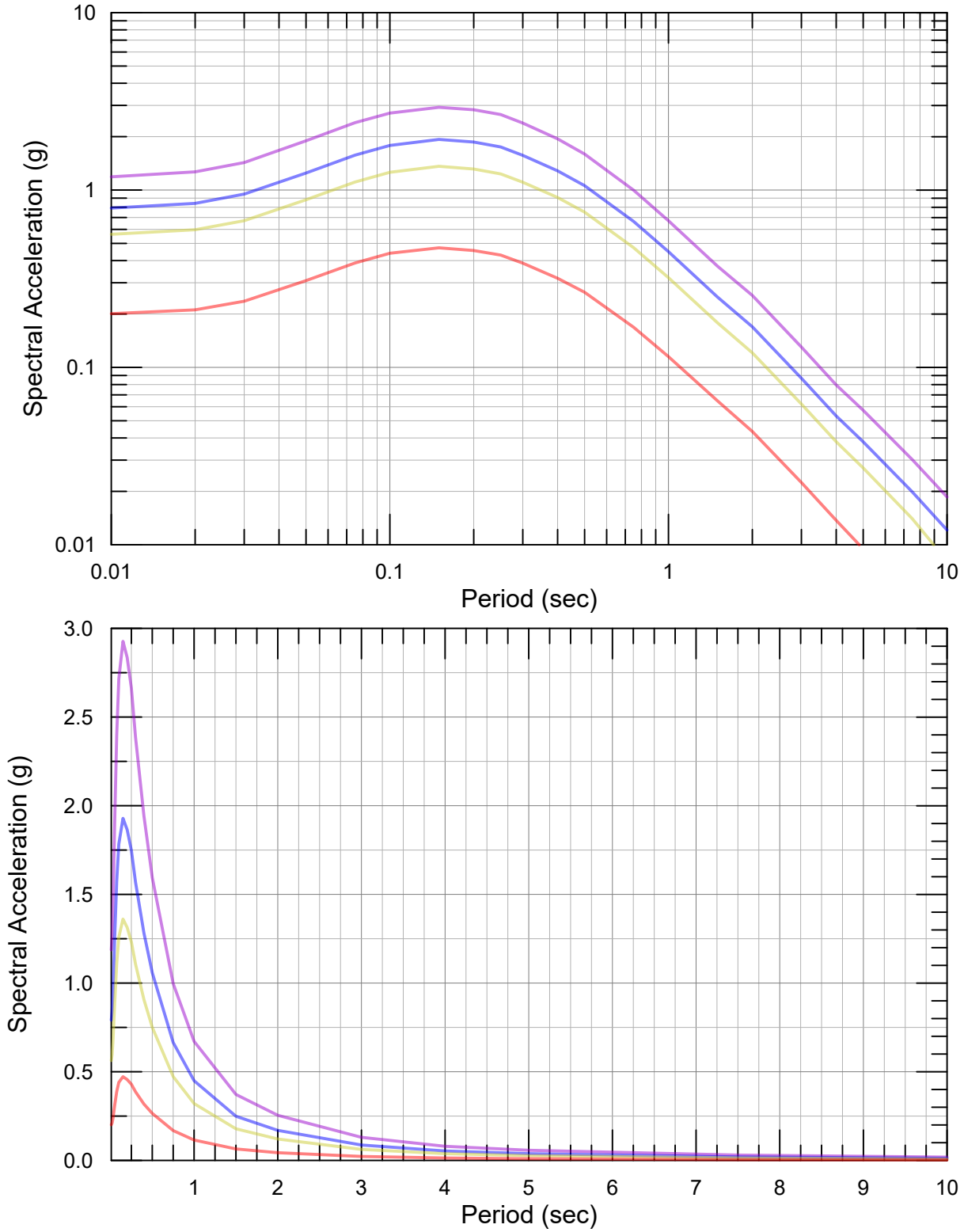

Return Period (yr)

- 72
- 475
- 975
- 2,475

5%-Damped Uniform Hazard Spectra at the 72-, 475-, 975-, and 2,475-Year Return Periods

PORT OF ALASKA

Lettis Consultants International, Inc. Figure **36**

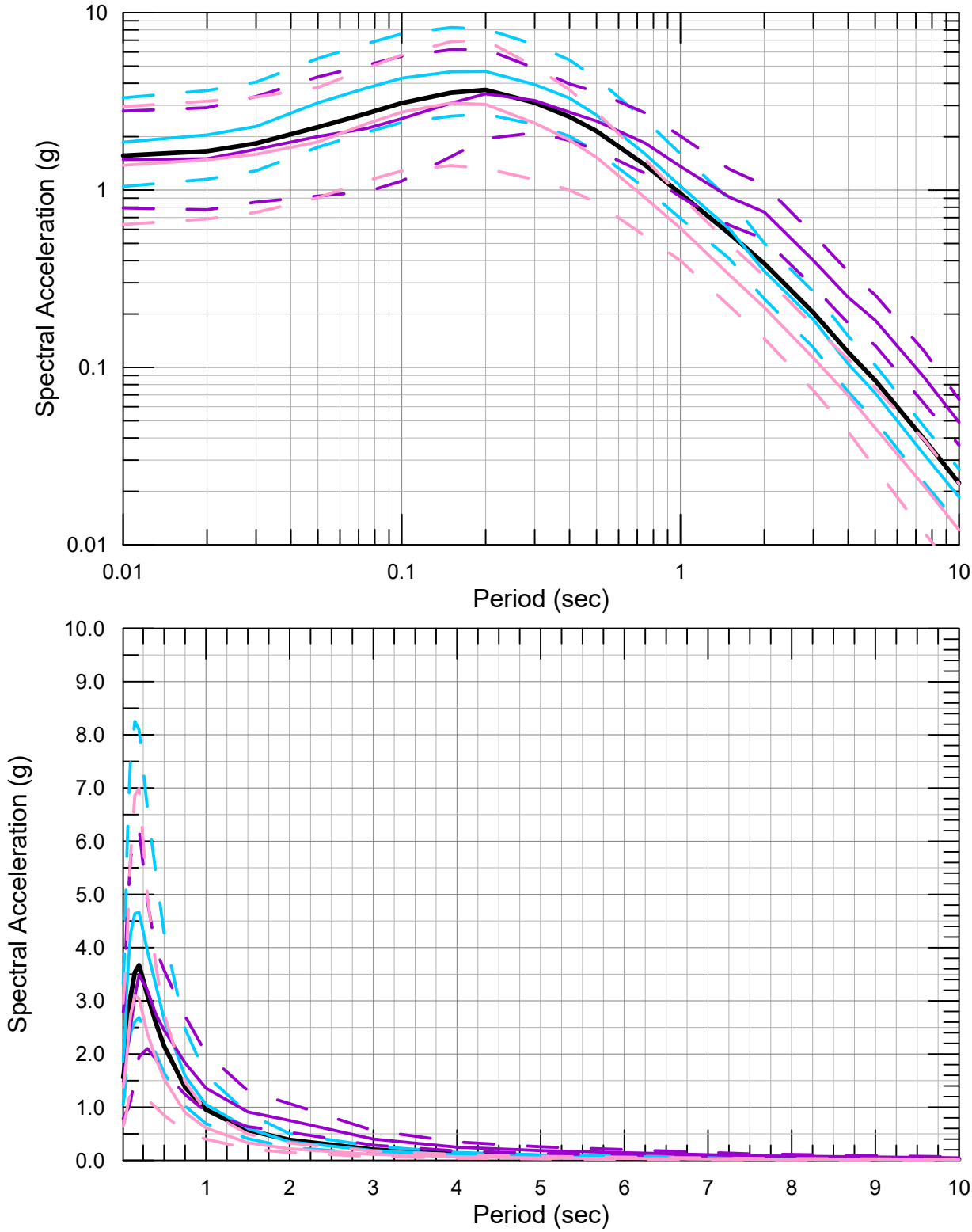

KBCG20
KBCG20, +/-EPS
PSHAB
PSHAB, +/-EPS
AG20
AG20, +/-EPS
Weighted Average

84th Percentile Deterministic Horizontal Acceleration Response Spectra for the M 7.6 Intraslab Scenario

PORT OF ALASKA

Lettis Consultants International, Inc. Figure **37**

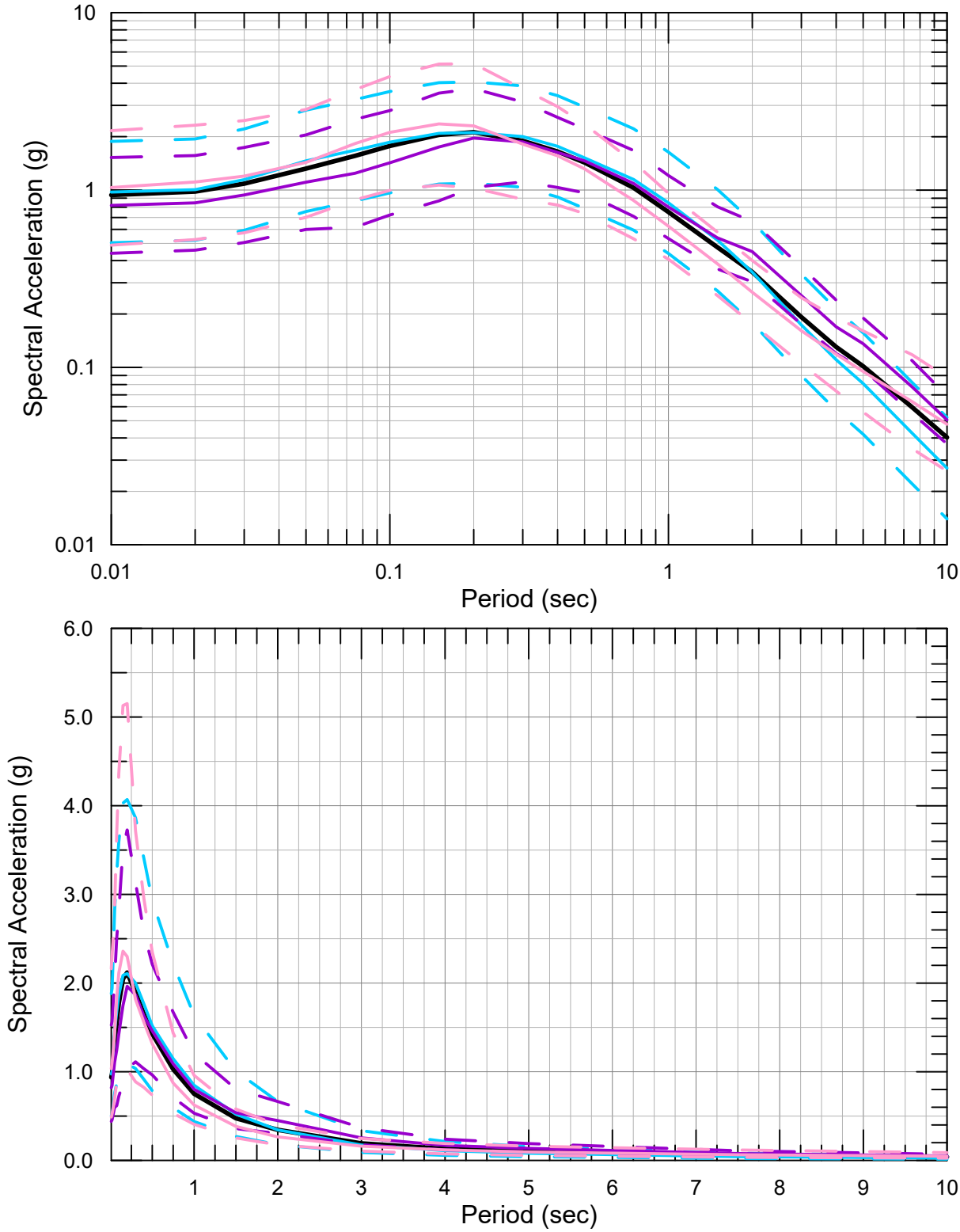

KBCG20
KBCG20, +/-EPS
PSHAB
PSHAB, +/-EPS
AG20
AG20, +/-EPS
Weighted Average

84th Percentile Deterministic Horizontal Acceleration Response Spectra for the M 9.2 Megathrust Scenario

PORT OF ALASKA

Lettis Consultants International, Inc. Figure **38**

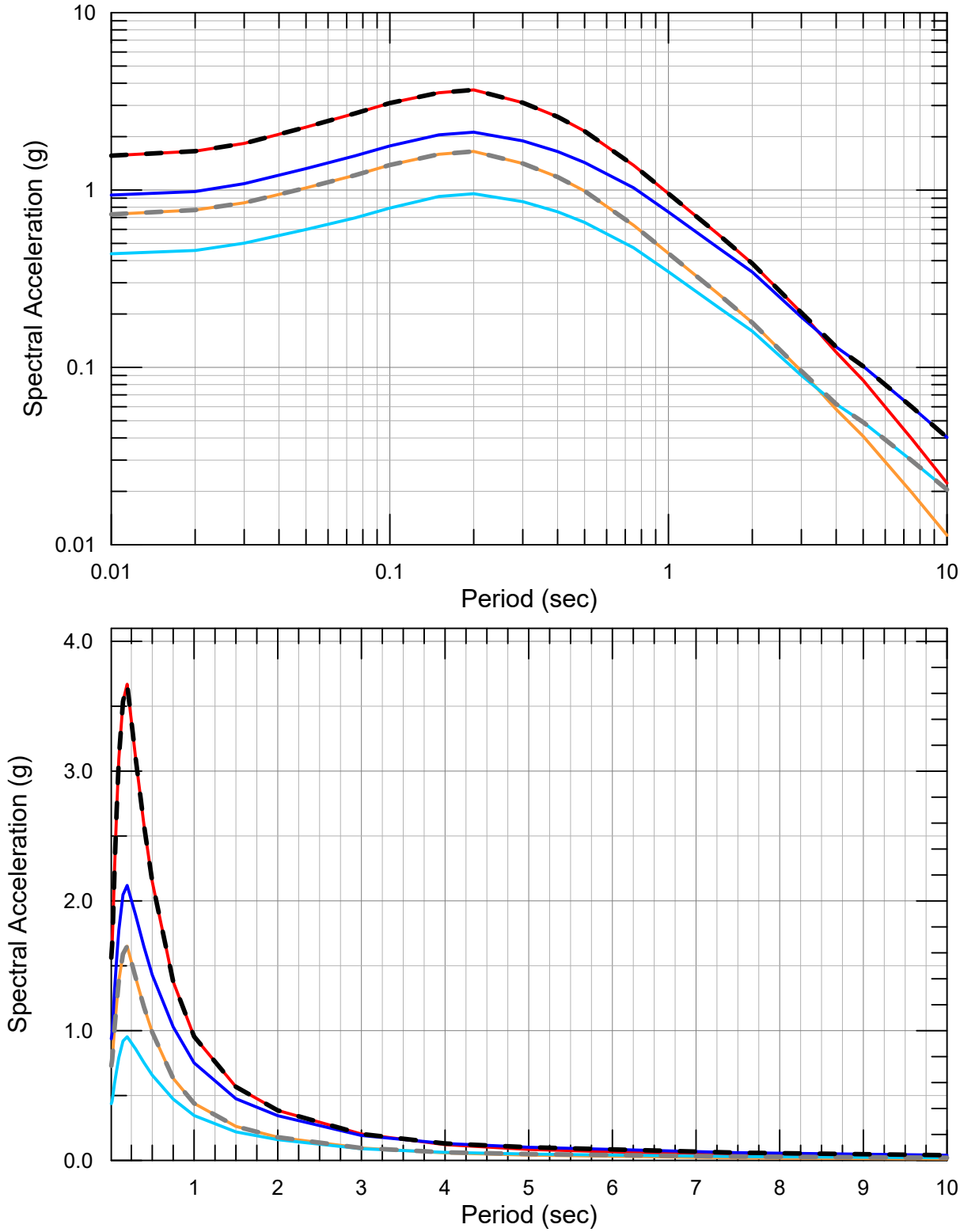

Intraslab - Median
Intraslab - 84th percentile
Megathrust - Median
Megathrust - 84th percentile
Envelope - Median
Envelope - 84th percentile

Comparison of 84th Percentile Deterministic Horizontal Acceleration Response Spectra

PORT OF ALASKA

Lettis Consultants International, Inc. Figure **39**

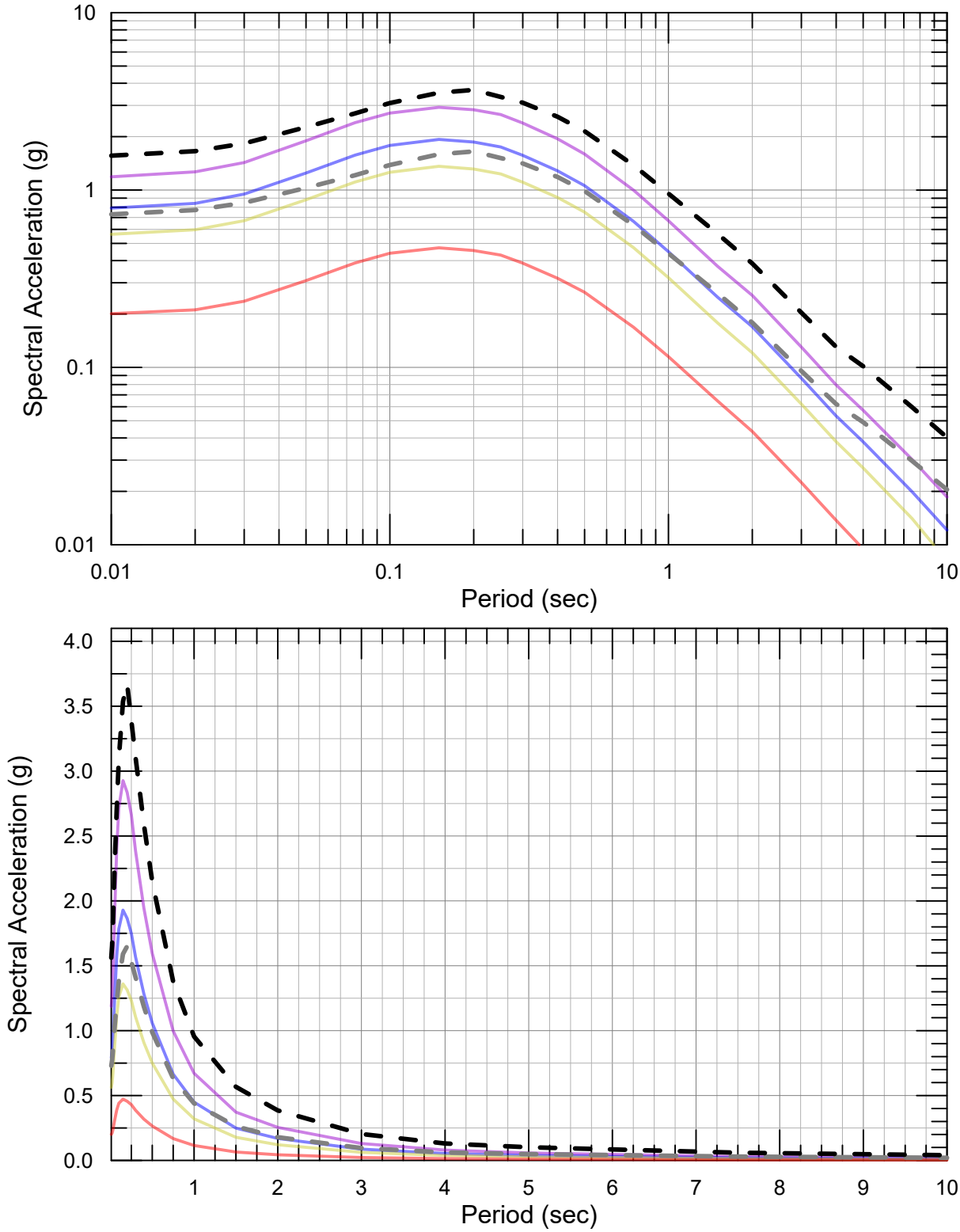

UHS
Return Period (yr)

- 72
- 475
- 975
- 2,475

Enveloped
Deterministic Spectra

- Median
- 84th percentile

Comparison of 5%-Damped Uniform Hazard Spectra at the 72-, 475-, 975-, and 2,475-Year Return Periods with the Controlling Deterministic Spectra

PORT OF ALASKA

Lettis Consultants International, Inc. Figure **40**

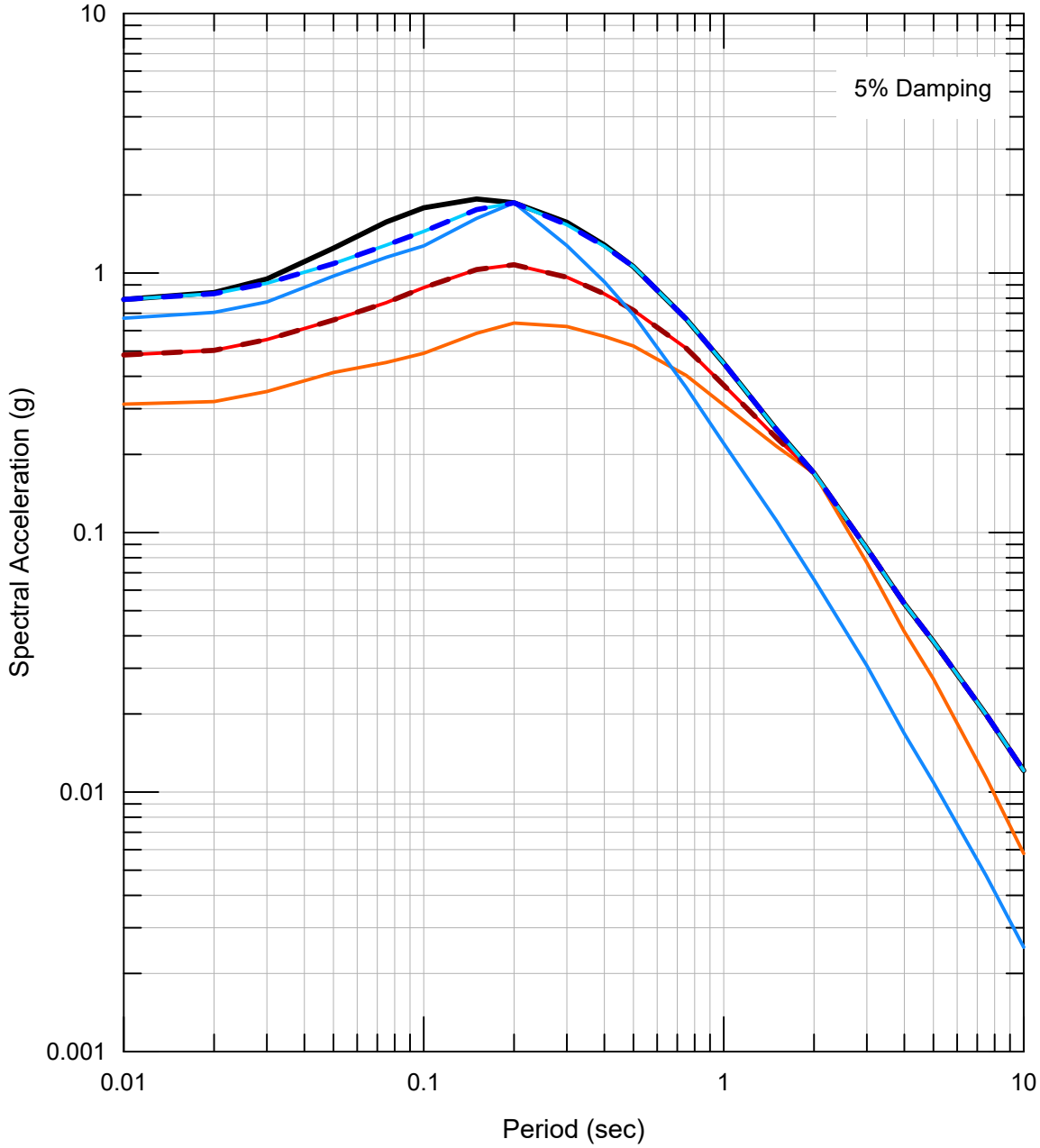

UHS (975-yr rp)
CMS 2.0-Enveloped
CMS 2.0-Interface
CMS 2.0-Slab
CMS 0.2-Enveloped
CMS 0.2-Interface
CMS 0.2-Slab

Uniform Hazard Spectra at 975-Year Return Period and CMS Conditioned at 0.2 and 2.0 sec Using Scenarios for the Interface and Intraslab

PORT OF ALASKA

Lettis Consultants International, Inc.

Figure **41**

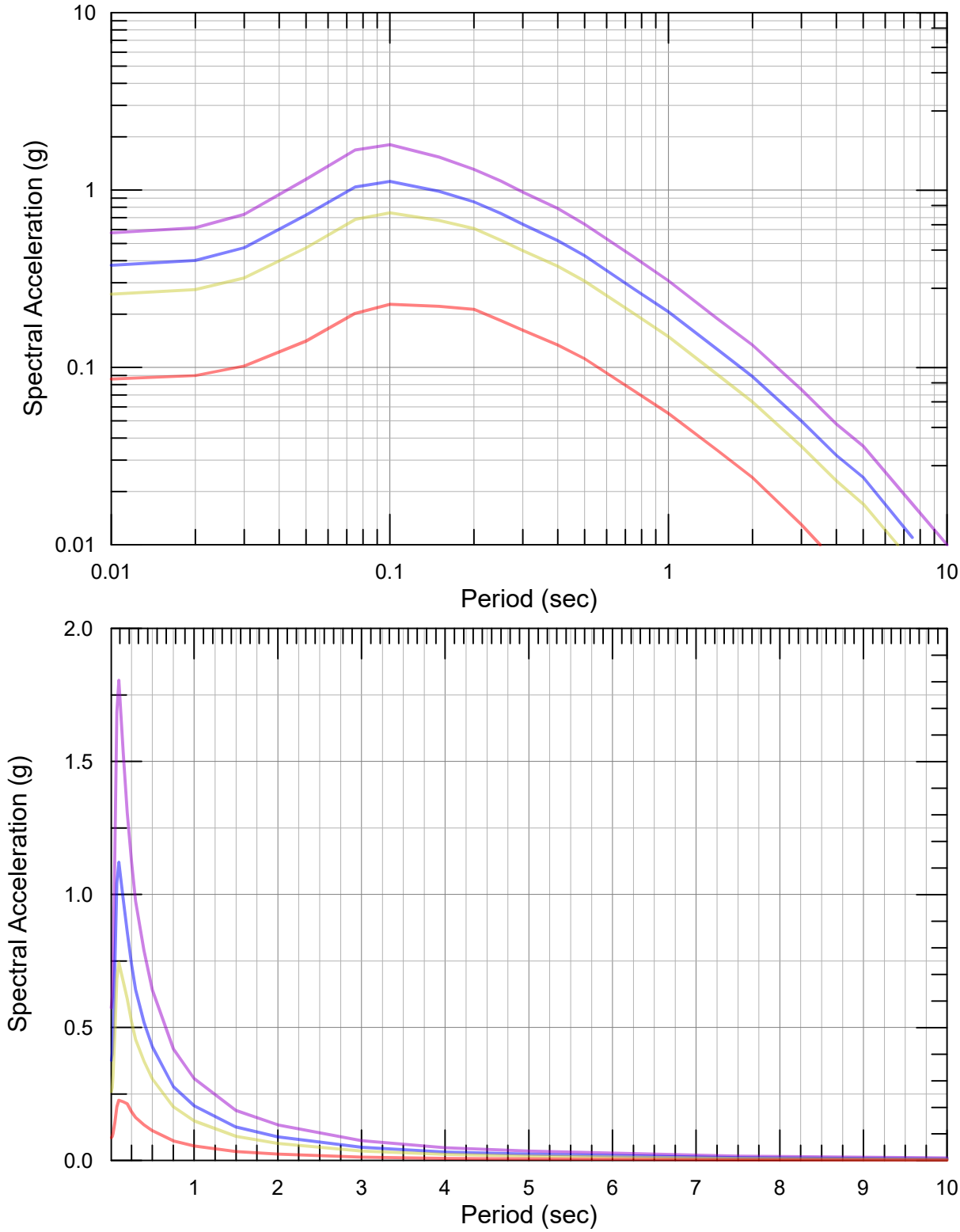

Return Period (yr)

- 72
- 475
- 975
- 2,475

5%-Damped Vertical Spectra at the 72-, 475-, 975-, and 2,475-Year Return Periods

PORT OF ALASKA

Lettis Consultants International, Inc.

Figure **42**

Appendix A
72-Year Return Period Time Histories

Table A-1. Properties of Seed Time Histories for 72yr UHS

No	RSN	Year	Earthquake Name	Station Name	Mag	ClstD (km)	Vs30 (m/sec)	Comp	PGA (g)	PGV (cm/sec)	PGD (cm)	Arias (m/s)	Dur5-95 (sec)	Scale Factor
Seed														
1	1002922	2016	Iniskin	ARTY	7.15	268.7	750	E	0.3430	10.2063	1.4414	0.6660	8.3050	1.22
								N	0.3041	11.7309	1.5665	0.5141	9.4700	1.22
								Z	0.1425	5.1955	1.2141	0.2124	37.6750	1.07
2	2000037	2001	Nisqually	ELW	6.8	63.8	438	E	0.0563	3.9591	1.6251	0.0540	20.6500	3.13
								N	0.0553	3.6990	0.8752	0.0592	19.6300	3.13
								Z	0.0348	2.7854	1.6143	0.0227	26.3600	2.40
3	2000081	2001	Nisqually	2130	6.8	2.7	399	237	0.1482	10.0484	1.7871	0.2163	20.6300	1.54
								327	0.1516	6.8689	1.4717	0.2086	21.7000	1.54
								UP	0.1572	4.4054	0.9067	0.1856	17.0150	0.99
4	3001313	2014	CentralAmerica & Mexico (143)	3687	7.32	165.7	382	01	0.0659	4.1480	1.3442	0.0838	28.3500	3.17
								02	0.0552	3.2301	0.9181	0.0798	27.7050	3.17
								03	0.0320	2.5142	0.5936	0.0264	35.6150	2.69
5	4007388	2011	Miyagi_Pre.Off	NARUKO	7.15	109.8	398.6	S2	0.0806	4.2633	1.0771	0.1341	33.0100	2.36
								W2	0.1040	4.3153	2.0079	0.1425	31.7000	2.36
								D2	0.0620	3.7540	2.1907	0.0827	29.0400	1.64
6	7006045	2006	Pingtung.Doublet1	KAU042	7.02	24.0	815.5	E	0.3269	21.1491	3.9229	1.1796	13.0600	0.80
								N	0.2338	11.1403	3.3129	0.9278	12.8900	0.80
								U	0.1185	6.3817	1.4668	0.1465	17.6950	0.78
7	7006531	2006	Pingtung.Doublet2	CHY068	6.94	78.1	196	E	0.1966	34.0226	14.2395	0.8412	10.2300	0.59
								N	0.3468	17.8487	3.6722	0.9766	11.4350	0.59
								U	0.0810	5.1139	2.4137	0.0943	17.0450	0.94

Table A-2. Properties of Spectrally-Matched Time Histories for 72yr UHS

No	RSN	Year	Earthquake Name	Station Name	Mag	Rrup (km)	Vs30 (m/sec)	Comp	PGA (g)	PGV (cm/sec)	Arias (m/s)	Dur5-95 (sec)	PGD (cm)
Matched													
1	1002922	2016	Iniskin	ARTY	7.15	268.7	750	E	0.2041	10.5028	3.1560	0.2361	8.6450
								N	0.1796	13.0199	3.1499	0.2485	6.9750
								Z	0.1219	6.3994	2.2139	0.2060	38.9500
2	2000037	2001	Nisqually	ELW	6.8	63.8	438	E	0.1951	9.7395	5.9260	0.5311	23.3600
								N	0.1883	10.0641	3.3608	0.5927	21.5700
								Z	0.0755	4.3419	3.3187	0.1239	27.0000
3	2000081	2001	Nisqually	2130	6.8	2.7	399	237	0.2099	15.1375	2.9361	0.3914	20.4500
								327	0.2205	6.6547	2.2417	0.3810	20.4200
								UP	0.0947	4.6834	1.1696	0.1338	21.1650
4	3001313	2014	CentralAmerica & Mexico (143)	3687	7.32	165.7	382	01	0.2347	9.3017	4.4456	0.7856	32.0400
								02	0.1850	8.3726	3.1187	0.7574	31.4450
								03	0.0964	4.9064	1.4330	0.1834	36.1250
5	4007388	2011	Miyagi_Pre.Off	NARUKO	7.15	109.8	398.6	S2	0.1825	10.4287	2.9151	0.6356	33.2800
								W2	0.2195	9.1362	3.9353	0.6733	32.1400
								D2	0.0953	5.7289	3.8408	0.2172	29.1400
6	7006045	2006	Pingtung.Doublet1	KAU042	7.02	24.0	815.5	E	0.2446	15.4153	3.0673	0.5852	13.3200
								N	0.1640	8.8914	2.9713	0.4042	13.3500
								U	0.0857	6.1678	1.2624	0.0888	17.6550
7	7006531	2006	Pingtung.Doublet2	CHY068	6.94	78.1	196	E	0.1440	13.1658	4.8141	0.3278	13.1850
								N	0.2634	9.8491	1.3450	0.4218	12.0300
								U	0.0854	3.9226	1.9328	0.0901	17.8700

Appendix B
475-Year Return Period Time Histories

Table B-1. Properties of Seed Time Histories for 475yr UHS

No	RSN	Year	Earthquake Name	Station Name	Mag	ClstD (km)	Vs30 (m/sec)	Comp	PGA (g)	PGV (cm/sec)	PGD (cm)	Arias (m/s)	Dur5-95 (sec)	Scale Factor
Seed														
1	1002922	2016	Iniskin	ARTY	7.15	289.8	750	E	0.3430	10.2063	1.4414	0.6660	8.3050	3.5010
								N	0.3041	11.7309	1.5665	0.5141	9.4700	3.5010
								Z	0.1425	5.1955	1.2140	0.2124	37.6750	3.1529
2	1002957	2016	Iniskin	AK:Anchorage;FS 07 (new)	7.15	253.9	332	090	0.2107	18.5791	3.8612	0.5830	25.3750	2.6930
								360	0.1815	11.6382	3.0530	0.3803	31.6250	2.6930
								68	0.0488	3.5732	1.3068	0.0406	76.0500	4.7481
3	3000185	1982	CentralAmerica & Mexico (69)	2747	7.31	70.0	519	EW	0.1875	25.2016	7.2953	1.9886	32.4400	2.0320
								NS	0.1695	28.0196	11.6039	1.4604	32.9400	2.0320
								VERT	0.1116	13.2660	2.7654	0.7245	40.9450	1.8290
4	4007389	2011	Miyagi_Pre.Off	TOUWA	7.15	73.0	849.8	S2	0.5504	14.6663	3.2504	7.7157	26.0300	1.7190
								W2	0.6416	19.7945	3.8003	5.7279	21.7100	1.7190
								D2	0.5189	8.8432	4.6808	4.9876	18.0000	1.3128
5	4040459	2011	Miyagi_Pre.Off	Ground Observation Point	7.15	54.6	850	EW	0.5625	19.0495	2.1092	5.0979	21.5200	1.6660
								NS	0.5365	21.3315	2.3529	7.2011	17.6600	1.6660
								UD	0.5301	8.1220	2.7247	7.2359	18.4400	1.1774
6	7005934	2006	Pingtung.Doublet 1	HEN	7.02	42.8	198	E	0.1783	33.5260	9.2419	1.0159	17.5450	2.0710
								N	0.1891	31.4529	8.4314	1.0565	18.1050	2.0710
								U	0.0756	7.5578	1.6863	0.1637	21.4350	2.6134
7	7006045	2006	Pingtung.Doublet 1	KAU042	7.02	50.5	815.5498	E	0.3269	21.1486	3.9228	1.1796	13.0600	2.3020
								N	0.2338	11.1400	3.3128	0.9277	12.8900	2.3020
								U	0.1185	6.3817	1.4668	0.1465	17.6950	2.2979

Table B-2. Properties of Spectrally-Matched Time Histories for 475yr UHS

No	RSN	Year	Earthquake Name	Station Name	Mag	Rrup (km)	Vs30 (m/sec)	Comp	PGA (g)	PGV (cm/sec)	Arias (m/s)	Dur5-95 (sec)	PGD (cm)
Matched													
1	1002922	2016	Iniskin	ARTY	7.15	289.8	750	E	0.6050	24.6848	7.4758	1.9170	8.5450
								N	0.5955	35.8803	8.1311	1.6515	8.8350
								Z	0.3462	17.6181	6.5257	1.8113	38.7050
2	1002957	2016	Iniskin	AK:Anchorage;FS 07 (new)	7.15	253.9	332	090	0.5941	33.5702	7.8653	3.0941	31.4300
								360	0.4413	31.4559	12.1423	2.2795	36.4350
								68	0.3200	15.0865	5.3121	1.0727	60.5800
3	3000185	1982	CentralAmerica & Mexico (69)	2747	7.31	70.0	519	EW	0.7151	38.3964	7.4720	6.2334	48.7850
								NS	0.5669	24.9248	17.9263	4.4121	48.0900
								VERT	0.2615	13.2544	3.9914	1.6093	47.4550
4	4007389	2011	Miyagi_Pre.Off	TOUWA	7.15	73.0	849.8	S2	0.4952	28.4987	9.4060	5.7413	27.8700
								W2	0.5662	31.3636	13.6071	4.8951	21.9900
								D2	0.3915	15.8168	8.4616	5.2002	21.3400
5	4040459	2011	Miyagi_Pre.Off	Ground Observation Point	7.15	54.6	850	EW	0.5328	27.9381	11.7333	4.4847	24.0000
								NS	0.5328	31.2541	8.7004	5.9349	19.7600
								UD	0.3482	10.1958	3.5303	3.1887	20.4400
6	7005934	2006	Pingtung.Doublet1	HEN	7.02	42.8	198	E	0.4117	27.9942	11.2693	3.2142	23.7950
								N	0.5150	28.3808	8.1303	4.0623	20.7750
								U	0.3050	14.5487	4.3871	0.7726	24.7600
7	7006045	2006	Pingtung.Doublet1	KAU042	7.02	50.5	815.5498	E	0.6957	44.0410	8.6803	4.5989	13.3100
								N	0.4461	23.0335	8.9138	3.2609	13.3350
								U	0.2711	17.2863	3.4236	0.7864	17.2100

Appendix C
975-Year Return Period Time Histories

Table C-1. Properties of Seed Time Histories for 975yr UHS

No	RSN	Year	Earthquake Name	Station Name	Mag	ClstD (km)	Vs30 (m/sec)	Comp	PGA (g)	PGV (cm/sec)	PGD (cm)	Arias (m/s)	Dur5-95 (sec)	Scale Factor
Seed														
1	1002922	2016	Iniskin	ARTY	7.15	289.8	750	E	0.3430	10.2064	1.4415	0.6660	8.3050	4.947
								N	0.3041	11.7310	1.5664	0.5141	9.4700	4.947
								Z	0.1425	5.1952	1.2156	0.2124	37.6750	4.514
2	1002957	2016	Iniskin	AK:Anchorage ;FS 07 (new)	7.15	253.9	332	090	0.2107	18.5789	3.8612	0.5830	25.3750	3.805
								360	0.1815	11.6381	3.0529	0.3803	31.6250	3.805
								68	0.0488	3.5734	1.3030	0.0406	76.0500	6.799
3	3000185	1982	CentralAmerica & Mexico (69)	2747	7.31	70.0	519	EW	0.1875	25.2023	7.2955	1.9888	32.4400	2.871
								NS	0.1695	28.0204	11.6042	1.4605	32.9400	2.871
								VERT	0.1116	13.2666	2.8467	0.7245	40.9450	2.619
4	4007389	2011	Miyagi_Pre.Off	TOUWA	7.15	73.0	849.8	S2	0.5504	14.6667	3.2502	7.7162	26.0300	2.429
								W2	0.6417	19.7952	3.8006	5.7282	21.7100	2.429
								D2	0.5189	8.8081	4.6640	4.9876	18.0000	1.879
5	4040459	2011	Miyagi_Pre.Off	Ground Observation Point	7.15	54.6	850	EW	0.5625	19.0495	2.1093	5.0979	21.5200	2.354
								NS	0.5365	21.3316	2.3529	7.2011	17.6600	2.354
								UD	0.5301	8.1398	2.6847	7.2359	18.4400	1.686
6	7005934	2006	Pingtung.Doublet 1	HEN	7.02	42.8	198	E	0.1783	33.5258	9.2418	1.0159	17.5450	2.921
								N	0.1891	31.4527	8.4313	1.0564	18.1050	2.921
								U	0.0756	7.5578	1.6863	0.1637	21.4350	3.742
7	7006045	2006	Pingtung.Doublet 1	KAU042	7.02	50.5	815	E	0.3269	21.1491	3.9229	1.1796	13.0600	3.2475
								N	0.2338	11.1403	3.3129	0.9278	12.8900	3.2475
								U	0.1185	6.3824	1.4672	0.1465	17.6950	3.290

Table C-2. Properties of Spectrally-Matched Time Histories for 975yr UHS

No	RSN	Year	Earthquake Name	Station Name	Mag	Rrup (km)	Vs30 (m/sec)	Comp	PGA (g)	PGV (cm/sec)	Arias (m/s)	Dur5-95 (sec)	PGD (cm)
Matched													
1	1002922	2016	Iniskin	ARTY	7.15	289.8	750	E	0.8661	34.6894	11.5981	3.8274	8.5100
								N	0.8420	41.0684	10.1109	3.6841	7.4400
								Z	0.5803	29.0058	7.1087	1.7242	35.4750
2	1002957	2016	Iniskin	AK:Anchorage;FS 07 (new)	7.15	253.9	332	090	0.7938	48.7254	11.0945	6.1255	31.4150
								360	0.7986	36.2304	12.1766	4.3009	38.5550
								68	0.4187	18.6305	8.1321	2.4663	63.0950
3	3000185	1982	CentralAmerica&Mexico (69)	2747	7.31	70.0	519	EW	0.9855	45.9413	13.4100	12.5226	48.5150
								NS	0.8927	40.5838	24.4017	8.7884	47.9650
								VERT	0.3957	19.5444	7.2099	4.4798	52.0000
4	4007389	2011	Miyagi_Pre.Off	TOUWA	7.15	73.0	849.8	S2	0.6761	40.5023	8.6536	11.3102	27.9100
								W2	0.7634	49.8610	22.6746	9.7004	21.9100
								D2	0.3851	18.4661	8.6967	2.5099	17.8400
5	4040459	2011	Miyagi_Pre.Off	Ground Observation Point	7.15	54.6	850	EW	0.8229	46.0914	14.3405	9.2369	23.5700
								NS	0.7489	42.4306	9.7992	11.8021	19.7000
								UD	0.3271	19.6132	7.2328	3.0812	18.9900
6	7005934	2006	Pingtung.Doublet1	HEN	7.02	42.8	198	E	0.5513	34.8662	14.6850	6.6042	23.5450
								N	0.7390	37.5028	8.9729	8.0446	20.6500
								U	0.4616	19.0750	6.0703	1.6440	24.4950
7	7006045	2006	Pingtung.Doublet1	KAU042	7.02	50.5	815	E	0.9916	62.5286	10.9539	9.5644	13.1250
								N	0.6256	29.6632	14.7655	6.4767	13.2800
								U	0.4147	24.1257	5.3762	1.5773	17.4150

Appendix D
2475-Year Return Period Time Histories

Table D-1. Properties of Seed Time Histories for 2475yr UHS

No	RSN	Year	Earthquake Name	Station Name	Mag	ClstD (km)	Vs30 (m/sec)	Comp	PGA (g)	PGV (cm/sec)	PGD (cm)	Arias (m/s)	Dur5-95 (sec)	Scale Factor
Seed														
1	2000015	2001	Nisqually	HAR	6.8	66.2	131	000	0.2156	24.1222	4.6212	1.0459	19.3800	4.31
								090	0.1868	30.8870	9.0596	0.9947	25.8900	4.31
								DWN	0.0881	9.2762	2.3413	0.2191	29.0400	5.50
2	2000023	2001	Nisqually	SDS	6.8	66.8	200	180	0.2745	34.7797	5.7389	1.0179	34.8150	3.87
								270	0.2142	36.8208	11.0630	0.7468	36.4400	3.87
								DWN	0.1069	12.8548	2.8741	0.2892	28.3250	4.88
3	3000185	1982	CentralAmerica & Mexico (69)	2747	7.31	70.0	519	EW	0.1875	25.2018	7.2954	1.9887	32.4400	4.33
								NS	0.1695	28.0198	11.6040	1.4605	32.9400	4.33
								VERT	0.1116	13.2660	2.7654	0.7245	40.9450	4.01
4	4040459	2011	Miyagi_Pre.Off	Ground Observation Point	7.15	54.6	850	EW	0.5625	19.0500	2.1093	5.0981	21.5200	3.55
								NS	0.5365	21.3319	2.3531	7.2014	17.6600	3.55
								UD	0.5301	8.1220	2.7247	7.2359	18.4400	2.58
5	6000989	1997	SouthAmerica (610157)	ILLAPEL COMISARIA	7.09	80.1	486	L	0.2850	11.1993	1.8207	2.1966	16.7700	5.16
								T	0.3692	16.1665	1.9331	2.7542	16.7150	5.16
								V	0.1937	5.2595	1.0566	0.6992	20.6600	4.54
6	7006045	2006	Pingtung.Doublet 1	KAU042	7.02	50.5	816	E	0.3269	21.1491	3.9229	1.1796	13.0600	4.90
								N	0.2338	11.1403	3.3129	0.9278	12.8900	4.90
								U	0.1185	6.3817	1.4668	0.1465	17.6950	5.04
7	7006531	2006	Pingtung.Doublet 2	KAU080	6.94	34.7	399	E	0.1966	34.0219	14.2392	0.8412	10.2300	3.62
								N	0.3468	17.8484	3.6722	0.9766	11.4350	3.62
								U	0.0810	5.1139	2.4138	0.0943	17.0450	6.07

Table D-2. Properties of Spectrally-Matched Time Histories for 2475yr UHS

No	RSN	Year	Earthquake Name	Station Name	Mag	Rrup (km)	Vs30 (m/sec)	Comp	PGA (g)	PGV (cm/sec)	Arias (m/s)	Dur5-95 (sec)	PGD (cm)
Matched													
1	2000015	2001	Nisqually	HAR	6.8	66.2	131	000	1.2485	58.6728	14.8912	15.0459	28.3800
								090	1.0448	64.9437	19.2839	13.8118	31.8300
								DWN	0.7317	28.8383	10.0990	5.4243	30.7300
2	2000023	2001	Nisqually	SDS	6.8	66.8	200	180	1.4672	63.3061	11.1957	13.0237	37.2000
								270	1.1184	77.6089	21.7198	10.1818	47.0700
								DWN	0.6126	32.1431	11.4706	5.0389	33.0200
3	3000185	1982	CentralAmerica & Mexico (69)	2747	7.31	70.0	519	EW	1.4503	63.5374	19.0870	27.7684	48.6200
								NS	1.3068	65.3985	38.3634	20.3255	47.4700
								VERT	0.6512	30.5627	10.1386	7.9065	46.0350
4	4040459	2011	Miyagi_Pre.Off	Ground Observation Point	7.15	54.6	850	EW	1.1076	63.5885	20.1447	20.4969	23.6600
								NS	1.1334	49.7696	12.6989	26.8135	19.6600
								UD	0.7939	21.6774	7.7810	17.4351	20.4400
5	6000989	1997	SouthAmerica (610157)	ILLAPEL COMISARIA	7.09	80.1	486	L	1.0148	66.1271	15.7309	26.4498	17.1550
								T	1.1755	76.6251	14.3701	33.1411	17.0900
								V	0.6452	24.0800	7.1505	12.0455	21.8600
6	7006045	2006	Pingtung.Doublet1	KAU042	7.02	50.5	816	E	1.4378	107.6383	17.1249	20.7341	13.2600
								N	0.9512	51.9981	19.4114	14.6628	13.1800
								U	0.6535	35.5915	7.3936	3.8419	17.4700
7	7006531	2006	Pingtung.Doublet2	KAU080	6.94	34.7	399	E	0.8883	89.2866	28.4581	11.6672	13.3800
								N	1.5497	58.4473	8.5859	14.7361	12.0400
								U	0.5866	23.7493	12.7450	4.0986	16.9700